Master's thesis
Astronomy

Star formation in selected Planck fields

Emma Mannfors

February 28, 2019

Tutor: adjunct prof. Mika Juvela

Censors: prof. Karri Muinonen
adjunct prof. Mika Juvela

UNIVERSITY OF HELSINKI
Department of Physics

P.O. Box 64 (Gustaf Hällströmin katu 2a)
00014 Helsingin yliopisto

"The world beyond Earth had always been a mysterious place, silent, dark and cold, the realm of magic and gods."

—Margot Lee Shetterly, *Hidden Figures*

HELSINGIN YLIOPISTO — HELSINGFORS UNIVERSITET — UNIVERSITY OF HELSINKI

Tiedekunta — Fakultet — Faculty	Laitos — Institution — Department
Faculty of Science	Department of Physics

ii

Tekijä — Författare — Author
Emma Mannfors

Työn nimi — Arbetets titel — Title
Star formation in selected Planck fields

Oppiaine — Läroämne — Subject
Astronomy

Työn laji — Arbetets art — Level	Aika — Datum — Month and year	Sivumäärä — Sidoantal — Number of pages
Master's thesis	February 28, 2019	159 pages

Tiivistelmä — Referat — Abstract

Star formation in 53 Galactic fields, selected from the Planck Catalog of Galactic Cold Clumps, has been studied using continuum submillimeter observations from the Herschel space telescope (PACS instrument 70, 100, and 160 μm, SPIRE instrument 250, 350, and 500 μm) and the James Clerk Maxwell Telescope SCUBA-2 instrument (850 μm). Fields are located at galactic latitudes between -20 and +37, and distances of 0.1-4.5 kpc.

Dense clumps have been extracted from the 850-μm data using the `FellWalker` clumpfinding algorithm. Properties of the dust have been found by fitting a modified blackbody function to SPIRE data and clump masses have been estimated using dust properties. Whether clumps are gravitationally bound has been estimated using Bonnor-Ebert analysis. Finally, young stellar objects (YSO) from four catalogs have been associated with the clumps.

Clumps are characterized as protostellar, prestellar or starless with protostellar sources having at least one YSO spatially related to them. Prestellar clumps are gravitationally bound while starless clumps are not. Virial analysis has been performed and compared to the results of Bonnor-Ebert analysis to study the role of turbulence in these regions.

`FellWalker` analysis found 529 dense clumps, 147 of which had sufficient data for mass estimation. Mass and radius of clumps is strongly correlated with distance. Temperature also shows a slight increase in more distant fields. These effects are due to the resolution of the SCUBA-2 instrument. Of these 147 clumps, from Bonnor-Ebert analysis 91 are protostellar, 55 prestellar, and 1 starless. The starless clump is the coldest and smallest of the whole sample. Prestellar clumps have an average temperature of 13.2 $\pm$ 1.0 K, and a column density of $(1.5\pm0.8)\times10^{22}$ cm^{-2}. Protostellar clumps are on average larger and hotter, but have lower column density than other types of clumps. Virial analysis, which includes estimates of non-thermal support, found 91 protostellar, 17 prestellar, and 39 starless clumps, showing a strong effect of turbulence. Virial prestellar clumps are the largest, coldest and densest of the sample.

These clumps represent a diverse sample of Galactic star forming regions, from high-latitude nearby clumps to distant massive clouds.

Avainsanat — Nyckelord — Keywords
ISM, Star formation, prestellar cores, molecular clouds, infrared astronomy

Säilytyspaikka — Förvaringsställe — Where deposited

Muita tietoja — övriga uppgifter — Additional information

Contents

Acknowledgements

This thesis would not have been possible without the support and guidance of my supervisor, adjunct prof. Mika Juvela. I am also grateful for the whole ISM group: Mika Saajasto for helping me with a thousand small problems and giving me several scripts, Dr. Elisabetta Micelotta for being so welcoming and always inviting me to tea, Dr. Laura Zschaechner for immediately including me in observation proposals and conference organization, Dr. Jorma Harju for always being ready to help, and Heidi Kirppu for working with me at the start of this project. I am grateful to prof Karri Muinonen for agreeing to read my thesis. All the staff and students at the astronomy department have been incredibly supportive and welcoming.

I want to thank the board of Meridiaani: Eerika, Ilja, Juho, Leo, Lepe, Taavi, Teo, Veera, and Vili, for their support and friendship over the past year. I could not have done this without all the wonderful people I have met during my years at the physics department, thanks for making procrastination at the student room so easy. Special thanks to Riina for all our conversations about Jane Austen. Finally, thank you to Ari-Pekka Honkanen, for answering questions about programming and academia, for all your love, and support, and most importantly, the cat photos.

Abbreviations

BSC = Akari Bright Source catalog made with the Akari Far-Infrared All-Sky Survey instrument.

BE = Bonnor-Ebert

CMF = Core mass function

ESA = European Space Agency

FWHM = Full width at half maximum

GCC = (Planck) Galactic Cold Cores survey

GMC = Giant molecular cloud

IMF = Initial mass function

IR = Infrared

ISM = Interstellar matter

JCMT = James Clerk Maxwell Telescope

MBB = Modified blackbody

MC = Molecular cloud

MS = Stellar main sequence; a star which is burning Hydrogen in its core

PACS = The Photoconductor Array Camera and Spectrometer on the Herschel Space Observatory

PGCC = Planck Galactic Cold Clumps Catalog

PI = Principal investigator

PSC = Akari Point-Source Catalog

SCUBA-2 = Submillimetre Common-User Bolometer Array 2 instrument on the JCMT

SCOPE = SCUBA-2 Continuum Observations of Pre-protostellar Evolution survey

SED = Spectral energy distribution

SF = Star formation

SFE = Star formation efficiency

SFR = Star formation rate

SN = Supernova

SPIRE = Spectral and Photometric Imaging Receiver on the Herschel Space Observatory

TOP = TRAO Observations of Planck cold clumps survey

TOP-SCOPE = *see* TOP, SCOPE

TRAO = Taeduk Radio Astronomy Observatory

TT = T-Tauri star

YSO = Young stellar object

1. Introduction

The birth and formation of stars is crucial to understanding many astrophysical phenomena such as the evolution of galaxies and planetary formation. While the basic processes of star formation (SF) are well-known, especially the initial conditions of the birth clouds are open questions. In this thesis, I study the conditions of star formation in the Galaxy by determining properties of dense clumps and cores within the larger interstellar medium (ISM).

This chapter presents theory about star formation, interstellar matter, and concepts relevant to this research. Chapter 2 discusses how these data were observed and reduced before the start of this thesis, as well as instrument specifications. Chapter 3 discusses data reduction and analysis steps performed by me for this thesis. Chapter 4 presents the results and 5 discusses the findings.

The appendices contain further information, including selected scripts used in the data analysis, tables of derived properties, and images.

1.1 The interstellar medium

The ISM includes all the baryonic[1] matter in a galaxy not found in stars or planets, and is composed of dust, gas, cosmic rays, electromagnetic radiation, and magnetic fields. Around 99% of the matter is gas, which itself is mostly Hydrogen and He-

[1]Visible matter, as opposed to dark matter or dark energy

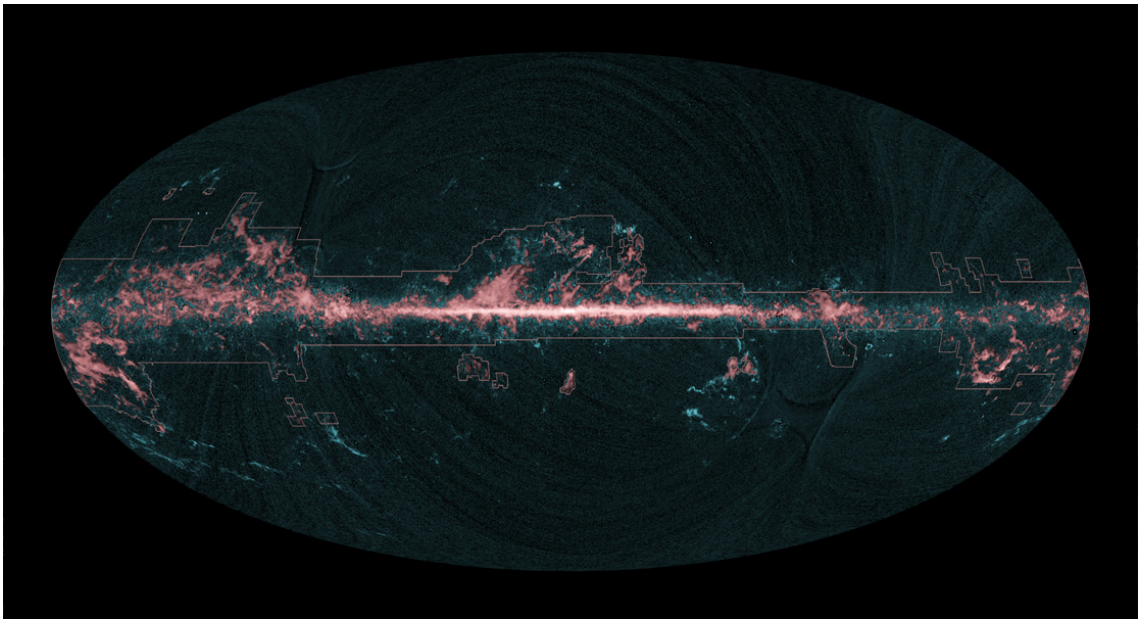

Figure 1.1: Distribution of CO seen by ESA Planck telescope (*blue*) overlaid on a compilation of previous CO surveys (Dame et al. (2001)) (*red*). White outlines mark the limits of the Dame et al. surveys. Credit: ESA/Planck Collaboration; T. Dame et al., 2001

lium, and around 2% metals[2] by mass [1]. Gas can be in any state, as ionized gas from the diffuse medium at high galactic latitudes, to HII regions around massive young stars, and as dense, cold clouds of molecular gas. Only a few percent of the ISM by mass is found in molecular clouds (MC), which are concentrated near the plane of the Galaxy and which are the hosts for star formation. Fig. 1.1 shows the spread of CO molecules through the galaxy, which corresponds to the overall spread of molecular gas. Gas can be found from smaller clumps all the way to giant molecular clouds (GMC), which can contain up to a few million solar masses.

Dust grains make up around 1% of the ISM, but cause much of the optical extinction. Interstellar dust is composed mostly of carbon compounds and silicates with grain sizes below 1 μm [1].

[2]All elements except Hydrogen and Helium are known as metals.

Figure 1.2: NASA/ESA Hubble Space Telescope image of Sh 2-106, a compact star-forming region in Cygnus. A new star, S106 IR, is visible at the center and is responsible for the hourglass shaped HII region. Ionized Hydrogen is colored blue. Credit: Hubble (NASA/ESA)

1.2 Characteristics of the interstellar medium

Gas in more diffuse clouds can be ionized or atomic, whereas the gas inside dense clouds is generally molecular as it is protected from the interstellar UV radiation field. Most of the gas in a molecular cloud is molecular Hydrogen, H_2 [1].

It is currently believed that most SF occurs on filamentary structures within MCs. Often, molecular gas forms one main filament, which may contain clumps and cores [2], and which is surrounded by smaller, perpendicular filaments. Clumps are a large, gravitationally unbound collection of gas [3], with mass of 10-10^3 $M_\odot$ and sizes under 2 pc. Cores are denser and further evolved than clumps and have mass under 10^2 $M_\odot$ and size under 0.5 pc [4]. Cores can be protostellar, prestellar, or starless. Protostellar cores have already begun the process of SF and contain protostars. Prestellar cores have not yet begun SF, but are massive enough that they are likely to do so in the future. Starless cores are not massive enough to be collapsing under

gravity unless they receive more material from the surrounding ISM.

Size

Molecular gas in galaxies is usually concentrated in large complexes with sizes of some kpc and masses up to 10^7 $M_\odot$ which can host several GMCs of size up to 100 pc and masses around 10^6 $M_\odot$. GMCs then contain much smaller, clumpy or filamentary structures [5]. Smaller MCs of mass $\sim 10^4$ $M_\odot$ are known as dark clouds [4], many of which are found in the solar neighborhood and which are some of the most studied SF clouds. These include, for example, the Taurus-Perseus MC ($d \sim$ 140 pc) [6], the Aquila MC ($d \sim 260$ pc) [7] and the Orion MC ($d \sim 440$ pc) [8]. Mass distribution of GMCs inside the solar circle is a power-law with a sharp cutoff at the high-mass end around $6{\times}10^6$ $M_\odot$ and 80% of mass inside GMCs is located in clouds with mass over 10^5 $M_\odot$ [9].

Column density

Molecular Hydrogen exists at column densities beyond $N(\mathrm{H}){\sim}\ 2{\times}10^{20}$ cm^{-2}, which corresponds to a visual extinction $A_\mathrm{v} \sim 0.1$ mag [9]. CO can form at column densities beyond $N(\mathrm{H}){\sim}\ 1.4{\times}10^{21}$ cm^{-2}, or $A_\mathrm{v} > 1$ mag, and CO line emission is often used as an observational tracer of H_2 gas [4]. As direct observations of H_2 are challenging, molecular clouds with column densities below the CO threshold are difficult to observe. However, most dense clouds involved in SF have column densities which are much higher, with typical values above 10^{22} cm^{-2}. Könyves et al. [7] found that around 90% of prestellar cores have background column density corresponding to $A_\mathrm{v} \sim 7$ mag. Column density and visual extinction are related by the empirical relation [10]:

$$N(\mathrm{H_2})/\mathrm{A_v} = 10^{21}\ \mathrm{cm^{-2}/mag}. \tag{1.1}$$

Temperature

Gas in the ISM is heated by the interstellar radiation field or through collisions. As cooling due to H_2 is extremely inefficient, CO molecules are responsible for most of the cooling in the dense ISM. While other metals also aid in cooling, they are not as abundant as CO. Increasing density of molecular clouds results in increased line cooling efficiency, while also reducing heating from external sources. Thus, temperatures in molecular clouds are around 10–20 K though temperatures of up to 100 K may exist around newly formed stars [5].

Collapsing gas generates heat, which is radiated away while the cloud is optically thin, keeping a constant temperature. Only during protostellar collapse, when the clump is dense enough, does the gas become opaque to radiation and the temperature begins to rise.

Optical depth

Optical depth τ describes the distance radiation can propagate inside a medium without interaction; a more optically thick medium causes higher extincton of background sources. At optical, UV, and near-infrared wavelengths, extinction is stronger for bluer light, and thus causes reddening of background starlight. The reddened color excess of light E(B-V) can be related to Hydrogen column density $N(\mathrm{H})$ by [4, 11]:

$$\frac{N(\mathrm{H})}{E(B-V)} = 5.8 \times 10^{21} \frac{\mathrm{H}}{\mathrm{cm}^2 \ \mathrm{mag.}}$$

Column densities can be directly estimated based on the reddening of background stars by this relation.

Turbulence

A nonturbulent MC would collapse and form stars at a rate much higher than that observed, thus real MCs must have a mechanism supporting them against

gravitational collapse. Observations of MCs show that most have internal velocity dispersion larger than that caused by thermal motions [1]. It is clear that most MCs have significant internal turbulence, caused by feedback from young stars, conversion of energy during collapse, and inheritance from the diffuse ISM. Turbulence in most MCs is supersonic [5].

Magnetic fields

Magnetic fields permeate the ISM. The field strength of the Galaxy is around 3 μG [1] and follows the spiral arm structure. It is approximately a factor of 1.5 stronger within the arms than between them [4]. Inside SF regions magnetic field strength has been found to increase with density, with dense massive SF cores having field strengths of 10 mG on 0.1 parsec scales [12]. Magnetic field energy inside these cores can be comparable to turbulent kinetic energy in clouds with $A_v \geq 2$ mag [4], thus making magnetic fields another important factor supporting a dense core against collapse.

1.2.1 Dust emission and the modified blackbody function

SF is obscured in the optical wavelengths by interstellar dust but can be studied in the IR and radio regimes by observing molecular lines and emission from dust heated by young stars [5]. Different molecular lines also show different parts of the core; CO and CS the cloud surface, N_2H^+ and NH_3 deeper layers, and H_2D^+ and D_2H^+ the very centers [13]. This is due to depletion, or the underabundance of a certain element or molecule in cores [4]. Molecules containing carbon, such as CO and CS are depleted already at the outer layers of dense cores [14], whereas molecules with Nitrogen and Hydrogen, such as N_2H^+ are depleted much later, only at the centers of the cores. CO abundance, for example, is 1-2 orders of magnitude larger at the core edge than in core centers [13]. The heavier H_2D^+ is depleted even later.

The hottest objects are seen in the shortest wavelengths. A visible object in 70 or 100 μm is a good indicator of a protostellar core as the SED of an accreting core peaks at under 100 μm [15]. Many studies (e.g. [7, 16], etc.) use a detection at 70 μm to classify cores as protostellar.

Dust emission at longer wavelengths is used to estimate the masses and column densities, by observing optical depth and estimating a dust opacity κ_ν. Submillimeter dust opacities generally assume a power-law of the form $\kappa_\nu \propto \nu^\beta$, where β is the opacity spectral index. Observations of dust emission from cold, dusty SF regions can be approximated by graybody emission from the product of this power-law and Planck function [17]. This also gives the opportunity to estimate the temperature of the emitting grains. Thermal emission of cold dust (T~10–40 K) peaks at around 70–500 μm, however both β and temperature affect the shape of this SED peak.

Continuum dust emission follows a modified blackbody (MBB) spectrum [2]:

$$F_\nu = F_{\nu_0} \frac{B(\nu, T)}{B(\nu_0, T)} \left(\frac{\nu}{\nu_0}\right)^\beta = \frac{\kappa_\nu B(T) M}{d^2}. \tag{1.2}$$

F_ν is the average flux for a frequency ν in Jy and F_{ν_0} the flux of a reference frequency ν_0, d the distance to the source, M the total mass of the object, and B(T) the Planck function:

$$B(T) = \frac{2h\nu^3}{c^2} \frac{1}{e^{h\nu/k_B T} - 1}.$$

Here h is the Planck constant, k_B the Boltzmann constant, and c the speed of light. Dust opacity κ_ν in dense clouds is often approximated with:

$$\kappa_\nu = 0.1(\nu/1000 \text{ GHz})^\beta, \ \beta = 1.8, \tag{1.3}$$

in units of [cm^2 g^{-1}] [18, 19]. κ_ν thus describes the absolute value of the optical depth relative to the total ISM mass.

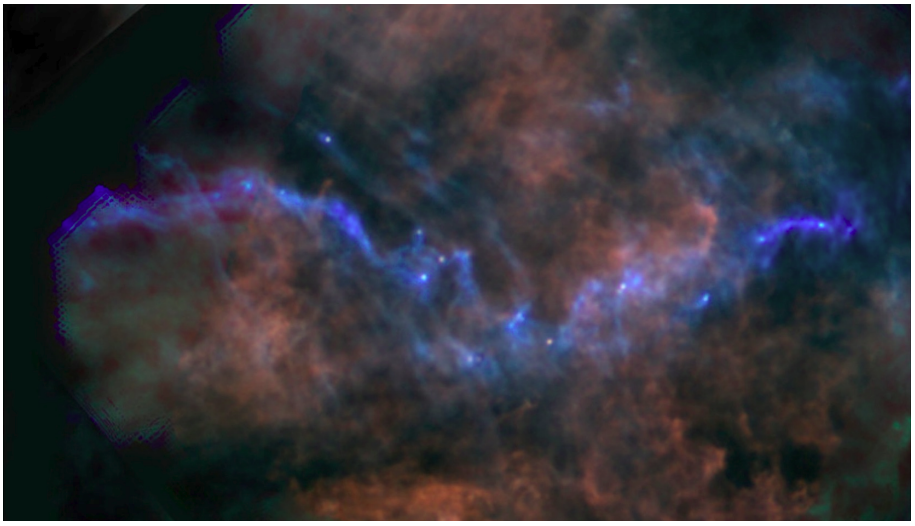

Figure 1.3: ESA Herschel SPIRE image of PGCC cloud G82.65-2.00 showing typical filamentary structure. Blue color is the coldest and densest part of the cloud, with mass 800 $M_{\odot}$, and red is slightly warmer dust. The field of view is 1° in size. Credit: ESA/Herschel/SPIRE/M. Juvela (U. Helsinki, Finland)

1.3 Molecular clouds

A MC can begin to contract under gravitational forces, but this collapse will be halted by turbulence, magnetic energy, and stellar feedback. With sufficient mass, a cloud may go through several bursts of SF. Eventually, all star-forming MCs will be destroyed by feedback from the stellar wind and supernovae (SN) of high-mass stars, or by Galactic shear or other large-scale motions. Potential MC lifetimes have been estimated in various ways, including measuring the chemical composition of the MC and the ratio of HI and H_2, or by comparing the number of starless and protostellar cores [9]. Lifetimes of around 20-30 Myr for a GMC have been estimated, dependent on the size of the cloud and the mass of the stars forming inside it. GMCs are destroyed by photoevaporation, smaller MCs often do not reach full ionization before being destroyed.

Most SF in the Milky Way happens in the galaxy's spiral arms, in a region which is around 200 pc thick. Studies support the theory of turbulent fragmentation, in

which filaments will form due to anisotropies in the larger cloud caused by magnetic fields, supersonic turbulence and radiation. Turbulence creates sheets of shocked gas, and where these sheets intersect, filaments form [9], as seen in Fig. 1.3. These filaments then fragment and condense into cores, especially where filaments converge, and some of these cores will go on to form stars [3]. Most stars are formed on filaments, with higher-mass stars being associated with denser filaments or at the intersection of multiple filaments [20].

SF can be triggered by cataclysmic events such as nearby SN, or interactions with expanding HII regions around OB stars and the host molecular cloud [21], or through gravity alone. There is a minimum mass required for a cloud to begin collapse into a protostar (Sect. 1.3.1). On large scales, gravitational tidal forces prevent collapse; on smaller scales, turbulence and, around more evolved objects, radiative pressure take effect.

Only a part of a molecular cloud will form stars, as few regions will become dense enough for SF. A contracting object will continue to accrete material from its envelope. As it matures, the envelope will collapse to a protostellar disk, from which a planetary system may be born. Once the central object becomes hot enough to fuse Hydrogen, the star will move towards the main sequence (MS) and eventually escape its host cloud. Stars are generally born in clusters, most of which dissipate with age [5].

1.3.1 Gravitational stability

A cold core can only form a star if the core is gravitationally bound, or gravitationally unstable. Both terms are used in this thesis. Virial balance is the best method of determining instability, however there are also several rougher approximations that disregard for example non-thermal motion.

The Jeans theory of cloud fragmentation considers an initially nearly uniform medium

which contains small density fluctuations. In a nonmagnetized and nonrotating medium without turbulence, density fluctuations over a certain length λ_J will not propagate but will instead grow exponentially. If the density of the medium is ρ and its temperature T, this Jeans length can be expressed with the aid of the isothermal sound speed c_s [15]:

$$\lambda_J = \pi^{1/2} c_s (G\rho)^{-1/2},$$

$$c_s = \sqrt{k_B T / \mu m_H}, \tag{1.4}$$

where m_H is the Hydrogen mass, $\mu = 2.33$ u is the mean molecular weight per particle, and k_B the Boltzmann constant. In a spherically symmetric situation, the minimum mass required for gravitational instability is the Jeans mass, $M_J = \rho\lambda_J^3$. This is very similar to the equation for the critical line mass of filaments, $M_{crit} = \dfrac{2c_s^2}{G}$, which describes the minimum mass required for gravitationally unstable infinite, isothermal cylinders [22]. However, internal gravity and external pressure are not enough to cause high pressures observed inside filaments, thus it is likely that filaments are contained by helical magnetic fields. Gravitationally unstable filaments contract radially. Once central density reaches a critical density $n_c \sim 10^6$ cm^{-3} the filament begins to fragment into cores, though the value of n_c depends on local turbulence and the system's total mass [9].

Virial Theorem

The energy of an isolated cloud in equilibrium can be described by

$$\frac{1}{2}\ddot{\mathcal{I}} = 2\Omega_K + \Omega_G + \Omega_M + \Omega_P, \tag{1.5}$$

where $\ddot{\mathcal{I}}$ is the second derivative of the moment of inertia, Ω_K the contribution from internal (kinetic) energy, Ω_G the gravitational potential energy, Ω_M the magnetic energy, and Ω_P the energy from external pressure [9, 14]. When $\ddot{\mathcal{I}} = 0$, the core is

virially stable, if $\ddot{\mathcal{I}} < 0$, total energy is negative and the core is collapsing.

By setting Ω_M and Ω_P to zero, thus assuming that the cloud is supported by turbulence alone [4], a virially stable system ($\ddot{\mathcal{I}} = 0$) has a relation between kinetic energy Ω_K and potential energy Ω_G:

$$\Omega_K = -\frac{1}{2}\Omega_G \Rightarrow \frac{1}{2}M\sigma^2 = \frac{1}{4}G\frac{M^2}{R}, \tag{1.6}$$

where R is the radius and M the mass of the object, σ^2 the square of the velocity dispersion, and G the gravitational constant. In reality, the virial approximation applies only to isolated systems, as a core may be virially subcritical but still collapse if it gets more mass from external gas flows.

The virial parameter α_{vir} can be calculated by the formula [20]:

$$\alpha_{\rm vir} = M_{\rm vir}/M_{\rm obs}, \tag{1.7}$$

where $M_{\rm obs}$ is the observed mass and $M_{\rm vir}$ the virial mass. If $\alpha_{\rm vir} \leq 1.0$, the core is gravitationally bound. $M_{\rm vir}$ is calculated from Eq. 1.6:

$$M_{vir} = \frac{kR_{\rm core}\sigma^2_{\rm tot}}{G}, \tag{1.8}$$

where k is a constant which depends on the density distribution. Assuming the density profile of the core scales as r^{-n} [23], k can be calculated:

$$k = \frac{5-2n}{3-n}.$$

For example, Parikka et al. [24] use $k = 1.333$, corresponding to $n = 1.5$. Non-thermal velocity dispersion σ can be estimated from molecular line observations:

$$\sigma = \sqrt{\frac{k_{\rm B}T_{\rm kin}}{\overline{m}} + \Big(\frac{\Delta V^2}{8\ln(2)} - \frac{k_B T_{\rm kin}}{m}\Big)}, \tag{1.9}$$

where $k_{\rm B}$ is the Boltzmann constant, $\overline{m} = 2.33$ u the mean molecular mass, and m the mass of the molecule used for observations. ΔV is the observed FWHM width of the spectral line. $T_{\rm kin}$ is the kinetic temperature of the gas, which can be estimated

e.g. from ammonia lines which depend only on $T_{\rm kin}$. When suitable molecular line observations are not available, continuum observations can also be used by assuming the gas temperature is similar to dust temperature. This is true only for densities over 10^5 cm^{-3} [25].

Bonnor-Ebert mass

By disregarding magnetism, clumps can be modeled as isothermal spheres bound by external pressure, known as Bonnor-Ebert (BE) spheres [26, 27]. Assuming fixed sound speed $c_{\rm s}$ (Eq. 1.4) and gravitational constant G, the minimum mass required for collapse is the Bonnor-Ebert mass $M_{\rm BE}$ [28]:

$$M_{\rm BE} = 2.4\frac{R_{\rm BE}c_{\rm s}^2}{G}, \tag{1.10}$$

with $R_{\rm BE}$ being the required radius. A gravitationally bound core is seen to have

$$\alpha_{\rm BE} = M_{\rm BE}/M_{\rm obs} \leq 2, \tag{1.11}$$

where $M_{\rm obs}$ is the observed mass [7, 15]. By replacing $c_{\rm s}$ with effective sound speed, the turbulent motions can also be included in BE analysis, however this also requires molecular line observations.

1.4 Young stellar objects

Lada [29] presented a classification of young stellar objects (YSOs) which divided them into three classes: I, II, and III. Andre et al. [30] added to this categorization Class 0 protostars, and Greene et al. [31] a fifth category, flat-spectrum sources. As more evolved YSOs have less IR excess than newly-formed ones, classification depends on spectral index α of protostars based on their continuum spectrum between 2 and 20 μm [1]. Fig. 1.4 shows structure and example spectra of class 0–III YSOs. Class 0 protostars are the next stage of evolution after a prestellar core and are

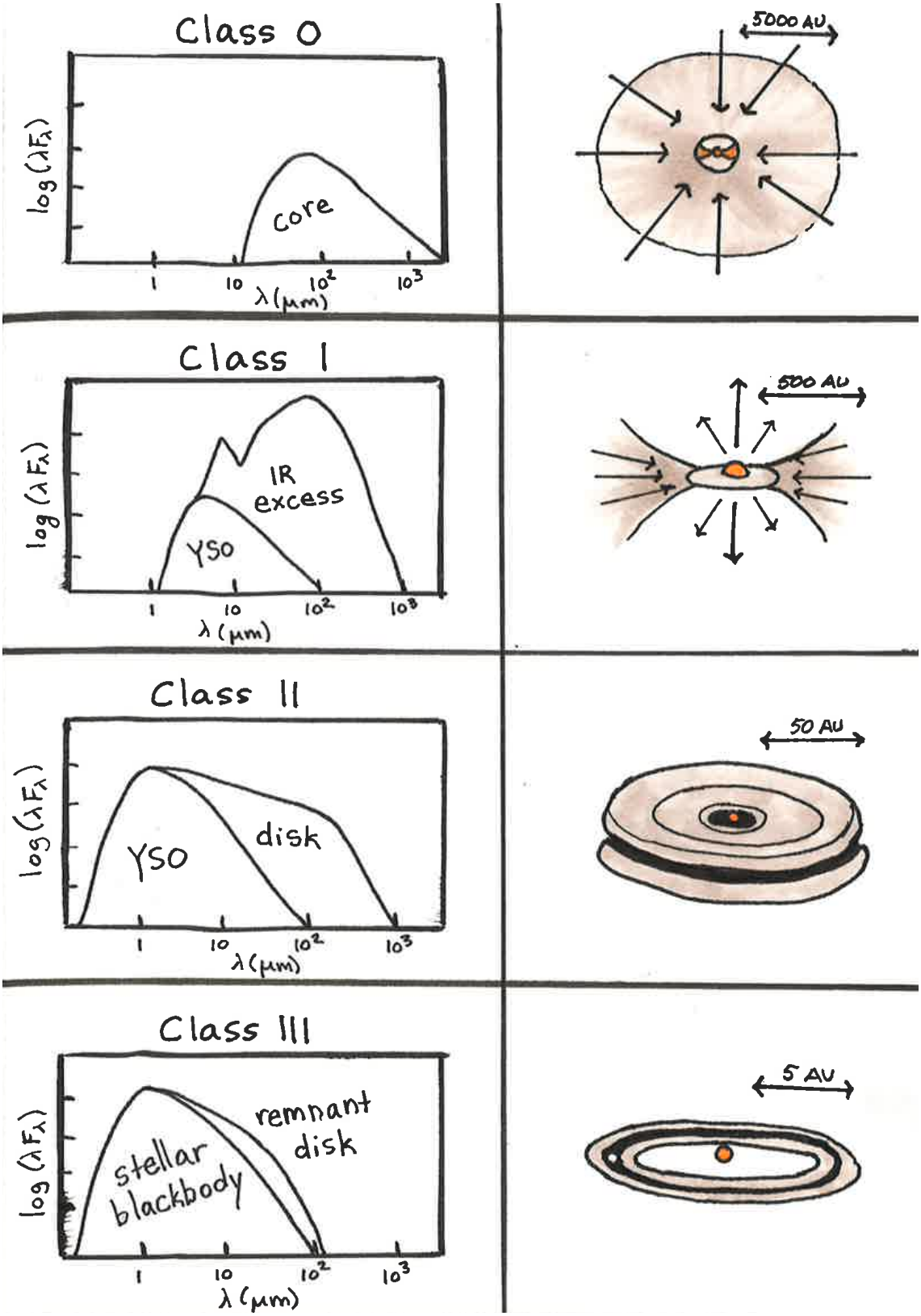

Figure 1.4: Typical spectra and diagrams of YSO classes 0–III. Size of each object is listed in the upper right corner in au. Mauve color stands for surrounding dust and orange is the central YSO. Arrows represent direction of mass transfer. Image by the author, adapted from `http://astronomy.swin.edu.au/~smaddiso/teaching/yso.html` and `http://www.reinervogel.net/index_e.html?/YSO/YSO_e.html`.

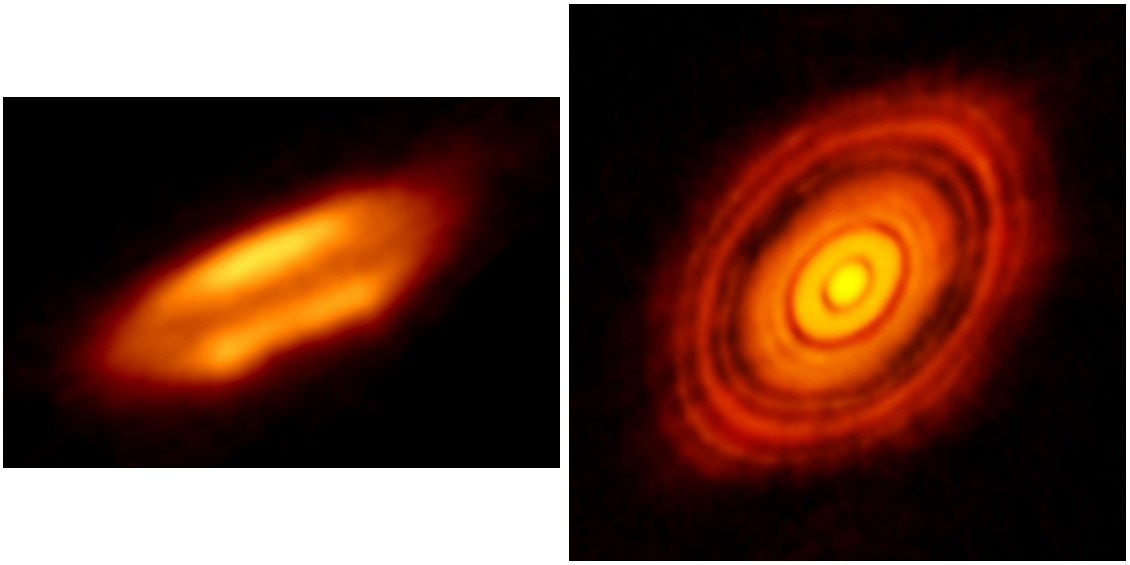

Figure 1.5: *Left:* Extremely young ($\sim$ 40 000 years old) YSO HH 212, located in the Orion nebula and imaged with ALMA. HH 212 is surrounded by its envelope. Credit: ALMA (ESO/-NAOJ/NRAO)/Lee et al. *Right:* ESO ALMA image of the later-stage protoplanetary disk around YSO HL Tauri. Rings show structures which may be indicative of planetary formation. Credit: ALMA (ESO/NAOJ/NRAO)

10^4–10^5 years old. They are not visible in wavelengths shorter than 10 μm and their spectrum resembles a blackbody. At this stage, the protostellar core is in hydrostatic equilibrium, with one or more small central objects surrounded by an envelope [1]. A class 0 protostar has a stellar mass less than its envelope mass.

Class I protostars are around (1–2)$\times 10^5$ years old. Most of their luminosity is due to accretion from their disk and circumstellar envelope (Fig. 1.5, left). Class I protostars often have strong bipolar outflows [1]. Flat-spectrum protostars have a spectral index α between Class I and II protostars, and thus, are likely to be in the final stages of accretion [31].

When observed in the optical, class II protostars are also known as Classical T-Tauri (TT) stars, low-mass stars approaching the MS which will reach a spectral class F or later [32]. As TT stars have no circumstellar envelope, they are the youngest known optically visible stars and have strong emission lines, particularly Hα. Class

II protostars still have a circumstellar disk which may be undergoing planetary formation (Fig. 1.5, right) and are around 10^6–10^7 years old.

When observed in the optical, class III protostars are also known as weak-line TT stars. These YSOs have no circumstellar envelope, but have a weak remnant circumstellar disk [1]. They have significantly less accretion than Class II YSOs.

1.4.1 Star formation rate

The star formation rate (SFR) is defined as the mass of stars formed in a unit of time in a certain area. For the entire Milky Way this is ~0.68–1.45 $M_\odot$/year [33]. The star formation efficiency (SFE) gives the fraction of the mass of an individual MC which is converted into stars.

The SFE per free-fall time of a GMC ($t_{\rm ff}$ ~4 Myr) is quite low, ≤ 0.01, suggesting strong influence of turbulence. However, in low-mass cores, SFE per free-fall time rises to ~ 0.1, showing a dominance of gravity over turbulence. As cores live for a few free-fall times, the total SFE is approximately 1/3 [9].

The Kennicutt–Schmidt law is an empirical relation between SFR and gas density in a galaxy of the form $\Sigma_{\rm SFR} \propto \Sigma_{\rm gas}^N$ where N takes a value of around 1.5 for many galaxies [34, 35]. However, in regions of high or low density, the SFR does not follow the Kennicutt–Schmidt law [36], for example within the Galaxy's central molecular zone, $\sim$ 150 pc from the center, the SFR is only 0.015 $M_\odot$/year [37].

1.4.2 Initial mass function and core mass function

The stellar initial mass function (IMF) describes the mass distribution of stars entering the main sequence as a function of their mass [9]. It is often approximated as a power law $\xi(M) \propto M^{-\alpha}$ dM. The IMF can be estimated by studying the spread in masses of stars in a given region, and taking into account the varying lifetimes of stars and estimating the amount of massive, post-MS stars which would have been

born in the area. For low or high-mass stars the IMF is more poorly known due to observational difficulty [3].

The first estimate of the IMF was the Salpeter IMF, a function which applies in the solar neighborhood, that has an α index of 2.35 [38], and works in an approximate mass range of 1 $M_\odot \leq M \leq 10\ M_\odot$. Kroupa [39] extended this relation to lower masses; $\alpha \sim 1.3$ for 0.08 $M_\odot \leq M \leq 0.5\ M_\odot$ and $\alpha \sim 0.3$ for mass under 0.08 $M_\odot$. Chabrier [40] developed separate IMFs for binaries. Modern IMF models usually approximate the IMF with a lognormal function below 1 $M_\odot$ [3].

It is likely that the mass of forming stars is greatly affected by the core mass function (CMF), the corresponding function for the masses of prestellar cores. This, too, can be approximated with a power law with $\alpha \sim 2$–2.5 for $M \geq 0.5\ M_\odot$and $\alpha \sim 1.5$ for lower masses, with a turnover near 1 $M_\odot$ [3].

1.4.3 High-mass star formation

A high-mass star is defined as one with mass over 8 $M_\odot$. Though rarer than less massive stars, high-mass stars are responsible for the majority of the luminosity of most (SF) galaxies, as well as the dynamics of many molecular clouds. In higher-mass stars, it is often more difficult to separate the stages of stellar formation as these stars have generally begun fusing Hydrogen before accretion is finished. High-mass protostars can spectrally overlap with A and B-type stars, thus they are called Herbig Ae/Be YSOs after their discoverer [32]. These YSOs are of spectral class A or earlier, but with IR excess due to their circumstellar envelopes and dust absorption.

1.5 The aims of this study

The purpose of this thesis is to study the initial states of star formation in a wide range of Galactic environments, from more diffuse, high-latitude fields to dense

molecular clouds in the Galaxy's disk. To achieve this goal, properties of the general ISM and dense clumps contained therein have been studied in 53 fields, located at distances of 0.1–4.5 kpc.

These fields are areas of high column density which have been selected from the Planck Galactic Cold Cores survey (GCC) [41]. They have been imaged in seven far-IR/submillimeter continuum wavelengths: 70, 100, 160, 250, 350, 500, and 850 μm with ESA's Herschel space telescope and the JCMT SCUBA-2 instrument. Denser clumps have been found in the 850-μm data.

In this thesis, I examine the physical characteristics of the clumps, including temperature, mass, and flux. From these, gravitational stability of the clumps is estimated. Using YSO catalogs and gravitational instability, clumps are characterized as starless, prestellar, or protostellar. Protostellar clumps are spatially associated with at least one YSO. Non-protostellar clumps can be considered prestellar if they are gravitationally bound [28]; starless clumps which are not gravitationally bound will generally disperse with time. It is studied whether there are significant differences between the physical properties of protostellar, starless, and prestellar cores. Finally, the accuracy of Bonnor-Ebert and virial analysis is compared and the contribution of the virial terms (Eq. 1.5) within these clumps is qualitatively studied.

2. Observations

The fields studied in this thesis are currently being observed in molecular lines at the Nobeyama 45-m radio telescope in Nagano, Japan. Previous observations in continuum wavelengths, part of the TOP-SCOPE joint survey, are used in this thesis to study SF in these fields. Sources in the TOP-SCOPE surveys have been selected from the Planck Catalog of Galactic Cold Clumps (PGCC). Observations and data reduction described in this section have been performed before the start of this thesis by the Planck Collaboration, the respective principal investigators (PI) of each survey, and their teams.

2.1 Target selection

While studying the cosmic microwave background, ESA's Planck telescope imaged dust emission from interstellar clouds in frequencies between 25 and 1000 GHz across the whole sky [42]. Over 13 000 dense clumps were collected into the PGCC [43], which contains sources at a wide range of distances and galactic latitudes [2].
As one of the main follow-up projects to the PGCC catalog, 2000 cold sources were observed in ^{12}CO and ^{13}CO J=1-0 transitions with the Taeduk Radio Astronomy Observatory (TRAO) telescope for the TOP (TRAO Observations of Planck cold clumps) survey (PI T. Liu). Preference was given to sources with high column density which had also been imaged with ESA's Herschel space telescope, though objects were located across all galactic longitudes [2]. The main follow-up project for the

TOP survey, the SCOPE (SCUBA-2 Continuum Observations of Pre-protostellar Evolution) survey (PI T. Liu) imaged 1000 PGCC fields in 850-μm continuum emission with the James Clerk Maxwell Telescope (JCMT) on Mauna Kea in Hawai'i. The purpose of the TOP-SCOPE joint survey is to study the formation and evolution of dense clumps and filaments in a variety of environments [2].

The sources used for this thesis are those selected from TOP-SCOPE sources for follow-up by the Nobeyama 45-m radio telescope, observations of which are ongoing (PI: Ken'ichi Tatematsu). These sources are being observed in DNC, $HN^{13}C$, N_2D^+, and cyclic-C_3H_2 [44]. Approximately half of these sources have the potential for high-mass SF. The purpose of the Nobeyama survey is to characterize the chemical evolution of the cores and find the earliest signs of SF.

The purpose of this study is to characterize the sources selected for the Nobeyama survey by using SCUBA-2 850-μm continuum data. In addition, most of the sources have data in at least one Herschel continuum wavelength. The primary data used in this thesis thus come from the JCMT and the Herschel space telescope. All imaged fields are shown in Appendix C.1. The regions studied in this thesis are located across the whole sky, though concentrated mostly around the galactic plane. Most of the target fields are located within 1.5 kpc of the Sun and are either associated with nearby molecular complexes or are part of the Perseus, or possibly Carina-Sagittarius, galactic arm [45]. All fields are plotted on the Planck 857 GHz map of the Galaxy in Fig. 2.1.

2.2 SCUBA-2 observations

The JCMT is the world's largest sub-mm range telescope, at a diameter of 15 m [2]. The data from the JCMT uses the SCUBA-2 (Submillimetre Common-User Bolometer Array 2) instrument, which has 5120 bolometers at both 450 and 850 μm. Its main beam size is 13.0 arcsec and effective beam FWHM is 14.6 arcsec at

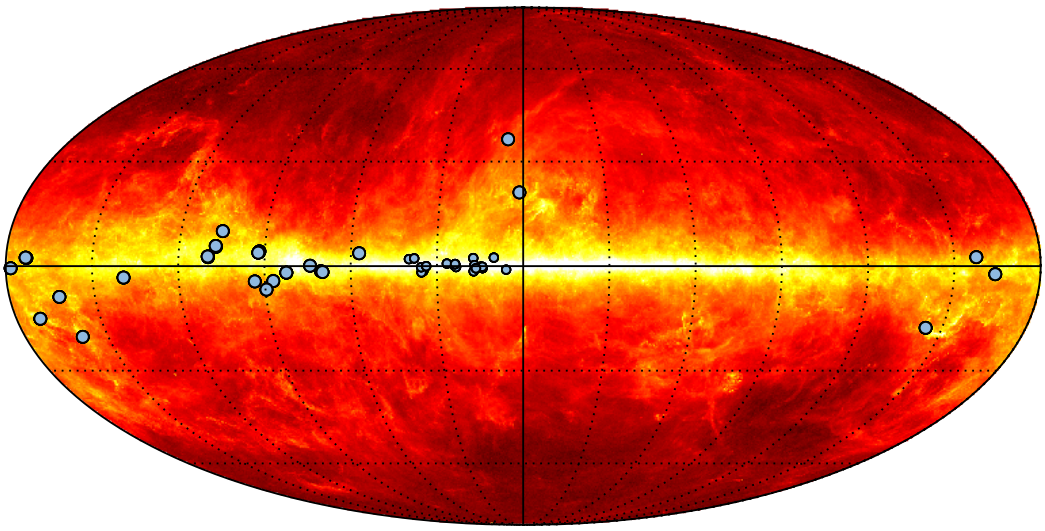

Figure 2.1: Planck image of the Galaxy in 857 GHz, with the 53 fields used in this thesis plotted on top. Fields toward the center of the galaxy are plotted with smaller markers due to overlap. The markers of some fields still overlap at this scale.

850 μm [46]. Its field of view is 45 arcmin^2. Due to its resolution, SCUBA-2 can detect dense cores with size of $\sim$ 0.1 pc to within 2 kpc [2].

Fields were observed with the CV (constant velocity) Daisy scan pattern, which is used for sources up to 12 arcmin in size[1]. Average angular size of PGCC sources is 8'. Average observing time was 16 minutes per field, with noise of 6-10 mJy/beam in the central 3' of the map [2]. Both 850-μm and 450-μm observations were taken, however the 450-μm maps have a high level of noise and are not used in this thesis. Data reduction was performed by Tie Liu et al., using an iterative mapmaking technique as descibed in [47]. This method compares detector beams and removes any low-frequency signals that are correlated between the beams, which removes contamination from the atmosphere but also any large-scale structure above 200 arcsec on a 4-arcsec pixel scale from the resulting surface brightness images [2].

SCUBA-2 data show compact sources with high column densities, and are thus used

[1] `https://www.eaobservatory.org/jcmt/instrumentation/continuum/scuba-2/observing-modes/`

to find dense cores in the fields. The complete list of the SCUBA-2 fields used in this thesis can be found in Appendix B.2. As an example, Fig. 2.2d shows a SCUBA-2 image with two visible dense cores.

2.3 Herschel observations

The Herschel Space Observatory was an ESA IR space telescope which had a 3.5-m diameter main mirror and orbited near the L2 Lagrange point. It finished operations in 2013. Herschel had three instruments: HIFI (Heterodyne Instrument for the Far Infrared), PACS (Photodetector Array Camera and Spectrometer), and SPIRE (Spectral and Photometric Imaging Receiver) [48], however only continuum data was observed for this research. The 250-, 350- and 500-μm data were collected simultaneously using the SPIRE photometer [49] and the 70-, 100-, and 160-μm data were collected using PACS. PACS imaged either 70- and 160-μm or 100- and 160-μm maps simultaneously.

Angular resolution of the Herschel instruments was sufficient to detect cores, though worsened with increasing wavelength, from 5.6 arcsec at 70 μm to 35.4 arcsec at 500 μm. Unlike SPIRE fields, the PACS fields did not have a constant FWHM size due to different scanning velocities, as a faster scan results in elongation of the effective beam. Band characteristics, including resolution, can be found in Table B.8. The differing scan velocities and FWHM resolution for the PACS red (160 μm) band are listed in Table B.9 [50].

The Herschel survey covered 116 fields between 12 arcmin and one degree in size, which in turn covers 390 individual PGCC detections [45], however not every SCUBA-2 field has Herschel data and most have data at only some of the wavelengths.

Herschel data were collected from the Herschel Science Archive [51], and thus they have been reduced by the official pipeline at levels 2.5 or 3. SPIRE maps include intensity zero-point corrections which are obtained from comparison to Planck mea-

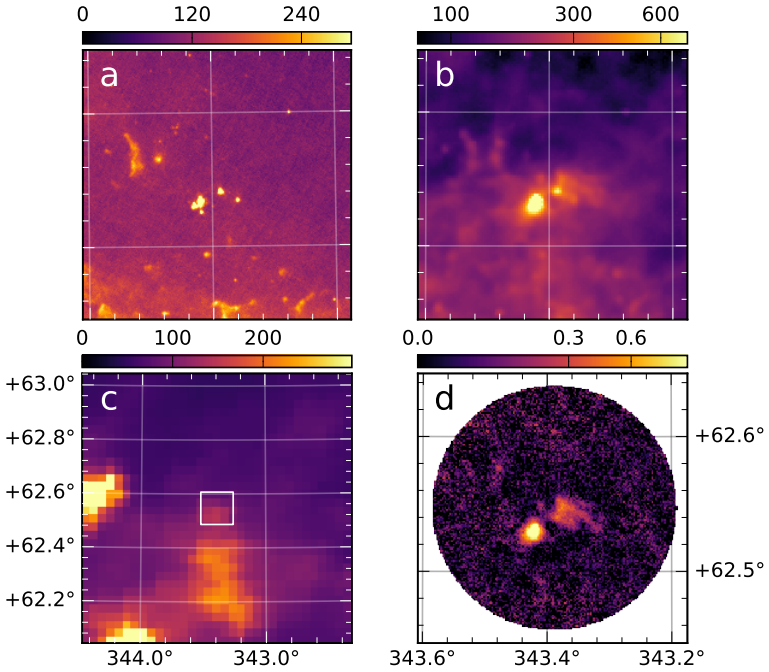

Figure 2.2: Surface brightness maps of field G109.81+02.72, part of the Cepheus molecular cloud, in PACS 70 μm (a), SPIRE 250 μm (b), Planck 857 GHz (c), and SCUBA-2 850 μm (d). The SCUBA-2 map is in units of mJy/arcsec^2, all others are in MJy/sr. The Planck image is 1×1 degrees in size. All other images cover a smaller area of 0.2×0.2 degrees, as indicated by the rectangle drawn on the Planck image. Coordinates are Equatorial (J2000).

surements. PACS images were not zero-point corrected by the pipeline and the data units were later converted from Jy/pixel to MJy/sr. Observation IDs for all fields used in this thesis are provided in Appendix B.1.

Extended emission is visible in the SPIRE observations (Fig. 2.2b), as the SED of cold dust peaks in these wavelengths [52]. SPIRE data are useful for determining cloud characteristics such as temperature and column density. Hotter protostellar sources are visible at shorter wavelengths, with 70- or 100-μm detection being a strong indicator of ongoing YSO formation. Fig. 2.2a shows several protostellar sources at 70 μm which are forming inside the clumps visible in 850 μm (frame d). Due to its low resolution, the original Planck data (frame c) is plotted on a larger scale than the other images.

3. Methods

Herschel fields were cropped to the size of the SCUBA-2 images, as shown for field G006.01+36.74 in Fig. 3.1. Dust properties, including temperature and column density $N(H_2)$ were calculated for each field by fitting a MBB function to a combination of the three Herschel SPIRE images. Distances to each field were found using a variety of methods.

Dense clumps were detected in SCUBA-2 fields using `FellWalker` analysis. YSOs from various catalogs, including Herschel PACS 70 and 100 μm were associated with the clumps.

Properties of clumps, including mass, temperature, and flux, were estimated. Gravitational instability estimation using Bonnor-Ebert analysis was performed and clumps were characterized as starless, prestellar, or protostellar. Finally, virial analysis was used to study the role of turbulence in these sources.

SCUBA-2 fields which have corresponding Herschel fields are listed in Appendix A, input values for the various methods in Appendix B, and figures in Appendix C. The methods are described in detail below and the relevant scripts can be found in Appendices D and E.

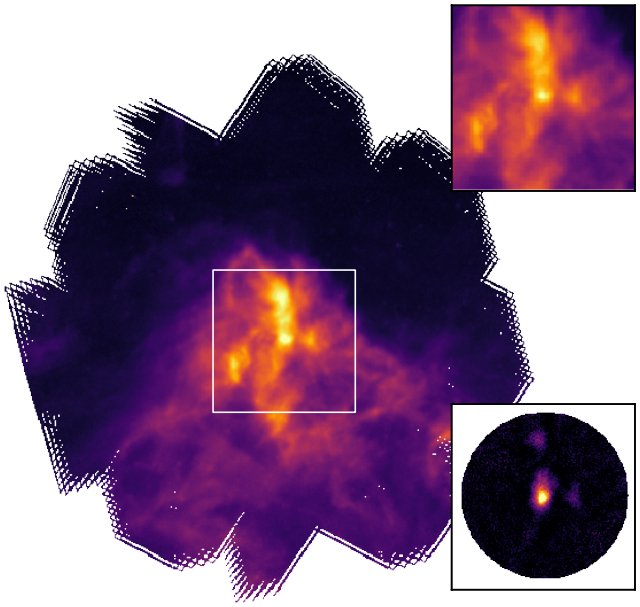

Figure 3.1: *top right* Cropped Herschel 250-μm image, *bottom right* SCUBA 850-μm image overlaid on top of the original Herschel 250-μm image, with white square showing the location of the crop. The field is G006.01+36.74. The original Herschel map is 41 arcmin in diameter, and the smaller fields 12×12 arcmin.

3.1 Derivation of dust temperature and column density maps

To estimate temperature, optical thickness, intensity, and column density of the clouds, a MBB function was fitted to a combination of all three Herschel SPIRE wavelengths. Due to the differing FWHM and pixel sizes of all the bands, (Table B.8), the maps had to be convolved to the lowest common resolution. Resizing was done by first convolving, then reprojecting each image onto the correct pixels. The function `convolve` from the Python library astropy[1] was used for convolution, and the montage[2] function `reproject` for the reprojection. The MBB fit was then performed for each pixel separately.

[1] `http://www.astropy.org/`

[2] `http://montage.ipac.caltech.edu/`

The PACS 70- and 100-μm fields were not used for this routine, as they do not show large-scale structure. Dust properties were analyzed by also including PACS 160-μm data, however shorter wavelengths could bias estimates of dust temperature and spectral index [53], and the resulting maps were of poor quality. SPIRE and PACS fields were not always imaged together, so not every field with SPIRE data also has 160-μm data. The list of matching fields between wavelengths can be found in Appendix A.

Convolution

The 500-μm band has the lowest resolution at FWHM = 35.4 arcsec. In order to calculate temperature and column density maps, the other bands were convolved to its resolution. The convolution function employed a choice of different convolution kernels; a Gaussian 2D kernel was used as the Herschel telescope beam can be approximated with a Gaussian [20]. The FWHM of the convolving kernel is:

$$FWHM = \sqrt{FWHM_{\mathrm{B}}^2 - FWHM_{\mathrm{A}}^2}, \tag{3.1}$$

where $FWHM_{\mathrm{B}}$ is the final resolution and $FWHM_{\mathrm{A}}$ the original resolution. The standard deviation σ corresponding to a given $FWHM$ is:

$$\sigma = \frac{FWHM}{\sqrt{8\ln(2)}}. \tag{3.2}$$

This same function was used for convolving the 250- and 160-μm images to the resolution of the 350-μm, and the 160-μm to the resolution of the 250-μm, in addition to the resolution of the 500-μm images. In case of the 160-μm images, the FWHM differed with scan speed (Table B.9) though a circular beam was still assumed. FWHM and σ for each wavelength combination is listed in Table B.10.

Reprojection

After convolution, images at different wavelengths were reprojected onto the same pixels. Three Herschel fields, G035.19-01.75 and two cropped areas of G013.90-00.51 were at this point removed from this analysis. All these fields were at the edge of the Herschel maps, and did not contain enough data for the convolution function to work (see Fig 3.2).

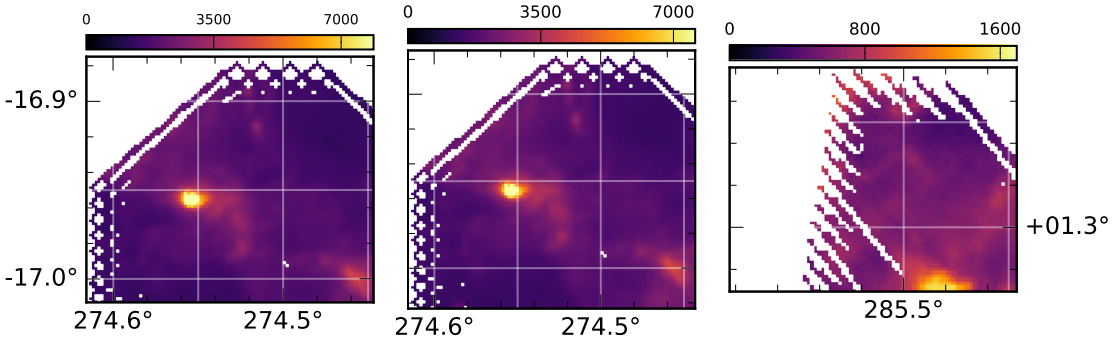

Figure 3.2: (*left and center*) Two cropped areas of field G013.90-00.51, corresponding to SCUBA-2 fields G014.14-00.55 and G014.15-00.55, and (*right*) the field G035.19-01.75, correspoding to SCUBA-2 field G035.38-01.77 in SPIRE 250 μm. The fields are at the edge of their respective Herschel maps and as such were not used in the column density calculations. The maps use Equatorial coordinates (J2000) and the surface brightness is given in units of MJy/sr.

Background removal

As only SPIRE data have been processed to have correct absolute zero points for their surface brightness scale, SPIRE and PACS fields did not have consistent zero-points. Therefore, after reprojection the estimated local background emission was subtracted from all maps at 160–500 μm. The average intensity within a circle of radius 12.0', chosen from an empty area of the field, was subtracted from each pixel in the field. The coordinates of the reference regions are presented in Tables B.5 - B.7. Each set of SPIRE and 160-μm maps corresponding to the same SCUBA field used the same region for zero point determination. Background subtraction was

performed only in the column density calculations that used PACS data (160 μm).

Calculating column density and optical thickness

The script for fitting of the modified blackbody function was provided by Dr. Juvela. The MBB function and its related parameters are discussed in section 1.2.1.

The script performs a least-squares fit on the MBB function (Eq. 1.2), limiting the acceptable solutions to temperatures between 6.9 K and 33 K.

The script creates maps of column density $N(\mathrm{H_2})$, dust color temperature T, optical depth τ, and 250-μm intensity I_{250} at the same wavelength. This map will be referred to in this thesis as the I_{250} map, whereas the original observed 250-μm map will be referred to as the SPIRE 250-μm map. Optical depth at 250 μm was then calculated using the following formula:

$$\tau_{250} = I_{250}/B_\nu(T), \tag{3.3}$$

where I_{250} is the intensity at 250 μm, and B_ν(T) the value of the Planck function at 250 μm for the pixel's temperature T. $N(\mathrm{H_2})$ was then estimated using

$$N(H_2) = \tau_{250}/\kappa_{250}/\mu_{\mathrm{H_2}}, \tag{3.4}$$

where wavelength-dependent values used $\lambda = 250$ μm. The total gas mass per $\mathrm{H_2}$ molecule is $\mu_{\mathrm{H_2}} = 2.8 \times 1.008 \times u$, where u is the atomic mass unit, $1.6605{\times}10^{-24}$ g. κ is assumed to have the form of Eq. 1.3.

3.2 Distance estimates

Distances to the fields could be found in several ways. The distances for 23 fields were estimated in GCCIV [45]. Distances to ten sources could also be found in the PGCC, which was accessed through the VizieR online collection of catalogs [41]. In GCCIV distances were estimated kinematically and by extinction modeling. Extinction modeling compares observed starlight, reddened due to extinction, with the

Besançon Galactic stellar population model to estimate the 3D extinction distribution. Kinematic distances are estimated using radial velocities measured from spectral lines (for example CO J=1-0) and assuming that the gas is in circular orbit with velocities predicted by models of galactic rotation. Finally, distances can be inferred by associating clumps with known sources, for example MC structures for which distances are known [45].

In addition to the distances from literature, I calculated distances to three fields based on a Bayesian distance calculation from [54][3], using ^{12}CO and ^{13}CO line data from Wang et al. [55]. Using a source's galactic coordinates and velocity $v_{\rm LSR}$, this calculator assigns the source with some probability to one of the galaxy's arms, which have known location and velocity. This probability is multiplied by the probabilities calculated through kinematic distance and galactic latitude, resulting in a probability distribution function which can give a fairly accurate location for the source. $v_{\rm LSR}$ values are estimated by eye from the spectra plotted in Appendix C.4. Input values are found in Appendix B.5.1. Distance estimates using all methods are listed in Tables B.11 and B.12.

3.3 Clump analysis

The SCUBA-2 850-μm maps were used to find dense clumps. Properties, including temperature, column density, and mass, were calculated for the clumps.

3.3.1 Clump detection

The program used to find dense clumps in the SCUBA-2 850-μm data is the `FellWalker` algorithm from the Starlink: FindClumps[4] package.

[3] `http://bessel.vlbi-astrometry.org/bayesian`

[4] `http://starlink.eao.hawaii.edu/docs/sun255.htx/sun255ss5.html`

`FellWalker` algorithm

The `FellWalker` algorithm is based on the `CLUMPFIND` algorithm, but developed to work around some problems in its exceution. `CLUMPFIND` is very sensitive to the interval used to create clump contours, especially in crowded regions. `FellWalker` is a watershed algorithm, which uses uphill paths rather than contours to define the clumps [56]. It produces FITS images in which pixels belonging to the extracted clumps are marked with an integer value and all other pixels have a value of NAN (Fig. 3.3). Input values used in the code are shown in Table B.14.

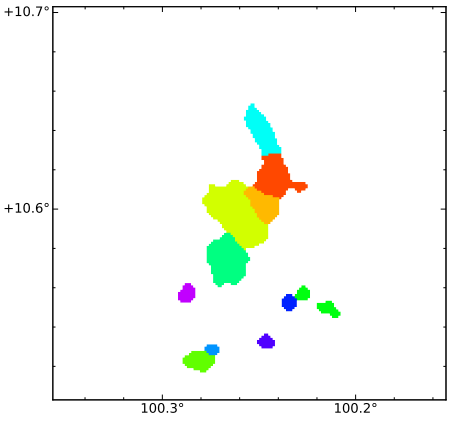

Figure 3.3: Clumps produced by `FellWalker` for field G202.31+02.53.

The RMS variable describes the global RMS noise level in the data. It uses the same reference regions used to estimate the background emssion in Sect. 3.1. The RMS value of the 12' circle was read from ds9[5], but as the resolution of a SCUBA-2 map is twice the pixel size, this rms value was multiplied by two.

When AllowEdge is zero, clumps which touch the edge of the data array are rejected. CleanIter specifies how many times clumps are cleaned, by replacing each clump index with the most commonly occurring value within a 2x2 square. The FWHMBeam variable is the FWHM of the instrument beam, and when deconv=True, the clump widths written to the output file are the deconvolved clump sizes. If the peak value of a clump is less than MinHeight, the clump is rejected. Likewise, a clump with fewer pixels than MinPix is also rejected. Both variables prevent noise peaks from being read as clumps. The noise parameter determines the background level; no pixel with value less than the noise will be considered in a potential clump. `FellWalker` will

[5] `http://ds9.si.edu/site/Home.html`

check the neighborhood around a local maximum for higher pixel values, this area is determined by MaxJump. Adjacent clumps with dip less than MinDip between them will be merged [57].

`FellWalker`, along with `CLUMPFIND` and several other algorithms is included in Starlink's CUPID-package.

3.3.2 Clump characteristics

Clump characteristics were found using Starlink's `EXTRACTCLUMPS` algorithm from the Cupid package. Up to twelve clump properties were derived, either directly with `EXTRACTCLUMPS` or based on those parameters and ancilliary data. The quantities are listed in the following table and the obtained values are listed in Appendix B.9:

Coordinates	Position angle	Effective radius R_{eff}
Flux density F_ν	Temperature T	Intensity at 250 μm I_{250}
column density $N(\mathrm{H_2})$	Mass M	Bonnor-Ebert mass M_{BE}
Bonnor-Ebert alpha α_{BE}	Number of YSOs N_*	Clump type

Coordinates and position angle are given by the `EXTRACTCLUMPS` algorithm.

Average temperature $\langle T \rangle$, surface brightness $\langle I_{250} \rangle$, and column density $\langle N(H_2) \rangle$ over the clump area used the values calculated in Sect. 3.1, only for SCUBA-2 fields with matching SPIRE data. The value of the clump is taken as the mean of the pixels `FellWalker` has assigned to the clump.

The source flux density F_ν is calculated by multiplying the average surface brightness with the clump solid angle, $F_\nu = \langle I \rangle \Omega$.

Finding radius and mass uses the methodology of Liu et al. [2]. Effective radius is calculated using:

$$R_{\mathrm{eff}} = \sqrt{ab},$$

where a and b are the FWHM major and minor axes of the clump in pc.

Masses of clumps were calculated by modifying Eq. 1.2, to:

$$M = \frac{F_\nu d^2}{\kappa_\nu B(T)}, \tag{3.5}$$

where F_ν is the flux density of the clump, d the distance to the field, κ the dust opacity according to Eq. 1.3, and B(T) is the Planck function. For clumps without temperature estimates, the estimated average clump temperature of 13.94 K was used. Mass and effective radius could not be estimated in fields without known distances. 382 clumps in 23 fields do not have estimates for distance.

Bonnor-Ebert mass $M_{\rm BE}$ and gravitational stability $\alpha_{\rm BE}$ is calculated from Eq. 1.10 and 1.11, respectively.

Clumps are classified as protostellar (ps) if they are associated with at least one YSO, prestellar (pre) if $\alpha_{\rm BE} < 2$, or starless (sl) otherwise. The analysis of YSOs is explained in the next section.

3.4 YSO association with clumps

Potential YSOs were found in four archives: Simbad, Akari point-source (PSC) and bright source (BSC) catalogs, Herschel PACS 70-μm and 100-μm catalogs, and the Marton et al. [58] YSO catalog. Sources from different catalogs were merged if their distances were smaller than the data resolution, e.g. 2" for WISE, and were compared to the locations of the clumps.

3.4.1 Catalogs of YSOs

Simbad

Simbad (Set of Identifications, Measurements and Bibliography for Astronomical Data) is a general database for astronomical sources which includes data for several million objects, and is not associated with any specific telescope [59]. It was searched for YSOs and YSO candidates, denoted in the catalog as Y*O and Y*?, respectively.

AKARI

The AKARI IR satellite was in operation from February 2006 to August 2007 and carried out an all-sky survey in six bands (9-160 μm) using two instruments: FIS (the Far-Infrared Surveyor instrument) [60] and IRC (Infrared Camera) [61]. Two catalogs were produced: Akari/IRC PSC which used data from 9 and 18 μm, and AKARI/FIS BSC, based on data from 65-160 μm.

Marton et al. catalog

The Marton [58] catalog, accessed through VizieR, has been compiled from WISE (Wide-field IR Survey Explorer) satellite sources using the AllWISE catalog. Data from the 2MASS catalog and Planck dust opacity measurements were used to classify the YSOs in the catalog. The Marton catalog is divided into two sections: Class I and II YSOs (133 980 rows), and Class III and more evolved YSOs (608 606 rows). Both were used in this thesis.

Herschel PACS point source catalog

The Herschel PACS point source catalogs (hereafter PACS catalogs) include point sources at 70, 100, and 160 μm, as well as extended source and rejected source catalogs [62]. For YSO detection, 70- and 100-μm catalogs were used.

3.4.2 Associating YSOs with clumps

Not all YSOs in a field are physically associated with the detected clumps. The method for choosing clump association was based on spatial matching: YSOs that are located on clumps are most likely also physically associated with the clumps. The coordinates of each YSO were checked against the FITS clump file produced by `FellWalker` (Fig. 3.3). If any of the clump's pixels are within 18 arcsec of a YSO then the YSO is considered associated with that clump and the clump is

characterized as protostellar. If a YSO is near the boundary of two or more clumps, it will be associated with the clump with most pixels within an 18 arcsec distance of it. When no clump's pixels are within the required distance, the YSO is considered a field YSO.

4. Results

The physical clump properties as well as their association with YSOs are presented in this chapter. As sources vary in size, they are referred to as clumps though this sample can contain everything from nearby cores to distant clouds. Uncertainties are discussed in Sect. 4.8.

4.1 Distances of the examined fields

The distances to 28 fields were found in literature, from [41] and [45]. Furthermore kinematic distances to three fields were derived in this thesis. Of the ten distances cited in [41], four were for fields already covered by GCCIV [45]. The distance estimates to all four are consistent within their uncertainties.

I derived new kinematic distances for three fields with available molecular line data using ^{12}CO and ^{13}CO data from [55] and a Bayesian distance calculator (Sect. 3.2), resulting in distances of 0.89 $\pm$ 0.07 kpc for field G105.44+09.88, 0.37 $\pm$ 0.11 kpc for field G159.23-20.09, and approximately 2.5 $\pm$ 0.5 kpc for field G202.31+02.53. Two of the fields, G105 and G159, did not have distance estimates in the literature, but the distance calculated with the linewidth of both molecules was consistent. Field G202 also had an estimate in GCCIV which was not consistent with that estimated through molecular lines; furthermore the distances estimated with ^{12}CO and ^{13}CO lines were different. For this field, the distance estimate from GCCIV was used. The input values and derived kinematic distances are found in Appendix B.5.1.

	Wavelength range (μm)				
	500-250	350-250	500-160	350-160	avg.
$\langle T \rangle$	16.18	17.52	17.12	17.78	17.15
(K)	± 0.83	± 0.94	± 1.25	± 1.28	± 1.08
$\langle N(H_2) \rangle$	6.66	5.18	3.67	4.43	4.98
($\times 10^{21}$ cm^{-2})	± 1.13	± 3.55	± 2.77	± 823.32	± 2.48
$\langle \tau \rangle$	4.49	3.49	2.47	2.98	3.36
($\times 10^{-3}$)	± 0.76	± 2.40	± 1.87	± 554.86	± 1.68
$\langle I_{250} \rangle$	407.72	407.08	130.45	127.78	268.26
(MJy/sr)	± 103.14	± 102.87	± 41.50	± 40.78	± 72.07

Table 4.1: Average values of T, $N(\mathrm{H_2})$, I_{250}, and τ calculated over all fields using fits with different wavelengths. Errors listed are errors of the mean, which are generally smaller than those discussed in Sect. 4.8.

4.2 ISM properties

Intensity, dust temperature, dust optical depth, and the total ISM column density were estimated with the methods described in Sect. 3.1. The values averaged over all fields are listed in Table 4.1 for all combinations of wavelength used in the derivation of these parameters. 27 fields have SPIRE data, 24 both SPIRE and PACS 160-μm data. Background subtraction was not performed on fits involving only SPIRE data. The large errors in τ and $N(\mathrm{H_2})$ for the 160-350 μm combination (column 5) are due to unreliable estimates at the edges of some maps.

The following values represent the averages for each clump using SPIRE 250–500-μm observations. $\langle N(\mathrm{H_2}) \rangle$ over each field ranged from (1.4±0.7) × 10^{21} cm^{-2} to (1.6±0.8) × 10^{22} cm^{-2}, $\langle T \rangle$ from 6.9 K to 35.4 K, and $\langle \tau \rangle$ from 10^{-3} to 0.01. Temperature is anticorrelated with $N(\mathrm{H_2})$, τ, and I_{250} (Fig. 4.1).

Column density maps with SCUBA-2 contours are shown in Appendix C.2.

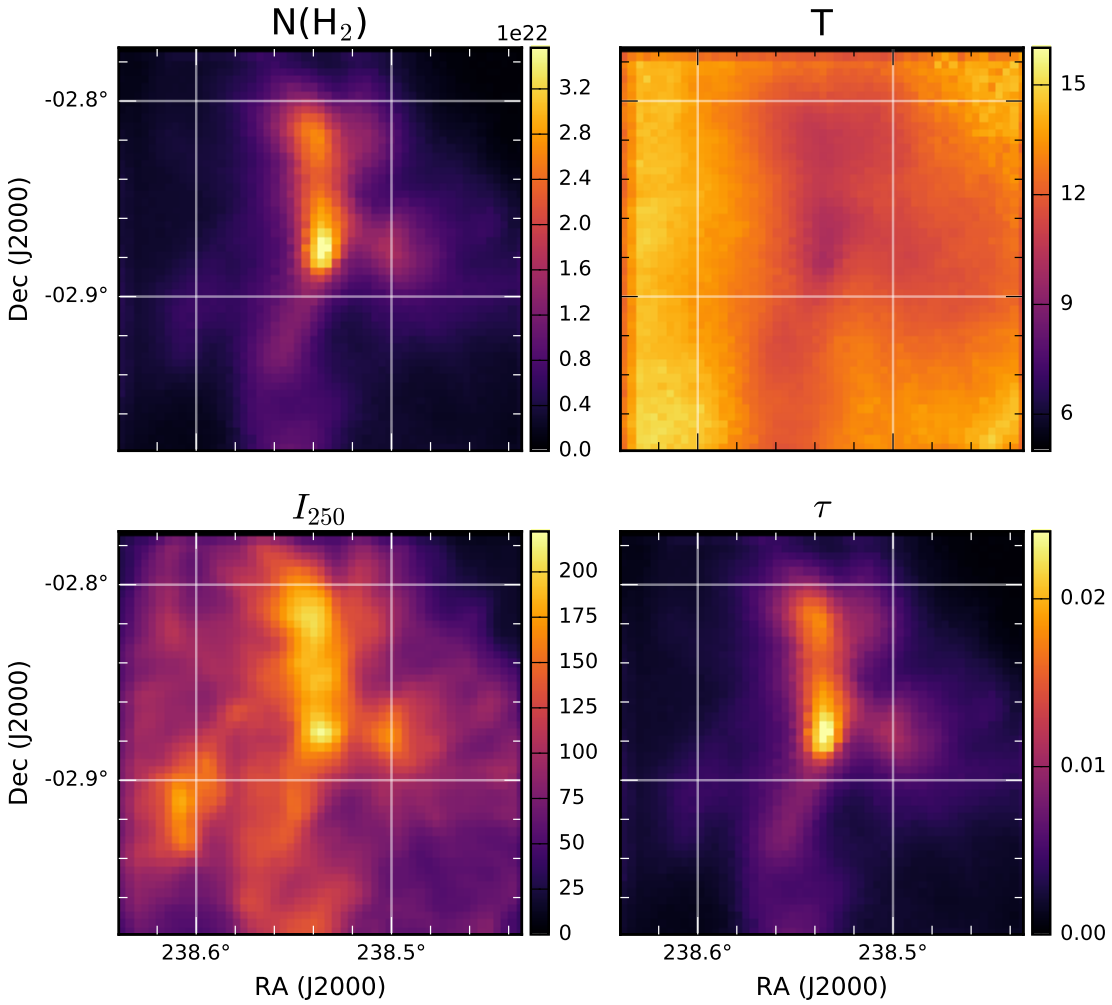

Figure 4.1: Column density $N(\mathrm{H_2})$ (10^{22} cm^{-2}), Temperature T (K), intensity I_{250} (MJy sr^{-1}) and optical thickness τ of field G006.04+36.73, calculated using Herschel SPIRE 250-, 350-, and 500-μm maps (FWHM = 35.4"). The original 250-μm intensity map is shown in Fig. 3.1.

4.3 Detected clumps

The `FellWalker` analysis (Sect. 3.3.1) found a total of 529 clumps in 53 fields. Each field contained between 1 and 35 clumps, with an average of $\sim$ 10 clumps per field. Clumps are generally cold and dense, with temperatures around 14 K and average column density of order 10^{22} cm^{-2}. Clump masses range from 10^{-2} to 10^{3} M$_{\odot}$, with average mass of order 10^{2} M$_{\odot}$. Flux is approximately 2 Jy. The derived properties of these clumps will be discussed further in Sect. 4.6.

4.4 YSO detections

Clumps which are spatially associated with at least one YSO candidate are classified as protostellar, as described in Sect. 3.4.2. YSOs which are not associated with any clump are referred to as field YSOs. Furthermore, YSO candidates regardless of type will be referred to simply as YSOs.

Clumps classified as protostellar should be already undergoing SF. However, it is possible that some clumps have been misclassified, either due to chance line-of-sight alignment of YSOs or misclassification of sources in the catalogs. These possibilities are discussed further in Sect. 5.3. In addition, especially more developed clumps may already have begun to lose mass; thus it is possible that protostellar clumps themselves do not have enough mass to overcome turbulence and thus may not form stars after the current YSOs.

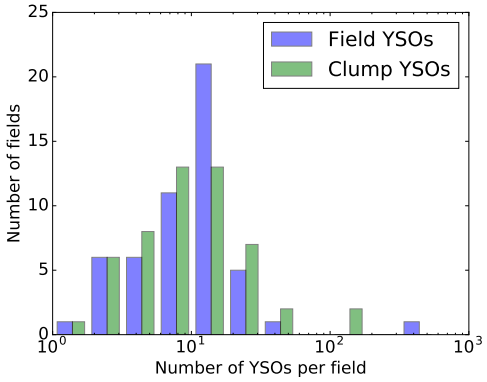

Figure 4.2: The total number of field YSOs in each field (blue) and total number of clump-associated YSOs (green) plotted on a semilog axis.

Fig. 4.2 shows the distribution of clump-associated and field YSOs, showing that

both are equally likely. Just under half (49.7%) of all YSOs located on the SCUBA-2 fields are associated with a clump (Fig. 4.3 (*left*)). Likewise, around 60% of clumps are protostellar, with an average of 1.6 YSOs per clump (Fig. 4.3 (*right*)). The distribution of protostellar clumps in each field is more even above 40%, whereas very few fields have above 70% of YSOs associated with clumps.

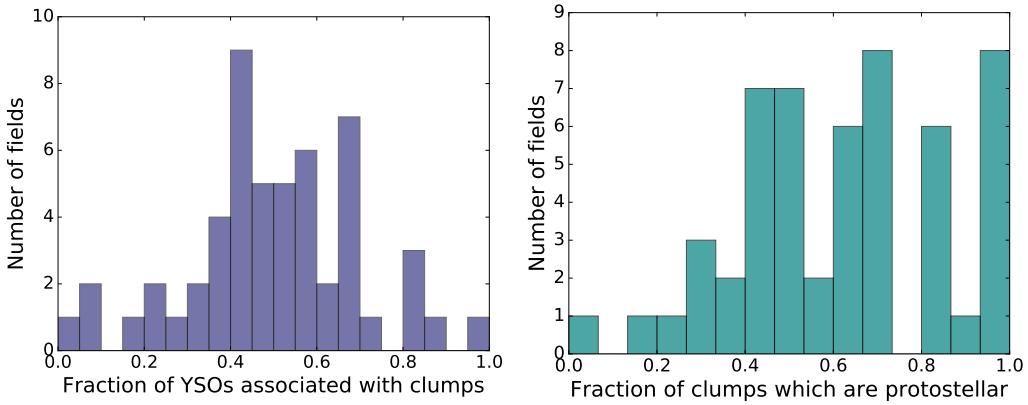

Figure 4.3: *Left:* The fraction of YSO candidates associated with clumps, defined as $N_{*,\mathrm{clump}}$ / $N_{*,\mathrm{tot}}$, per field. *Right:* Fraction of protostellar clumps per field.

4.4.1 Comparison of YSO catalogs

Figure 4.4 studies whether distance affected the type of YSO found, or whether catalogs showed preference for YSOs at a certain distance. YSOs found in several catalogs have not been merged for this image.

The majority of clump-associated YSOs are under 1-kpc distance away (*left*). All YSOs are similarly spread as a function of distance (*right*), though this peak is slightly closer to Earth: 23% of clump-associated but only 12% of field YSOs are located in fields with distance over 1 kpc. Generally, the opposite would be expected; nearby clumps are generally high-latitude clumps, where fewer field YSOs would be expected. Of course, as these are unassociated YSOs, it is possible that they are located at a different distance than the SF region and so the distances listed may be incorrect. The concentration of YSOs around 1 kpc is similar to the distance

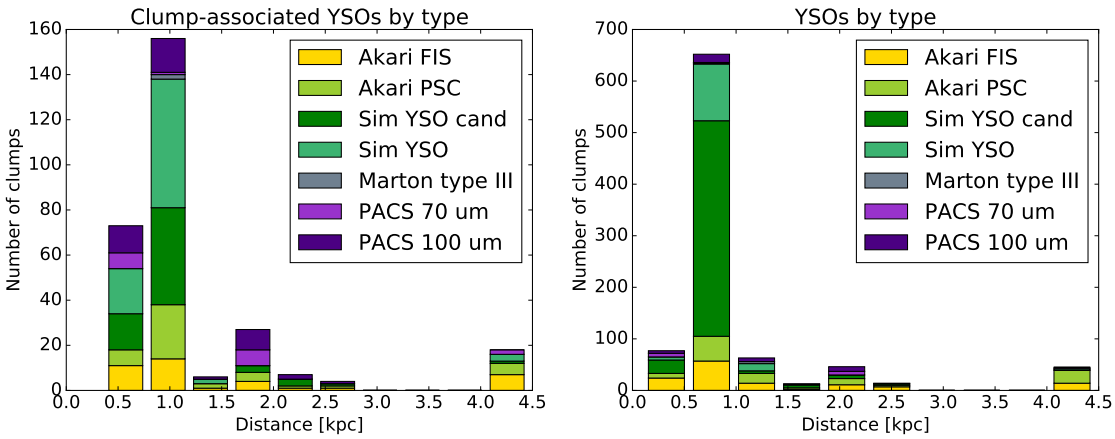

Figure 4.4: *Left:* YSOs associated with the extracted clumps. *Right:* The same, but including all YSOs in the field. The label *Sim YSO cand* stands for Simbad YSO candidates.

dependence of clumps (Fig. 4.7, *top left*). There are no fields, and thus no clumps or YSOs between 3 and 4 kpc. There are also no Class I/II YSOs from the Marton et al. catalog in these fields.

Matches in various YSO catalogs

YSOs that were located within 2 arcsec of each other were merged as a single YSO candidate. The rate of matches between catalogs are shown in the appendices in Table B.15 for clump-associated YSOs and in Table B.16 for all YSOs, including field YSOs. Especially Simbad YSOs and YSO cadidates overlapped with entries in the other catalogs.

4.5 Clump classification

Clumps that have at least one associated YSO are categorized as protostellar. The rest of the clumps are either prestellar or starless, depending on whether they are gravitationally bound. Clumps are classified as prestellar if the ratio between observed and BE mass is $\alpha_{\rm BE} \leq 2$ (Sect. 1.3.1). $\alpha_{\rm BE}$ cannot be estimated without known distance, as mass (Eq. 3.5) depends on the square of distance.

Out of 529 clumps in total, 382 (72%) do not have known distances. Of the remaining 147 clumps with distance estimates, 91 (62%) are classified as protostellar, 55 (37%) prestellar, and 1 (1%) starless. Out of these, 61, 32, and 1, respectively, have corresponsing SPIRE data, and thus column density and temperature estimates.
321 (61%) of all clumps are protostellar, including those without distance estimates. Of the clumps for which it was possible to calculate mass, 98% of non-protostellar clumps are prestellar. For the full sample of clumps, this would suggest approximately 204 prestellar and 4 starless clumps in total.
Average temperature, flux density, column density, and mass are shown in Table 4.2. Histograms for the quantities are drawn in Fig. 4.5.
There is less spread in BE masses than observed masses, no clump has BE mass higher than 15 $M_{\odot}$. As BE mass depends on sound speed (Eq. 1.10) which is nearly constant, the upper limit of BE mass is related to an upper limit of clump size $R_{\mathrm{eff,max}}$. This upper limit is caused by the filtering of extended emission performed on SCUBA-2 data.
Fig. 4.6 plots BE and observed mass for both starless (*blue*) and protostellar (*red*) clumps as a function of α_{BE}. The black dashed bar shows the limit of gravitational instability; starless clumps found under this line are categorized as protostellar. As BE mass is calculated based only on sound speed, it takes into account only thermal, but not turbulent, support. By assuming a certain velocity dispersion, gravitational instability including non-thermal support has been estimated in Sect. 5.5.

4.6 Clump properties

Figure 4.7 shows histograms and correlation of clump distance, aspect ratio, mass, temperature, column density, and volume density. Temperature and column density are derived from the MBB fit to SPIRE data, mass from Eq. 3.5, and density by dividing mass by the three dimensional clump area, mean molecular weight μ and

	T (K)	F_ν (Jy)	$N(H_2)$ ($10^{21}cm^{-2}$)	M ($M_\odot$)
Starless	11.21	0.19	14.70	0.04
Prestellar	13.21	0.99	14.69	82.10
Protostellar	14.37	2.30	13.76	143.42
All	13.94	1.80	14.09	119.50
Uncertainty	± 1 K	10%	50%	80%

Table 4.2: Mean temperature, flux density, column density, and mass of starless, protostellar and prestellar clumps, estimated in Sect. 3.3.2. Only fields with distance estimates are considered. Average temperatures and column densities are further limited to fields with SPIRE data.

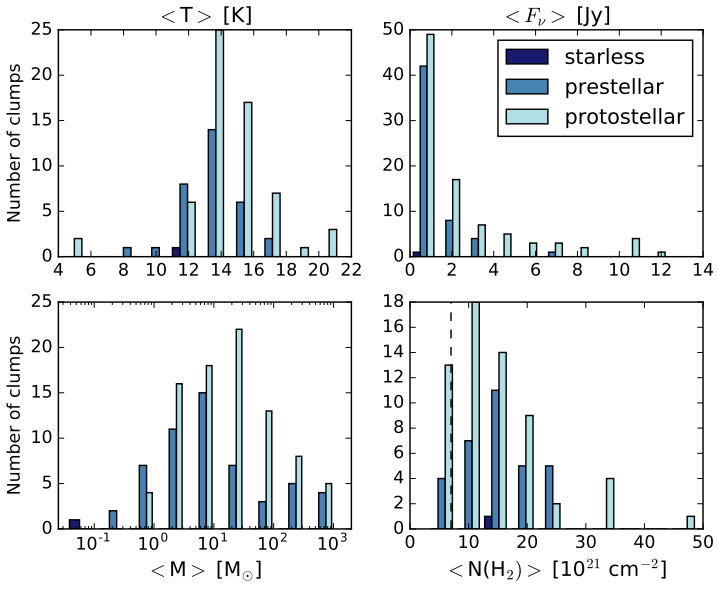

Figure 4.5: Histograms for properties of starless, prestellar, and protostellar clumps. (*Top left*): Average temperature. (*Top right*): Flux density. (*Bottom left*): Mass, plotted on a semi-log scale. (*Bottom right*): Average column density. Dotted line corresponds to visual extinction $A_v = 7$, using Eq. 1.1.

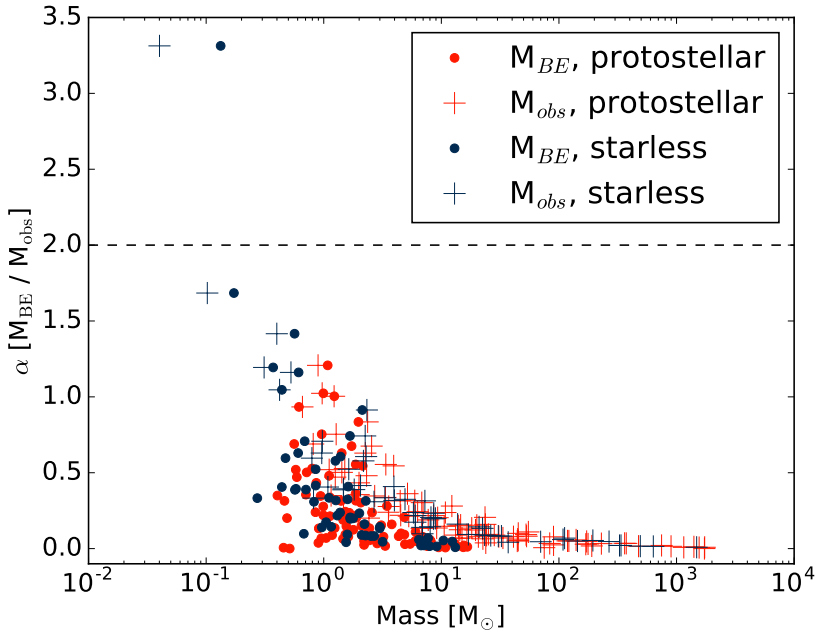

Figure 4.6: α_{BE} (Eq. 1.11) plotted against M$_{BE}$ (*circles*) and M$_{obs}$ (*crosses*) for protostellar (*red*) and starless/prestellar (*blue*) clumps. Black dashed line is the limit for gravitational instability.

atomic Hydrogen mass $m_{\rm H}$ [2]:

$$n = \frac{M}{\frac{3}{4}\pi R_{\rm eff}\mu m_{\rm H}}.$$

There is a peak in the number of clumps at 1 kpc. Mean $N(\rm H_2)$ over all the clumps is (1.4±0.7) × 10^{22} cm^{-2}, corresponding to visual extinction $\langle A_{\rm v}\rangle$ = 14.0 ±7 mag. Using $A_{\rm v,BG} \geq 7$ mag as the threshold for SF, proposed by Könyves et al. [7], approximately 84% of protostellar and 88% of prestellar clumps, as well as the one starless clump, are found above this column density.

The average clump temperatures ranged from 5 to 20 K, with a mean of 13.94±1 K. The few temperatures under 10 K are found in fields G017.23-01.47 and G105.44+09.88, shown in Fig. 4.8, which have clumps located at the edge of Herschel fields; these temperatures are likely to be erroneous.

Clumps have a wide range of masses, from between 0.04 M$_\odot$to 1371 M$_\odot$, with average mass of 119.5 M$_\odot$. Mass of clumps compared to the clump's radius is plotted

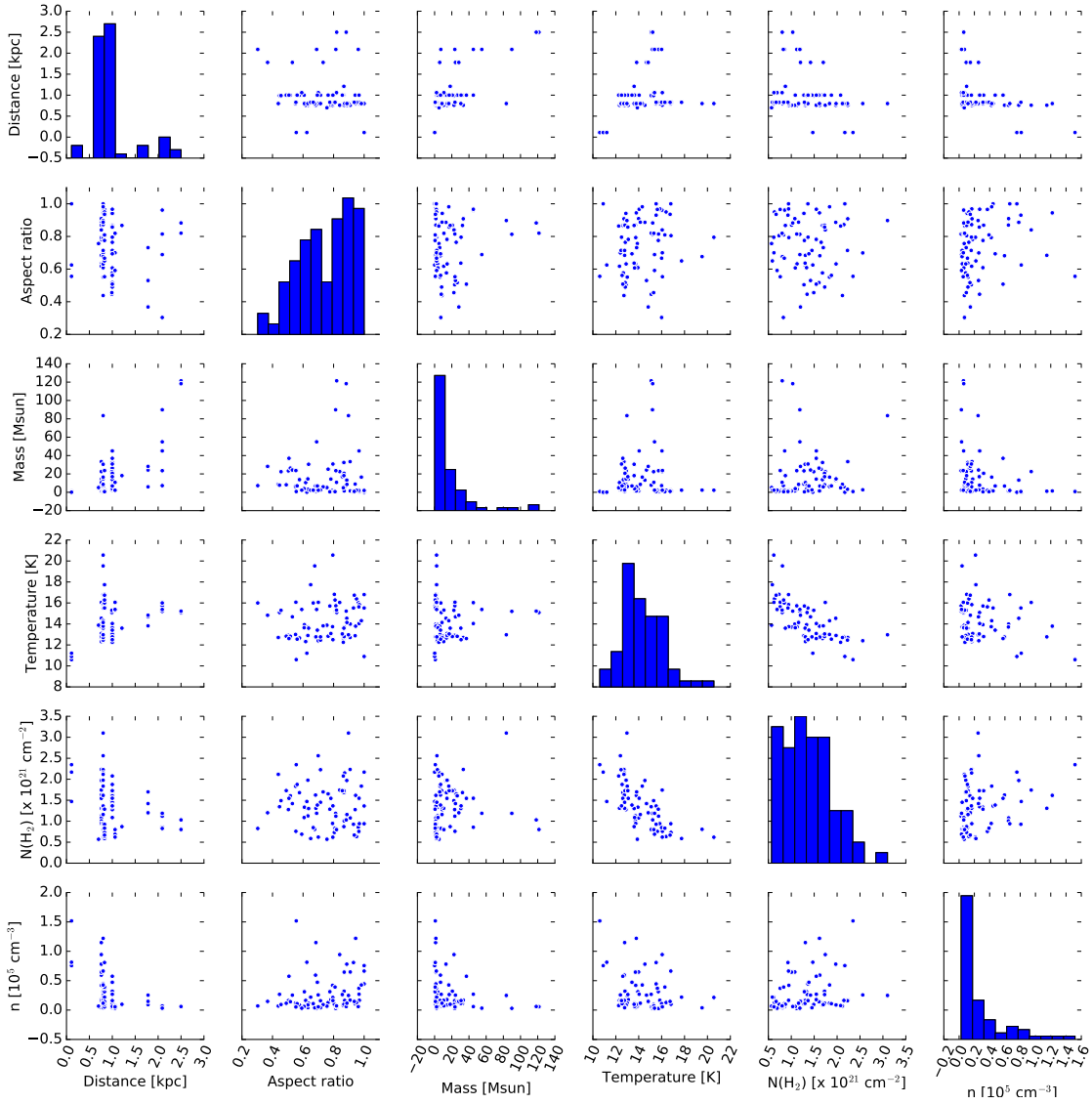

Figure 4.7: Histograms of clump distance, aspect ratio (minor/major axis), mass, temperature, column density $N(\mathrm{H_2})$, and number density n are shown on the diagonal, with scatterplots relating each parameter to each other on the other axes. In this figure, only clumps from the 17 fields with both distance estimates and SPIRE data are included.

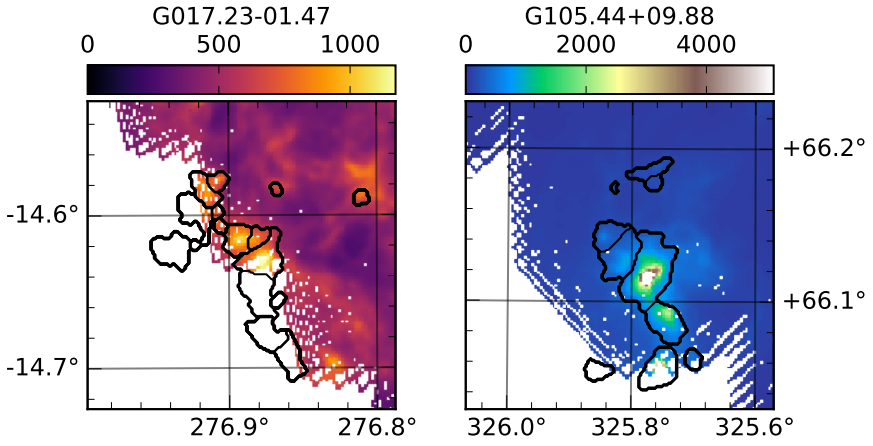

Figure 4.8: FellWalker clump contours plotted on top of Herschel 250-μm images of two fields with clump temperatures under 10 K. As can be seen, these clumps are located at the very edge of the Herschel field. Those clumps located off Herschel fields have no estimate for temperature or column density.

for protostellar, prestellar, and starless clumps in Fig. 4.9 and shows strong linear correlation caused by the angular resolution of the SCUBA-2 instrument.

Clump radius as a function of distance has been calculated using the angular size of clumps, and is plotted in Fig. 4.10. The black line represents the resolution of the SCUBA-2 instrument in parsecs as a function of distance; the deconvolved sizes of some clumps are below the beam size. Radii of the extracted clumps are very strongly correlated with their distance.

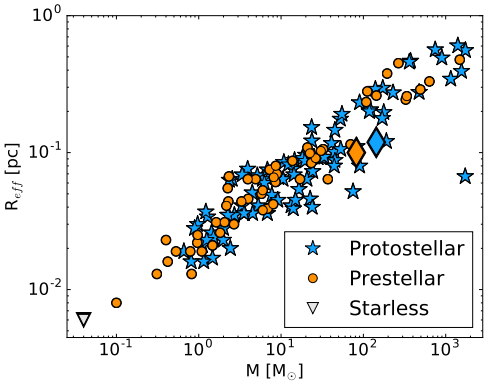

Figure 4.9: Effective clump radius as a function of clump mass. The symbols correspond to protostellar (*blue stars*), prestellar (*orange circles*), and starless (*gray triangle*) clumps. Average mass and radius are plotted with diamonds of the same color.

The average area of a clump is approximately 0.25 arcmin^2. Clumps are generally round, with mean aspect ratio of 0.74 (Fig.

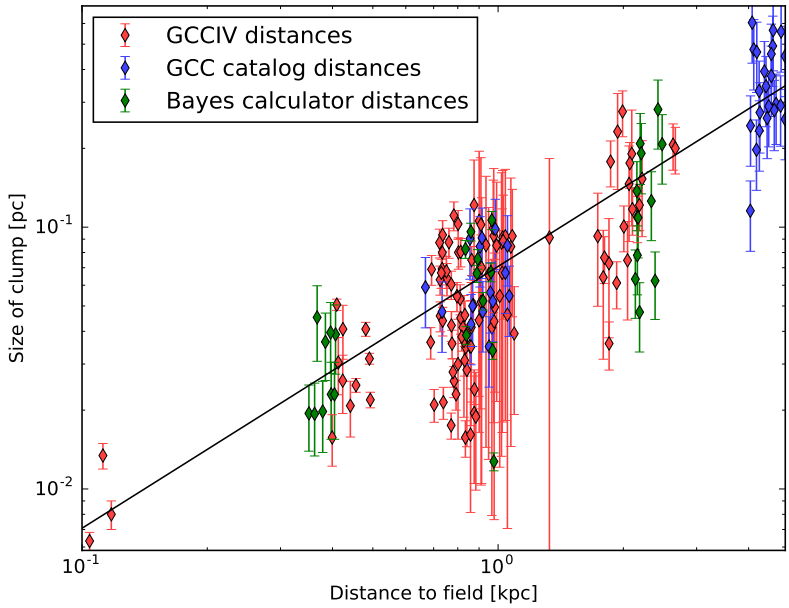

Figure 4.10: Size of the clumps as a function of distance on a log-log scale. The distances are from GCCIV [45] (*red*), the PGCC catalog [41] (*blue*), and the Bayesian distance calculator [54] (*green*). Distance uncertainties are not included for readability, but can be seen from table B.11, and are on average 30%. Random jitter of $\leq$ 10% of distance has been added to distances to improve readability. The black line is the resolution of the SCUBA-2 instrument as a function of distance.

4.7), though this may be caused by many clumps being close to the resolution limit of the SCUBA-2 instrument.

4.7 Virial analysis

Bonnor-Ebert analysis using sound speed only considers the effect of external pressure and gravity. Virial balance (Sect. 1.3.1) also takes into account non-thermal support of clumps against gravitational collapse, though this approximation ignores external pressure. Both approximations are compared in order to study the role of turbulence in these clumps.

To estimate virial mass of a clump, information about the velocity dispersion inside

the clump is necessary. This can be found by analyzing molecular line data. For thirteen clumps in three fields (G105.44+09.88, G159.23-20.09, and G202.31+02.53), ^{13}CO molecular line data from Wang et al. [55] was used for virial analysis.

Virial masses are calculated from Eq. 1.8, using velocity dispersion σ from Eq. 1.9. Here, m is the mass of the ^{13}CO molecule, $m_{^{13}\mathrm{CO}} = 29\,\mathrm{u}$ and kinetic temperature $\mathrm{T_{kin}}$ is substituted by $\mathrm{T_{dust}}$ from SPIRE observations. I assume k=1.333 in accordance with [24]. Though both ^{12}CO and ^{13}CO data existed, ^{13}CO was used as it shows velocities from deeper in the cloud, where denser cores are located. Molecules such as N_2H^+ or NH_3 would have been optimal for this study, as they best probe the densest regions.

Calculated virial masses are presented in Table B.17, where sources with PACS 70- or 100-μm detections are marked with an asterisk (*), though it should be noted that field G105 did not have PACS observations. All of the clumps have an associated YSO from at least one other catalog, thus all are classified as protostellar.

Finally, an estimate for the virial balance of all 147 clumps with mass estimates was performed using average velocity dispersion of the 13 clumps $\sigma_{\mathrm{avg}} = 884.7\ \mathrm{ms}^{-1}$. Mean virial mass is approximately 23.9 $\mathrm{M}_\odot$, with masses ranging between 1.5 and 116 $\mathrm{M}_\odot$. Mean α_{vir} is 3.8, with clumps with $\alpha_{\mathrm{vir}} \leq 1$ classified as prestellar. Of the 13 clumps with ^{13}CO data, 8 (62%) are gravitationally bound. Out of the full sample of 56 non-protostellar clumps, 17 (30%) are prestellar. Extrapolated into the whole sample of 529 clumps, virial analysis predicts approximately 62 prestellar and 146 starless clumps.

Mean temperature, flux density, column density, and mass for starless, prestellar, and protostellar clumps categorized based on virial analysis is shown in Table 4.3 and plotted in Fig. 4.11. The values of protostellar clumps are the same as with BE analysis. Prestellar clumps are the coldest at 12.6 K and have significantly higher column density, almost $2\times10^{22}\ \mathrm{cm}^{-2}$. Mean mass of prestellar clumps is also

	T (K)	F_ν (Jy)	$N(\mathrm{H_2})$ ($10^{21}\mathrm{cm}^{-2}$)	M ($\mathrm{M}_\odot$)
Starless	13.28	0.59	13.71	4.64
Prestellar	12.55	1.87	19.13	254.99
Protostellar	14.37	2.31	13.76	143.42
Uncertainty	± 1 K	10%	50%	80%

Table 4.3: Mean temperature, flux density, column density, and mass of starless, protostellar and prestellar clumps, estimated using virial analysis. Only fields with distance estimates are considered. Average temperatures and column densities are further limited to fields with SPIRE data. Protostellar and overall values (not listed here) are the same as in Table 4.2.

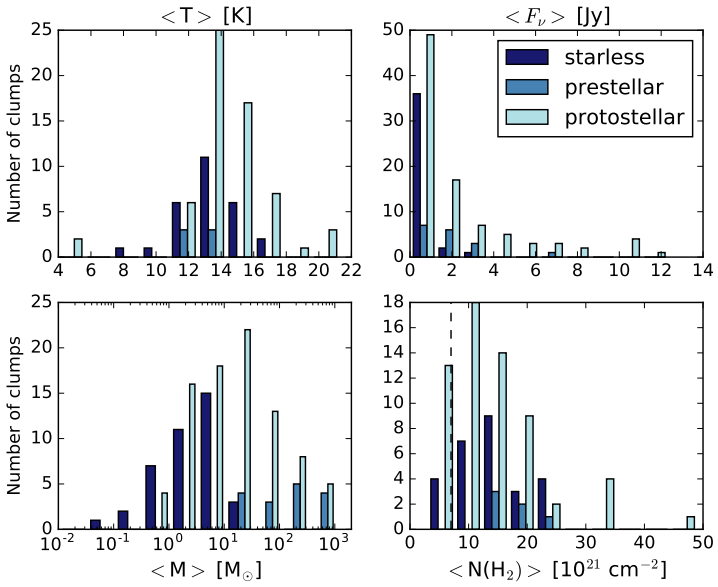

Figure 4.11: Histograms for starless, prestellar, and protostellar clumps, calculated using virial categorization. (*Top left*): Average temperature. (*Top right*): Flux density. (*Bottom left*): Mass, plotted on a semilog scale. (*Bottom right*): Average column density. Dotted line corresponds to visual extinction $\mathrm{A}_v = 7$, using Eq. 1.1. (Compare to Fig. 4.5)

almost twice that of even protostellar clumps. Starless clumps are much smaller and have lower flux than other categories. The histograms show the comparatively large spread in the values of protostellar clumps, whereas both starless and prestellar clumps have lower range. When compared to the mean values of properties of clumps characterized by Bonnor-Ebert analysis (Table 4.2 and Fig. 4.5), certain differences are apparent.

Mean temperature of prestellar clumps has decreased by almost 1 K, whereas starless mean temperature has increased by 2 K. Flux density of prestellar clumps has doubled. Clumps with lower column density are virially classified as starless, meanwhile the mean column density of prestellar clumps has increased by approximately 3×10^{22} cm^{-2}. The most significant change is undoubtedly in mass. Protostellar mass has increased by a factor of three, as the least massive clumps are virially categorized as starless. The mass ratio between prestellar and protostellar clumps has changed: prestellar clumps were approximately half the mass of protostellar clumps as categorized by BE analysis, but virially categorized protostellar average mass is approximately half of average prestellar mass.

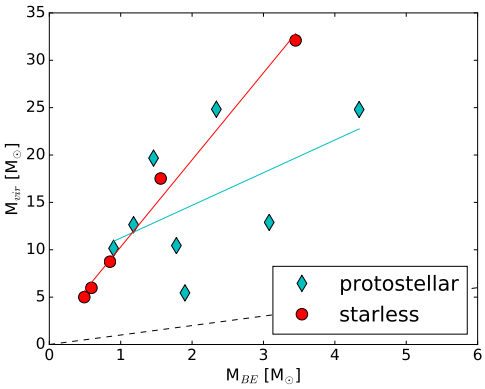

Figure 4.12: Bonnor-Ebert and virial masses plotted for each clump with CO line data. Diamonds are protostellar and circles starless clumps, according to virial analysis. Cyan and red lines are least-squares linear fits (`numpy.polyfit`) to both sets of data. The black dashed line shows where virial and BE mass are equal.

Bonnor-Ebert masses and virial masses are plotted for the thirteen clumps with ^{13}CO data in Fig. 4.12. The same relation is plotted for all 147 clumps in Fig. 4.13a. In both plots, the dashed line shows the situation if Bonnor-Ebert and virial masses are equal ($M_{BE} = 2M_{vir}$). It is clearly seen from

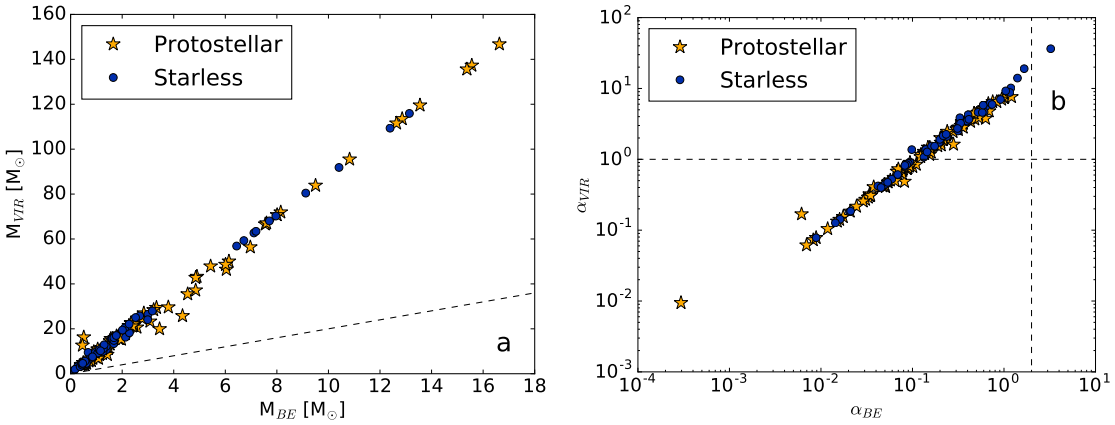

Figure 4.13: (a) Virial mass $M_{\rm vir}$ plotted against Bonnor-Ebert mass $M_{\rm BE}$ for all clumps with distance estimates, using $\sigma_{\rm avg}$. Starless and prestellar clumps are plotted with blue dots, protostellar clumps with orange stars. (b) $\alpha_{\rm vir}$ values plotted against $\alpha_{\rm BE}$ for starless and protostellar clumps on a log-log scale. Dotted lines show limit of gravitational instability, $\alpha_{\rm vir} = 1.0$ and $\alpha_{\rm BE} = 2.0$.

the whole sample that the relation between Bonnor-Ebert and virial mass is linear, $M_{\rm vir} \approx 9 M_{\rm BE}$, over four times that found in previous studies, e.g. [24]. With larger sample sizes, the difference seen in Fig. 4.12 between starless and protostellar clumps is no longer present, but both categories follow the same linear relation.

The difference in Bonnor-Ebert and virial masses is also seen in Fig. 4.13b, which plots $\alpha_{\rm BE}$ and $\alpha_{\rm vir}$ against each other for all 147 clumps. Here, too, the relation is approximately linear. This strong linear correlation is the direct result of the large range of distance in this sample, which directly affects the radius of the clumps on which both BE and virial mass depend. The dashed lines show the limits for gravitational stabillity, $\alpha_{\rm BE} = 2$ and $\alpha_{\rm vir} = 1$; any data points with values higher than these are gravitationally unbound, starless clumps. The much higher ratio of prestellar to starless clumps with Bonnor-Ebert analysis is clearly seen.

4.8 Uncertainties

Intensity uncertainty caused by noise in SCUBA-2 data varies over the map (Fig. 4.14). Error grows radially from the center, and the map has quadrilateral symmetry caused by the DAISY scan pattern used. Formal noise error calculations would require knowledge about pixel correlation. Though pixels are strongly correlated, in the ideal sitution mapmaking processes can lead to spatially uncorrelated noise [47]. Though mapmaking is never ideal and there may be remaining correlated noise, this noise is small compared to mapmaking and calibration errors. I assumed a final uncertainty of 10% across all pixels for SCUBA-2 data, similar to [53].

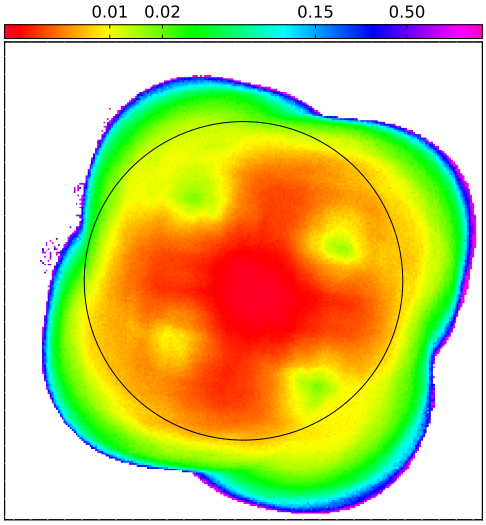

Figure 4.14: Variance map of field G001.36+20.96. The more erroneous lobes are caused by the SCUBA-2 scan pattern. In this thesis, data only from the central 0.09° of the map was used, shown by the black circle.

Both GCCIV and the Bayesian distance calculator provided error estimates for distance, however the PGCC catalog did not. The average distance uncertainty is 30%, which is adopted for all fields.

`EXTRACTCLUMPS` did not provide direct error estimates for the clump coordinates, major and minor axis, and position angle. However, the uncertainties of the linear size are dominated by the uncertainty of the distance, thus 30% error estimates are adopted for effective radius.

The footprint of the clump in pixels is taken as exact, by defining this footprint as "the clump" for which quantities such as mass are calculated. Thus, uncertainty in flux is also directly that of the SCUBA-2 intensity, 10%.

Errors in temperature, τ, I_{250}, and column density are due to errors and noise in the

Herschel maps. Herschel error comes from several sources: calibration uncertainty at ± 5.5% [63], and photometric errors. Total error in Herschel intensities I_{250} is estimated to be below 10%, resulting in temperature errors of the order of 1 K [45]. The uncertainty of the dust opacity κ is at least 50%, leading to a similar undertainty in τ and $N(H_2)$.

Error in mass estimates is dominated by distance, as $M \propto d^2$ though uncertainty in κ, β and flux density have a small contribution as well. Uncertainty in β is taken to be 20%. Altogether, the uncertainty in mass is approximately 80%. As $M_{\rm BE} \propto R_{\rm eff}T$, the uncertainty in Bonnor-Ebert mass is $\sim 30\%$, leading to an uncertainty of 85% for $\alpha_{\rm BE}$. Using the number of prestellar and starless clumps extrapolated for the whole sample, within this uncertainty there are a minimum of 31 (6%) and a maximum of 377 (71%) prestellar clumps, and between 0 and 7 (1%) starless clumps.

As $M_{\rm vir} \propto R\sigma^2$ uncertainties of virial mass are around 100%, leading to uncertainty of $\alpha_{\rm vir}$ of around 130%. This leads to a minimum of zero and a maximum of 143 (27%) virially prestellar clumps, and a maximum of 336 (64%) virially starless clumps in the whole sample.

The number of YSOs depends on a range of factors, including the completeness of the surveys used, on distance, extinction, and YSO class. This error is different for all catalogs. Photometric error may account for misclassification of YSOs, and position error may cause false association with clumps. For Simbad YSOs the uncertainty determination is difficult as sources are gathered from multiple instruments and surveys, and the uncertainty in position varies from 0.1 mas to 1° [59]. In the AKARI/FIS BSC the final position error, including systematic error in calculation of distance, is taken to be 6.0 arcsec [60], and in the AKARI/IRC PSC a mean error of 0.8 arcsec is assumed [61]. The Marton et al. catalog uses data from the AllWISE and 2MASS catalogs, with position uncertainties of 70-130 mas [64] and under 0.5 arcsec [65], respectively. A final position error of 1.5 arcsec has been determined

for the 70- and 100-μm bands in the Herschel PACS catalog [62]. The final error on position is taken as the average of all the errors for the various catalogs. Assuming average error of 1 arcsec for Simbad YSOs, the resulting error on position is approximately 6.3 arcsec. As the circle used to determine YSO association with a clump is 18 arcsec (Sect. 3.4.2), the error in number of YSOs directly resulting from positional uncertainties is approximately 35%.

Field YSOs are potentially erroneous detections. There is an average of 2.6×10^{-3} YSOs per arcsec^2 on the clumps, and 1.1×10^{-4} YSOs per arcsec^2 located on the fields, taking into account a YSO's 6-arcsec position error. As there are approximately 10 times more associated YSOs than field YSOs, 90% of clump-associated YSOs are taken to be real detections. The total error in number of YSOs is thus assumed to be 36%. This results in a lower limit of 172 (33% of all clumps) and an upper limit of 393 (74% of all clumps) protostellar clumps, when taking into account that some clumps are associated with more than one YSO.

5. Discussion

5.1 Field properties

The wide range in distance to fields makes analysis more difficult but also gives the possibility to study SF in various contexts. The clumps in this sample range from cores in nearby fields to entire clouds 4.5 kpc away. The majority of fields are located $\sim$ 1 kpc away, possibly part of the nearby Sagittarius arm if Galactic longitude $\ell \sim 0°$, or the Perseus arm if $\ell \sim 180°$ (Fig. 3 in [66]). Fields in this sample generally have high column density sufficient to be involved in SF. With very few exceptions, dust temperatures are low, showing little effect from internal heating. Temperatures are consistent with those from other GCC studies [53]. Dust opacity spectral index β may vary in the clouds, but likely would not have significant effect on temperatures.

Table 4.1 shows that temperature estimates are highest when estimated from the shortest wavelength combination, 350, 250, and 160 μm. Using only SPIRE in the SED fit data provides the lowest color temperature estimates. The difference between the two combinations is $\sim$ 2 K, twice the formal uncertainty of the temperature estimates.

5.2 Clump properties

Clump properties were estimated from Herschel SPIRE data, though for comparison column density is estimated from SCUBA-2 clump peak intensities in Sect. 5.4. Comparison of the properties of the dense clumps and the general properties of the fields does not produce surprising results (Tables 4.1 and 4.2). Temperatures are 2–3 K lower for dense clumps than for the overall field, and $N(H_2)$ is about three times higher. As clumps are the densest and coldest locations in the ISM, this is to be expected. Due to the large uncertainty in column density, the differences between clumps and the overall field are within the error estimates of the absolute column density values, but are highly significant as relative changes within individual fields. In general the results support previous findings about SF regions. Column densities are somewhat higher than those found by other studies using e.g. Herschel data for finding clumps due to SCUBA-2 sources being selected for high column density.

Temperature

The mean clump temperature of 14 K is consistent with temperature estimates found in nearby regions (e.g Corona Australis, [20], Cepheus [28]). Temperatures are slightly higher than those found in the Lupus cluster [15], though only by a few Kelvin. A few clumps have average temperatures around 20 K, suggesting presence of more evolved YSOs. The maximum temperatures allowed by the MBB code were 33 K, and only a few clumps reached this value. Mean dust temperature has been shown to increase with distance, as more distant low temperature sources are missed [45]. There is a slight increase of temperature in this data as well, seen in the correlation plot in Fig. 4.7. Temperature is also lower for areas with higher column density, as expected. Line-of-sight temperature variations increase color temperature [45], so it is likely that this analysis overestimates the physical dust temperature. This effect worsens with the inclusion of shorter wavelengths such as

PACS 160 μm, thus using only SPIRE wavelengths may give a truer estimate. In the literature the addition of SCUBA-2 850-μm data has been found to also increase temperature estimates by approximately 2 K, though this also depends on assumed spectral index β (Fig. 6 in [53]).

Column density

Könyves et al. [7] found that, according to Herschel observations, 90% of prestellar cores in the Aquila complex are found in regions with $A_v \geq 7$. Bresnahan et al. [20] also found a high rate of association between filamentary structures and prestellar cores in the Corona Australis cloud. In the Taurus MC, 100% of prestellar cores have been found to be located on filaments with $A_v \geq 5$, compared with only 40% of the starless sources, based also on Herschel observations [6]. These studies support the finding of a threshold for SF throughout the Galaxy.

In this sample prestellar clumps show similar relation to high column density. However, protostellar clumps also have a high rate of association with high $N(H_2)$; this is most likely due to the high overall column density of these fields. Generally this threshold applies to background column density, however if a clump is above this threshold, its background cannot be far below. Furthermore it is not possible to calculate background column density associated with unresolved sources.

There is a slight decrease of column density as a function of distance, anticorrelated with temperature. Analysis with SPIRE data alone also results in higher $N(H_2)$ than when shorter PACS wavelengths are included in the SED fit; the average column density estimated using 160–500-μm data is a little over half of that derived using SPIRE data alone (see Table 4.1).

Radius

Due to deconvolution, clumps with estimated sizes below the resolution of SCUBA-2 are still likely real detections, not noise. That distant clumps are larger is due to observational effects: distant small cores will not be detected while large-scale nearby structures are filtered out during SCUBA-2 data reduction.

Other studies also show a linear relation between distance and effective radius. At a distance of 200 pc Sadavoy et al. [10] found clumps with radius $\sim 10^{-2}$ pc. At a distance of $\sim$ 4.2 kpc, Liu et al. [2] found larger radii, around 10^{-1} pc. This is similar to the clumps in this thesis, where cores with distance under 1 kpc generally have radii under 0.1 pc while the most distant clumps are also of radius 10^{-1} pc (Fig. 4.10).

Mass

Previous studies also suggest a relation between observed clump mass and distance. In this data the most massive clumps are also located in the most distant fields whereas the smallest are found in the closest field, G006.01+36.74 (d = 0.1 kpc).

In previous research, typical core masses have been around 0.2 $M_\odot$ in Lupus at a distance of 200 pc [15], and 0.3-1.6 $M_\odot$ in Perseus at the same distance [10], and between 0.03 $M_\odot$ and 10 $M_\odot$ in the Aquila complex at a distance of 300 pc [7]. At a distance of $\sim$ 4.2 kpc, significantly larger masses between 27 and 2000 $M_\odot$ were found by Liu et al. [2]. The larger masses found further away are due to the sources being larger clumps or entire clouds, instead of gravitationally bound cores due to the limit of the instrument beam [45].

The derived masses for these sources thus match the literature quite well. In general, clumps in nearby fields under 1 kpc have mass under 1 $M_\odot$, fitting the definition of cores. The most distant clumps are likely entire clouds, with radius nearer to 1 pc and mass up to 10^3 $M_\odot$. Even considering the large uncertainty of 80%, these results

confirm mass-distance relation ratios found in literature. Fig. 4.7 shows that more massive clumps are also likely to be rounder, whereas smaller cores have a large variation in aspect ratio. Whether this is due to individual clumps being merged or real effects is unclear. In general, the majority of clumps are of mass under 100 $M_{\odot}$, at a mean distance of 1 kpc.

5.3 Star formation in the fields

Over half of YSO candidates located in the fields are not associated with clumps. There are several possibilities for this disassociation: first, that this is a more evolved YSO which has already left the densest cores; a YSO with a relative motion of only 1 kms^{-1} can in 10^5 years travel over 0.1 pc, comparable to the size of a core. Second, for some reason the core may have lower flux and thus not have been found by the `FellWalker` algorithm. There are ISM clouds also outside the clumps found by the algorithm, though typically with lower column densities. Third, some YSO candidates in the catalogs may not be true YSOs.

The third scenario is at least partially responsible for the large number of YSO candidates found outside the clumps. By comparing the left and right sides of Fig. 4.4, one can see that Simbad YSO candidates make up a very large part of field YSOs, whereas in clump-associated YSOs Simbad confirmed YSOs are as common as Simbad YSO candidates. As YSO candidates are those objects which do not have sufficient data to be confirmed as YSOs, they are possibly incorrectly classified sources or false detections.

Fig. 4.4 also shows that the majority of YSOs are under 1 kpc away which follows the distance distribution of fields and clumps. The mean distance of field YSOs is slightly smaller, 1.03 kpc compared to 1.16 kpc for clump-associated YSOs. In addition to the misclassification of sources as YSO candidates discussed above, it is also possible that the YSOs located spatially in the field are not physically anywhere

near the SF regions for which distance is estimated. Association of YSOs to a field is based on two-dimensional projection, and a YSO candidate located parsecs away from a clump may be mistakenly associated with it. This is especially true for fields close to the plane of the Galaxy, which are likely to have several SF regions and IR sources along the line of sight.

5.3.1 Types of clumps

Only 28% of the clumps were located in fields with distance estimates, making full analysis impossible. However, the fraction of protostellar clumps can be estimated for clumps with and without distance estimates; the percentage of protostellar clumps in both categories is $\sim$ 60%. This suggests that an extrapolation of 39% prestellar and 1% starless cores into the whole sample may be potentially representative, though it must be noted that the method for recognizing a protostellar clump is different than that for distinguishing prestellar from starless clumps.

A larger percentage of distant clumps are prestellar, as distant starless clumps are more difficult to detect due to their lower flux [15]. According to the literature, in nearby clouds with distances below 200 pc, around 20% of starless cores were found to be prestellar and 30% of cores to be protostellar [6, 15, 20, 43]. Between 200 and 500 pc, around 60% of starless cores have been found to be prestellar [7, 8]. At distances of $\sim$ 1 kpc, 80–100% of starless sources are prestellar [16, 67]. This trend is also clearly visible in our data; Fig. 5.1 (left axis) shows that α_{BE} is significantly lower, and thus cores are more gravitationally unstable in distant fields.

There are several possible reasons why so few clumps in this data are starless. First, the majority of fields are around 1 kpc in distance, and the results are not so dissimilar to other studies focusing on more distant fields. Furthermore, many of these other studies used Herschel data to find dense cores. Due to its lower sensitivity when compared with Herschel data, SCUBA-2 data show only denser material and

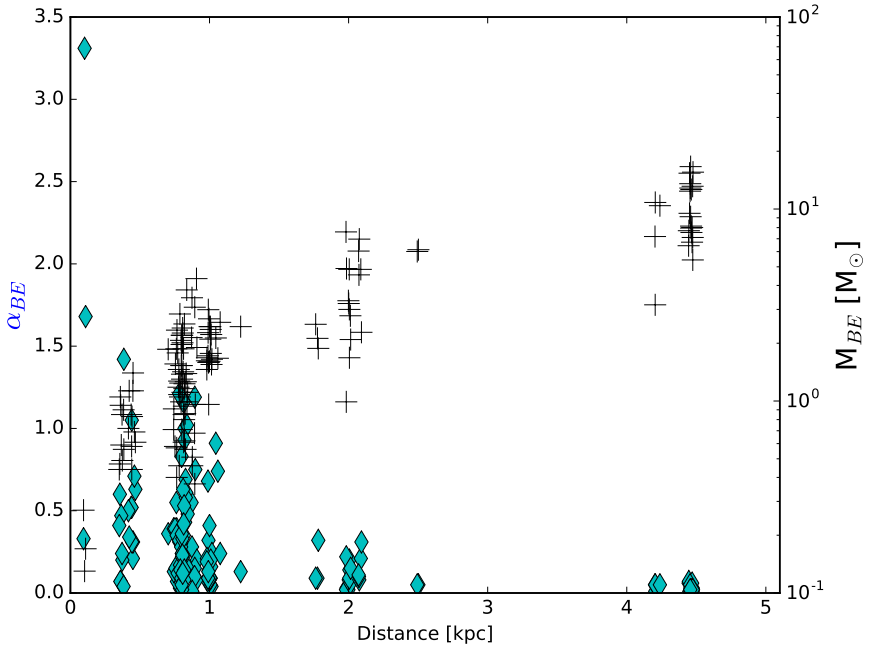

Figure 5.1: Clump α_{BE} (cyan diamonds, left axis) and M_{BE} (black plusses, right axis) plotted as a function of distance.

as starless cores are more diffuse, they may also be less visible in SCUBA-2 images. The possibility of BE analysis being a poor approximation for these sources is discussed briefly in Sect. 5.5.

Differences between clump types

Slight differences have been found between the physical characteristics of prestellar and protostellar clumps. On average, protostellar clumps are hotter by approximately 1 K. Though this is within the error in temperature, the difference is statistically significant ($t = 2.1$, $p = 4\%$)[1]. The difference in flux is also highly significant ($t = 3.3$, $p = 0.1\%$), with the flux of protostellar clumps being higher by a factor of two. The difference in mass, though quite large, is not significant ($t = 1.1$, $p = 27\%$), nor is column density ($t = 0.5$, $p = 57\%$). Due to their large undertainties, differences in both mass and column density fall within the uncertainties of the

[1]Values calculated using the student t-test

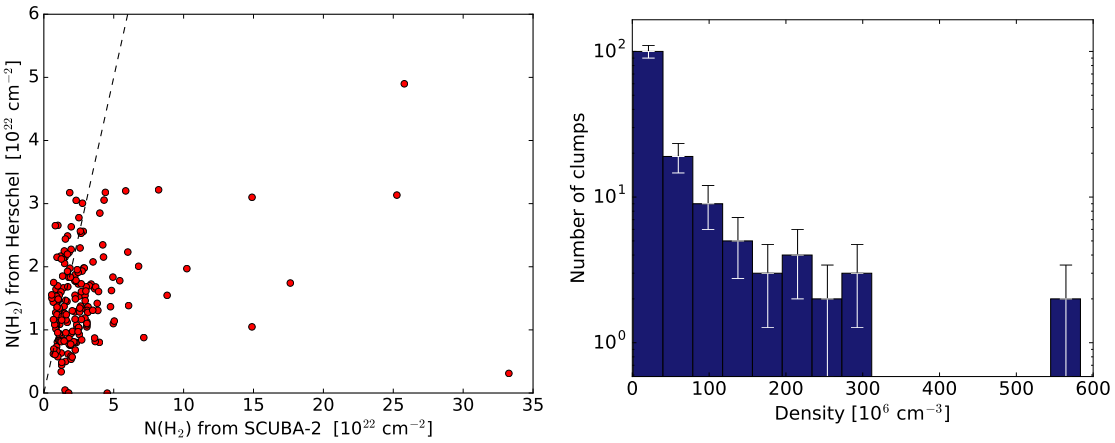

Figure 5.2: *Left:* $N(\mathrm{H_2})$ from Herschel (*y-axis*) plotted against $N(\mathrm{H_2})$ from SCUBA-2 peak values (*x-axis*). The black dotted line shows where both are equal. *Right:* Histogram of peak density of each clump and poisson-distributed uncertainty.

values.

5.4 Column density

By analyzing Herschel data, column densities over the clump area the order of (1.4 ± 0.05)×10^{22} cm^{-2} were estimated. For comparison, peak column densities derived from the higher resolution SCUBA-2 surface brightness measurements, combined with Herschel SPIRE temperature estimates were examined. For clumps without Herschel temperature estimates (or with unrealistically low estimates below 10 K) the mean clump temperature of 13.94 K was used. The peak surface brightness of each clump was provided by the `EXTRACTCLUMPS` algorithm. Column density was estimated by calculating optical depth τ from Eq. 3.3 and $N(\mathrm{H_2})$ using Eq. 3.4. The values are approximately (4 ± 0.2)×10^{22} cm^{-2}, a factor of four higher than those estimated from Herschel SPIRE data (Fig. 5.2, *left*), with maximum of around (5.0 ± 2.5)×10^{23} cm^{-2}. These give a better picture of the densest regions of the cloud. Average density is (6.0±0.7)×10^{7} cm^{-3}, and values range from (1.0±0.6)×10^{6} cm^{-3} to (6.0±3.6)×10^{8} cm^{-3} (Fig. 5.2, *right*) . As these sources may be more extended

along the line of sight than the distance corresponding to a single SCUBA-2 beam, this method likely overestimates the average volume density. However, these high values confirm the sources are likely to be directly involved in SF.

5.5 Virial analysis and the role of turbulence

Comparing the results of Bonnor-Ebert analysis (Sect. 4.5) and virial analysis (Sect. 4.7) shows the difference between the assumptions of fixed sound speed c_s used for BE analysis and velocity dispersion σ, which takes into account the non-thermal motions inside the clumps. Ignoring the effect of turbulent support leads to an underestimation of starless sources. Of the full sample of 529 clumps, 62 (12%) are estimated to be prestellar by virial analysis. In comparison, 204 (39%) of all clumps are classified as prestellar according to Bonnor-Ebert analysis. Previous studies in the Ophiuchus MC have concluded that dense cores are not accurately modeled as critically stable BE spheres [14]. Previous research has also shown that cores which show a large discrepancy between Bonnor-Ebert and virial instability are likely to have significant non-thermal motion [10]. Thus, it can be concluded that these clumps are dominated by turbulence.

38 clumps which are Bonnor-Ebert prestellar are starless according to virial analysis. By comparing Tables 4.2 and 4.3, one can see that clumps which are unbound after the inclusion of turbulence are generally less massive, more diffuse, and warmer than those which remain bound despite turbulence. These results agree with the current understanding of SF.

The virial analysis considered only the first two terms of the virial equation (Eq. 1.5), internal and gravitational energy. Though Bonnor-Ebert analysis does include the effects of external pressure, the errors introduced by the lack of non-thermal effects are too large. Of the clumps which were predicted to be pressure-confined, only the most massive, densest and coldest are virially bound. This is in accordance

with the understood process of star formation.

Previous research has found that external gas pressure is approximately the same order of magnitude as internal energy. There are fewer available measurements of interstellar magnetic fields, however in studies of e.g. the Ophiuchus MC the contribution of magnetic energy has been found to be approximately 5% of that of internal energy [14] and so does not necessarily have a significant effect on SF. Draine [4] however suggests an effect comparable to the effect of turbulence. The strength of the magnetic energy likely depends on location of the field in relation to Galactic magnetic fields and local magnetic sources.

External pressure will aid in a clump's collapse, meaning that clumps which may not have sufficient mass for gravitational collapse may still be pressure-confined. Whether clumps are gravitationally bound or pressure-confined has in the literature been found to depend on their location within the larger ISM [14]. Due to the large effect of external pressure, it is however likely that some of the clumps in this sample are pressure-confined. Thus, the true number of prestellar clumps will likely lie somewhere between the 12% predicted by virial analysis and the 39% predicted by Bonnor-Ebert analysis.

6. Conclusions

The properties of up to 529 dense clumps in 53 fields have been characterized. These fields generally show high column density and low temperature, having little effect from protostellar formation. Fields are located at a wide range of Galactic latitudes, from -20 to +37, and heliocentric distances of 0.1 to 4.5 kpc.

Due to the wide range of distances, clumps may be in any form from small, nearby cores to entire clouds. Clumps have been classified as protostellar, prestellar, or starless, with protostellar sources having at least one associated YSO, and prestellar sources being gravitationally bound. Boundness was determined using Bonnor-Ebert analysis but could only be performed for those clumps with distance estimates. Of these 147 clumps, 62% are protostellar, 37% prestellar, and 1% starless.

Mean temperature $\langle T \rangle$ of dense clumps is 13.94 K, with prestellar clumps having $\langle T \rangle = 13.2$ K, and protostellar clumps $\langle T \rangle = 14.4$ K. Temperature estimates are generally accurate to 1 K. Clump masses range from 0.04 ± 0.03 $M_\odot$ to 1735 ± 1388 $M_\odot$, with larger clumps being located futher away. Mean mass of prestellar clumps is 82 ± 26 $M_\odot$, whereas protostellar clumps are larger with mean mass of 143 ± 26 $M_\odot$. Effective radius also shows a similar spread, with nearby clumps ($d \leq 1$ kpc) having radius under 0.1 pc, while more distant clumps ($d \geq 4$ kpc) have radius up to 0.6 pc, with uncertainty $\pm$ 30%.

Based on Herschel observations, average column densities over the extracted clumps are around $(1.0 \pm 0.05) \times 10^{22}$ cm^{-2}, being highest for prestellar clumps. Deriva-

tion of column density from SCUBA-2 850-μm peak intensity at the full SCUBA-2 resolution shows $\langle N(H_2)\rangle$ four times higher, with the densest clumps reaching $(5 \pm 2.5)\times10^{23}$ cm^{-2}.

Lack of data has affected the scope of this study. Only 28% of clumps have estimates for distance, and only 64% of these clumps are located in fields with corresponding Herschel SPIRE data. With only one starless core, it is impossible to do statistical analysis. This one starless core is the smallest of the sample, and has a temperature of 11.2 ± 1 K and low flux of 0.19 ± 0.02 Jy. Its column density, however, is higher than the mean of protostellar or prestellar clumps.

When compared to protostellar clumps, prestellar clumps generally have lower range in temperature, flux, and column density. Mass, temperature, and flux are higher for protostellar clumps, but column density is lower, probably as protostellar clumps have already begun to lose mass.

Thirteen clumps in three fields had available ^{13}CO molecular line data. With similar data for all clumps, gravitational instability could be estimated by taking non-thermal turbulent support into account in the virial analysis. For the 13 clumps, virial analysis was performed. The average velocity dispersion from these 13 clumps was used to estimate virial stability for all 147 clumps with estimates of mass, leading to an estimate of 62% protostellar, 12% prestellar and 27% starless clumps in the whole sample. This shows the importance of non-thermal support discussed in Sect. 5.5. Furthermore, the clumps which were categorized as prestellar by both methods are the most massive, coldest, and densest clumps in the samples. Clumps classified as starless by virial analysis are the least massive, but have higher column density than protostellar clumps.

The addition of the Nobeyama spectral line data will include signal from deeper inside the clouds, so a more thorough picture of these sources will be known after the data have been studied. With molecular line data for all fields, an estimate

could be made for distance, and thus, for mass of all 529 clumps. Further studies on these regions, which take into account the source's local environment and include data from molecular lines, will increase our understanding of star formation across the Galaxy.

A. SCUBA-2 and corresponding Herschel fields

SCUBA-2 fields and their corresponding Herschel matches are shown in tables A.1-A.3. An X signifies a Herschel field, a - means that a corresponding Herschel field does not exist.

SCUBA-2 field	Herschel			
	SPIRE	PACS 160 μm	PACS 100 μm	PACS 70 μm
G001.36+20.96	-	X	-	X
G005.93-01.00	-	X	-	X
G006.01+36.74	X	X	X	-
G010.21+02.40	X	X	X	-
G014.14-00.55	X	X	-	X
G014.15-00.55	X	X	-	X
G014.22-00.19	-	X	-	X
G014.72-00.19	-	X	-	X
G014.73-00.19	-	X	-	X

Table A.1: SCUBA-2 field, with its matches in SPIRE (250, 350 and 500 μm) and PACS wavelengths. Table 1/3

SCUBA-2 field	Herschel			
	SPIRE	PACS 160 μm	PACS 100 μm	PACS 70 μm
G016.28-00.45	X	X	-	X
G016.37-00.61	X	X	-	X
G016.43-00.62	X	X	-	X
G016.97+00.28	X	X	-	X
G017.23-01.47	X	-	-	-
G017.38+02.26	-	-	-	-
G023.35-00.26	-	X	-	X
G023.68+00.58	-	X	-	X
G023.69+00.58	-	X	-	X
G024.04+00.27	-	X	-	X
G026.54+00.72	-	X	-	X
G033.73-00.01	-	X	-	X
G034.74-01.39	-	X	-	X
G035.38-01.77	X	X	-	X
G035.50-00.31	-	X	-	X
G037.93+02.18	X	X	X	-
G039.74+01.98	X	X	X	-
G057.12+03.63	-	-	-	-
G069.81-01.67	X	X	X	-
G070.40-01.40	X	X	X	-
G074.13+00.11	-	X	-	X
G082.40-01.84	X	X	X	-
G082.42-01.84	X	X	X	-

Table A.2: SCUBA-2 field, with its matches in SPIRE (250, 350 and 500 μm) and PACS wavelengths. Table 2/3

SCUBA-2 field	Herschel			
	SPIRE	PACS 160 μm	PACS 100 μm	PACS 70 μm
G087.07-04.20	X	X	X	-
G089.66-06.62	X	X	X	-
G091.88+04.17	X	-	X	-
G092.04+03.92	X	X	X	-
G092.28+03.79	X	X	X	-
G093.51-04.31	X	X	X	X
G105.44+09.88	X	-	X	-
G107.18+05.44	-	X	X	-
G107.26+05.71	-	X	X	-
G109.70+02.52	X	X	X	X
G109.81+02.72	X	X	X	X
G139.14-03.23	X	X	X	-
G159.23-20.09	X	X	X	X
G162.46-08.69	-	X	-	X
G171.53-14.91	-	X	X	X
G172.89+02.28	-	-	-	-
G173.15+02.40	-	X	X	X
G178.28-00.60	X	X	-	X
G195.73-02.28	X	X	X	-
G202.31+02.53	X	X	X	-
G215.87-17.50	-	-	-	-

Table A.3: SCUBA-2 field, with its matches in SPIRE (250, 350 and 500 μm) and PACS wavelengths. Table 3/3

B. Data

Observation IDs for all the observations (Tables B.1 - B.4)

Coordinates of the center of the maps as well as the centers of the areas used for background removal (Tables B.5 - B.7).

SPIRE instrument specifications (Tables B.8 - B.9)

Convolution kernels (Table B.10)

Distances to the sources (Tables B.11 - B.12).

Bayesian distance calculator inputs (Table B.13)

FellWalker code input parameters (Table B.14)

Virial analysis (Table B.17)

Clump characteristics (Table B.18 onwards.)

B.1 Observation IDs

SCUBA 850-μm data have two project IDs: M16AL003 and M15AI05. M16AL003 corresponds to the SCOPE survey, M15AI05 to data collected during the pilot program. Only one field, G074.13+00.11, is part of the pilot program; all other SCUBA-2 850-μm data have a project ID of M16AL003.

Herschel observation IDs are listed in Tables B.1-B.4.

70 μm			
Filename	proposal	Filename	proposal
G001.15+21.18	OT1_ jhatchel_ 1	G035.09+00.13	KPOT_ smolinar_ 1
G006.52+00.14	KPOT_ smolinar_ 1	G074.71+01.07	OT2_ smolinar_ 7
G013.12+00.14	KPOT_ smolinar_ 1	G093.77-04.74	KPGT_ pandre_ 1
G013.91-00.51	KPGT_ okrause_ 1	G109.86+02.75	OT1_ tmegeath_ 5
G014.64-00.77	KPGT_ fmotte_ 1	G109.88+01.23	OT2_ smolinar_ 7
G015.32+00.14	KPOT_ smolinar_ 1	G110.04+02.39	OT1_ rgutermu_ 1
G016.96+00.75	KPGT_ fmotte_ 1	G110.16+02.70	OT1_ tmegeath_ 5
G017.12+00.45	KPGT_ fmotte_ 1	G158.80-20.65	KPGT_ pandre_ 1
G017.52+00.14	KPOT_ smolinar_ 1	G159.21-20.11	KPGT_ pandre_ 1
G021.91+00.14	KPOT_ smolinar_ 1	G160.40-18.02	KPGT_ pandre_ 1
G024.11+00.14	KPOT_ smolinar_ 1	G162.07-08.79	OT1_ pharve01_ 3
G024.42+00.04	Calibration_ pvparall_ 3	G171.50-14.91	OT1_ jpatienc_ 1
G026.31+00.14	KPOT_ smolinar_ 1	G173.16+02.36	OT2_ jstutzki_ 3
G026.54+00.62	KPGT_ mgroen01_ 1	G173.40-14.08	KPGT_ pandre_ 1
G032.90+00.14	KPOT_ smolinar_ 1	G178.41-00.69	OT1_ rsahai_ 4
G034.87-01.05	KPGT_ fmotte_ 1	G178.12-00.02	OT1_ smolinar_ 5

Table B.1: Observation IDs for Herschel PACS 70-μm maps.

100 μm			
Filename	proposal	Filename	proposal
G006.04+36.73	KPOT_ mjuvela_ 1	G093.79-04.60	KPGT_ pandre_ 1
G010.20+02.39	KPOT_ mjuvela_ 1	G105.60+10.30	KPOT_ mjuvela_ 1
G013.91-00.51	KPGT_ okrause_ 1	G107.36+05.45	SDP_ mjuvela_ 3
G037.91+02.17	KPOT_ mjuvela_ 1	G109.79+02.70	SDP_ mjuvela_ 3
G039.61+01.85	KPOT_ mjuvela_ 1	G139.48-03.27	KPOT_ mjuvela_ 1
G069.71-01.70	KPOT_ mjuvela_ 1	G158.87-20.77	KPGT_ pandre_ 1
G070.22-01.50	KPOT_ mjuvela_ 1	G171.49-14.91	OT1_ mdunham_ 1
G082.74-01.99	KPOT_ mjuvela_ 1	G173.16+02.36	OT2_ jstutzki_ 3
G087.07-04.08	KPOT_ mjuvela_ 1	G195.74-02.29	KPOT_ mjuvela_ 1
G089.77-06.83	KPOT_ mjuvela_ 1	G202.16+02.64	KPOT_ mjuvela_ 1
G092.12+03.88	KPOT_ mjuvela_ 1		

Table B.2: Observation IDs for Herschel PACS 100-μm maps.

160 μm			
Filename	proposal	Filename	proposal
G001.15+21.18	OT1_ jhatchel_ 1	G089.77-06.83	KPOT_ mjuvela_ 1
G006.05+36.72	KPOT_ mjuvela_ 1	G092.12+03.88	KPOT_ mjuvela_ 1
G006.52+00.14	KPOT_ smolinar_ 1	G093.78-04.74	KPGT_ pandre_ 1
G010.20+02.39	KPOT_ mjuvela_ 1	G093.79-04.60	KPGT_ pandre_ 1
G013.12+00.14	KPOT_ smolinar_ 1	G105.60+10.31	KPOT_ mjuvela_ 1
G013.91-00.51	KPGT_ okrause_ 1	G107.36+05.45	SDP_ mjuvela_ 3
G014.64-00.77	KPGT_ fmotte_ 1	G109.79+02.70	SDP_ mjuvela_ 3
G015.32+00.14	KPOT_ smolinar_ 1	G109.86+02.75	OT1_ tmegeath_ 5
G016.96+00.75	KPGT_ fmotte_ 1	G109.88+01.23	OT2_ smolinar_ 7
G017.12+00.45	KPGT_ fmotte_ 1	G110.04+02.38	OT1_ rgutermu_ 1
G017.52+00.14	KPOT_ smolinar_ 1	G110.16+02.70	OT1_ tmegeath_ 5
G021.91+00.14	KPOT_ smolinar_ 1	G139.48-03.27	KPOT_ mjuvela_ 1
G024.11+00.14	KPOT_ smolinar_ 1	G158.80-20.65	KPGT_ pandre_ 1
G024.42+00.04	Calibration_ pvparall_ 3	G158.86-20.77	KPGT_ pandre_ 1
G026.31+00.14	KPOT_ smolinar_ 1	G159.21-20.11	KPGT_ pandre_ 1
G026.54+00.62	KPGT_ mgroen01_ 1	G160.40-18.03	KPGT_ pandre_ 1
G032.91+00.14	KPOT_ smolinar_ 1	G162.07-08.79	OT1_ pharve01_ 3
G034.87-01.05	KPGT_ fmotte_ 1	G171.49-14.91	OT1_ mdunham_ 1
G035.09+00.13	KPOT_ smolinar_ 1	G171.50-14.91	OT1_ jpatienc_ 1
G037.91+02.17	KPOT_ mjuvela_ 1	G173.16+02.36	OT2_ jstutzki_ 3
G039.60+01.87	KPOT_ mjuvela_ 1	G173.40-14.07	KPGT_ pandre_ 1
G069.71-01.70	KPOT_ mjuvela_ 1	G178.12-00.02	OT1_ smolinar_ 5
G070.22-01.50	KPOT_ mjuvela_ 1	G178.41-00.69	OT1_ rsahai_ 4
G074.71+01.07	OT2_ smolinar_ 7	G195.74-02.29	KPOT_ mjuvela_ 1
G082.74-01.99	KPOT_ mjuvela_ 1	G202.15+02.64	KPOT_ mjuvela_ 1
G087.08-04.08	KPOT_ mjuvela_ 1		

Table B.3: Observation IDs for Herschel PACS 160-μm maps.

SPIRE		
Filename	obs id	proposal
G006.04+36.73	1342203075	KPOT_ mjuvela_ 1
G010.20+02.39	1342216945	KPOT_ mjuvela_ 1
G013.90-00.51	1342192062	KPGT_ okrause_ 1
G014.32-00.64	1342241160	GT2_ pandre_ 5
G017.69-00.15	1342218995	KPOT_ smolinar_ 1
G023.22+00.01	1342192065	KPGT_ okrause_ 1
G023.31+00.05	1342192066	KPGT_ okrause_ 1
G023.48+00.11	1342192067	KPGT_ okrause_ 1
G035.19-01.75	1342244164	GT2_ pandre_ 5
G037.92+02.18	1342229180	KPOT_ mjuvela_ 1
G039.60+01.86	1342219633	KPOT_ mjuvela_ 1
G070.07-01.60	1342219987	KPOT_ mjuvela_ 1
G082.75-01.98	1342222137	KPOT_ mjuvela_ 1
G087.08-04.08	1342222116	KPOT_ mjuvela_ 1
G089.76-06.83	1342213455	KPOT_ mjuvela_ 1
G092.12+03.88	1342220862	KPOT_ mjuvela_ 1
G094.11-04.86	1342197305	KPGT_ pandre_ 1
G105.60+10.31	1342219970	KPOT_ mjuvela_ 1
G109.79+02.70	1342187655	SDP_ mjuvela_ 3
G139.48-03.27	1342226625	KPOT_ mjuvela_ 1
G158.55-20.92	1342190326	KPGT_ pandre_ 1
G178.31+00.28	1342250769	OT1_ smolinar_ 5
G195.73-02.29	1342216931	KPOT_ mjuvela_ 1
G202.16+02.64	1342228342	KPOT_ mjuvela_ 1

Table B.4: Observation IDs for Herschel SPIRE 250-, 350-, and 500-μm maps. As SPIRE fields of the same coordinates were observed simultaneously, each wavelength range has the same observation ID.

B.2 Centers of the SCUBA-2 fields and reference regions

SCUBA field	Center of SCUBA fields		Centers of reference regions	
	RA[hms]	DEC[hms]	RA[hms]	DEC[hms]
G001.36+20.96	16:34:29.951	-15:47:12.665		
G005.93-01.00	18:2:55.703	-24:19:48.037		
G006.01+36.74	15:54:8.163	-2:52:35.496	15:53:49.215	-2:48:00.59
G010.21+02.40	17:59:19.479	-18:55:32.700	17:59:07.020	-18:50:49.16
G014.14-00.55	18:18:12.055	-16:55:16.957		
G014.15-00.55	18:18:12.553	-16:54:40.859	18:17:55.548	-16:55:25.31
G014.22-00.19	18:17:0.872	-16:40:29.967		
G014.72-00.19	18:17:59.847	-16:14:11.037		
G014.73-00.19	18:18:0.819	-16:13:51.071		
G016.28-00.45	18:22:0.411	-14:59:23.850	18:22:20.739	-15:04:23.81
G016.37-00.61	18:22:46.673	-14:59:10.549	18:22:50.147	-15:04:16.76
G016.43-00.62	18:22:56.411	-14:56:12.351	18:23:15.470	-15:00:54.14
G016.97+00.28	18:20:42.622	-14:2:1.078	18:20:56.296	-13:57:13.36
G017.23-01.47	18:27:33.538	-14:37:30.259		
G017.38+02.26	18:14:19.191	-12:43:50.711		

Table B.5: (*Columns 2/3*) Right ascension and declination of the center of the SCUBA-2 maps used for cropping. (*Columns 4/5*) Right ascension and declination for the centers of empty reference regions used for background removal; only sources with PACS 160-μm and SPIRE fields are listed. Table 1/3.

SCUBA field	Center of SCUBA fields		Centers of reference regions	
	RA[hms]	DEC[hms]	RA[hms]	DEC[hms]
G023.35-00.26	18:34:45.537	-8:38:18.739		
G023.68+00.58	18:32:22.659	-7:57:27.448		
G023.69+00.58	18:32:24.170	-7:56:49.453		
G024.04+00.27	18:34:9.879	-7:46:53.852		
G026.54+00.72	18:37:10.102	-5:21:22.284		
G033.73-00.01	18:52:56.664	0:42:19.969		
G034.74-01.39	18:59:41.331	0:58:34.566		
G035.38-01.77	19:2:11.354	1:22:17.762	19:02:07.578	+1:27:05.15
G035.50-00.31	18:57:14.578	2:8:46.655		
G037.93+02.18	18:52:46.738	5:26:15.119	18:52:29.633	+5:21:30.74
G039.74+01.98	18:56:48.006	6:57:44.196	18:56:28.628	+6:55:29.19
G057.12+03.63	19:23:58.152	23:7:51.001		
G069.81-01.67	20:13:34.414	31:21:54.388	20:13:55.682	+31:20:09.70
G070.40-01.40	20:14:3.026	32:0:55.778	20:13:46.779	+32:05:44.28
G074.13+00.11	20:18:0.979	35:57:18.402		
G082.40-01.84	20:51:25.863	41:24:21.475	20:51:19.270	+41:21:13.66
G082.42-01.84	20:51:29.663	41:25:29.675	20:51:19.143	+41:21:23.75
G087.07-04.20	21:17:47.194	43:18:36.614	21:18:04.811	+43:22:14.49

Table B.6: (*Columns 2/3*) Right ascension and declination of the center of the SCUBA-2 maps used for cropping. (*Columns 4/5*) Right ascension and declination for the centers of empty reference regions used for background removal; only sources with PACS 160-μm and SPIRE fields are listed. Table 2/3.

SCUBA field	Center of SCUBA fields		Centers of reference regions	
	RA[hms]	DEC[hms]	RA[hms]	DEC[hms]
G089.66-06.62	21:37:15.047	43:21:27.382	21:36:49.046	+43:17:09.34
G091.88+04.17	21:0:30.140	52:31:18.032		
G092.04+03.92	21:2:27.936	52:28:30.845	21:02:13.013	+52:33:18.56
G092.28+03.79	21:4:8.005	52:34:6.774	21:03:54.549	+52:38:55.89
G093.51-04.31	21:44:56.654	47:37:26.535	21:45:24.802	+47:42:09.68
G105.44+09.88	21:43:15.843	66:7:49.862		
G107.18+05.44	22:21:30.197	63:37:31.941		
G107.26+05.71	22:20:49.553	63:54:10.571		
G109.70+02.52	22:53:29.862	62:19:33.037	22:52:49.914	+62:18:32.07
G109.81+02.72	22:53:33.900	62:32:45.725	22:53:21.713	+62:37:29.72
G139.14-03.23	2:50:27.971	55:50:57.937	2:50:45.936	+55:55:45.49
G159.23-20.09	3:33:27.056	31:7:38.954	3:33:49.603	+31:08:17.64
G162.46-08.69	4:21:33.193	37:34:1.542		
G171.53-14.91	4:28:43.042	26:49:56.493		
G172.89+02.28	5:36:56.344	36:10:37.069		
G173.15+02.40	5:38:7.999	36:1:8.385		
G178.28-00.60	5:39:8.184	30:4:52.547	5:39:06.623	+30:09:41.50
G195.73-02.28	6:11:0.260	14:10:16.667	6:11:17.531	+14:06:52.24
G202.31+02.53	6:41:1.186	10:36:8.610	6:41:20.621	+10:38:22.39
G215.87-17.50	5:53:39.862	-10:24:3.859		

Table B.7: (*Columns 2/3*) Right ascension and declination of the center of the SCUBA-2 maps used for cropping. (*Columns 4/5*) Right ascension and declination for the centers of empty reference regions used for background removal; only sources with PACS 160-μm and SPIRE fields are listed. Table 3/3.

B.3 Herschel SPIRE instrument specifications

SPIRE

Band	**PSW**	**PMW**	**PLW**
Central wavelength (μm)	250	350	500
Spectral resolution ($\lambda/\Delta\lambda$)	3.3	3.4	2.5
Beam FWHM size (arcsec)	17.9	24.2	35.4
Number of detectors	139	88	43

PACS

Band	**Blue**	**Green**	**Red**
Central wavelength (μm)	70	100	160
Spectral resolution ($\lambda/\Delta\lambda$)	6.6	5.9	5.3
Beam FWHM size (arcsec)	5.6	6.8	varies

Table B.8: Characteristics of the SPIRE bands [63] (*top*) and of the PACS bands (*bottom*). The FWHM size for the red band depends on scan speed and is presented in Table B.9. Source: `https://www.cosmos.esa.int/documents/12133/996891/PACS+Photometer+Quick+Start+Guide`

Scan speed (arcsec/s)	FWHM (arcsec)	FWHM used in code
10	10.46 x 12.06	-
20	10.65 x 12.13	11.4
60	11.31 x 13.32	12.5
60 (parallel mode)	11.64 x 15.65	-

Table B.9: Speed and FWHM resolution of PACS 160-μm maps, as well as the FWHM values used for the code in Sect. 3.1.

B.4 Convolution kernels

Convolving to 500 μm (FWHM = 35.4")			
λ [μm]	original pixel size [arcsec]	original FWHM [arcsec]	σ arcsec
160 (medium)	3.2	11.4	2.486256
160 (fast)	3.2	12.5	2.456987
250	6.0	17.9	2.495991
350	10.0	24.2	0.981340
850	4.0	14.6	1.711863
Convolving to 350 μm (FWHM = 24.2")			
λ [μm]	original pixel size [arcsec]	original FWHM [arcsec]	σ arcsec
160 (medium)	3.2	11.4	1.583607
160 (fast)	3.2	12.5	1.537246
250	6.0	17.9	0.470573
850	4.0	14.6	1.024481
Convolving to 250 μm (FWHM = 17.9")			
λ [μm]	original pixel size [arcsec]	original FWHM [arcsec]	σ arcsec
160 (medium)	3.2	11.4	1.023783
160 (fast)	3.2	12.5	0.950498
850	4.0	14.6	0.549732

Table B.10: Pixel sizes, FWHM and σ of the kernel used for the convolution.

B.5 Distances to sources

The distances to the sources found in [45] (*column 2*), [41] (*column 3*), and estimated from CO data from [55] using Bayesian distance estimates from [54] (*column 4*). Fields missing from the tables do not have distance estimates. Error in [41] are assumed to be ± 30% (section 4.8).

SCUBA-2 field	Distance [kpc]		
	(GCCIV)	GCC catalog	CO-line data
G006.01+36.74	0.110 ± 0.010	-	-
G010.21+02.40	0.830 ± 0.400	-	-
G024.04+00.27	-	4.460	-
G026.54+00.72	-	4.220	-
G033.73-00.01	-	4.220	-
G034.74-01.39	-	4.220	-
G035.38-01.77	-	4.220	-
G035.50-00.31	-	4.220	-
G037.93+02.18	1.060 ± 0.790	1.060	-
G039.74+01.98	0.990 ± 0.480	-	-
G069.81-01.67	1.780 ± 0.810	-	-
G070.40-01.40	2.090 ± 0.830	-	-
G082.40-01.84	$1.000^{+1.000}_{-0.600}$	-	-
G082.42-01.84	$1.000^{+1.000}_{-0.600}$	-	-
G087.07-04.20	0.700 ± 0.100	-	-
G089.66-06.62	1.210 ± 1.210	-	-

Table B.11: Distances estimates to the sources from [45] (*column 2*) and from GCC catalogs [41] (*column 3*) in kpc, and estimated distances from CO line data from [55] (*column 4*), with associated SCUBA-2 fields. Table 1/2

SCUBA-2 field	Distance [kpc]		
	(GCCIV)	GCC catalog	CO-line data
G092.04+03.92	0.800 ± 0.100	-	-
G092.28+03.79	0.800 ± 0.100	-	-
G105.44+09.88	-	-	0.89 ± 0.07
G107.18+05.44	0.800 ± 0.100	0.900	-
G107.26+05.71	0.800 ± 0.100	0.900	-
G109.70+02.52	0.800 ± 0.100	-	-
G109.81+02.72	0.800 ± 0.100	0.700	-
G139.14-03.23	2.500 ± 0.500	-	-
G159.23-20.09	-	-	0.37 ± 0.11
G162.46-08.69	0.450 ± 0.023	-	-
G173.15+02.40	2.000 ± 0.400	-	-
G195.73-02.28	1.000 ± 0.500	-	-
G202.31+02.53	0.760 ± 0.100	-	2.285 ± 0.67*
G215.87-17.50	0.425 ± 0.100	-	-

Table B.12: Distances estimated to the sources in [45] (*column 2*) and from GCC catalogs [41] (*column 3*)in kpc, and estimated distances from CO line data from [55] (*column 4*), with associated SCUBA-2 fields. *The GCCIV [45] distance estimate is used for field G202 due to uncertainties in the Bayesian estimate, see section 3.2. Table 2/2

B.5.1 Input values for the Bayesian Distance Calculator

Name	ℓ	b	v_{LSR}		Distance estimate	
			^{12}CO	^{13}CO	^{12}CO	^{13}CO
	(deg)	(deg)	(km/s)	(km/s)	(kpc)	
G105	105.415	9.87943	-10.475	-10.2	0.89 ± 0.07	
G159	159.23	-20.1098	7.350	6.675	0.37 ± 0.11	
G202	202.306	2.5335	7.8	7.4	2.29 ± 0.47	2.28 ± 0.48

Table B.13: Input values and results for the Bayesian distance calculator. Galactic latitude (b) and longitude (ℓ) are from the source's name. Velocities have been found from CO line data and are in km/s. Distance estimates come from the calculator. For field G202, the calculator's distance estimate has very large uncertainty and the distance from [45] has been used instead.

B.6 Parameters of the `FellWalker` clump detection algorithm

RMS	MinHeight	AllowEdge	MinPix	CleanIter	Noise	FWHMBeam	MaxJump	deconv	MinDip
Varies	3×RMS	0	7	5	1×RMS	1	3	True	1.5×RMS

Table B.14: Input values used for FellWalker algorithm for SCUBA-2 sources. See section 3.3.1 for details on RMS values. FlatSlope, VeloRes, and MaxBad values were left to their default values.

B.7 Matches between YSO catalogs

	Simbad	Akari PSC	Marton III	Akari BSC	PACS 70	PACS 100
Total:	506	174	2	125	84	46
Simbad	6	46	-	3	18	14
Akari PSC	46	X	2	2	17	7
Marton III	-	2	X	-	-	-
Akari BSC	3	2	-	X	2	2
PACS 70	18	17	-	2	X	15
PACS 100	14	7	-	2	15	X

Table B.15: Number of matching sources between the YSO catalogs. The table includes only clump-associated YSOs. Total number of YSOs in each catalog is included in the second row.

	Simbad	Akari PSC	Marton III	Akari BSC	PACS 70	PACS 100
Total:	1041	373	8	309	84	46
Simbad	7	68	-	5	18	14
Akari PSC	68	X	3	4	17	7
Marton III	-	3	X	-	-	-
Akari BSC	5	4	-	X	2	2
PACS 70	18	17	-	2	X	15
PACS 100	14	7	-	2	15	X

Table B.16: Number of matching sources between the YSO catalogs. The table includes YSOs not associated with any clumps.

B.8 Results of virial analysis

G105

Clump ID	ΔV (km/s)	R_{eff} (pc)	T (K)	M ($M_\odot$)	M_{vir} ($M_\odot$)	α_{vir}	α_{BE}
2	1.95	0.106	20.71	53.1	24.8	0.47	0.08
3	2.57	0.082	21.27	12.3	32.1	2.61	0.28
4	1.45	0.096	16.26	20.0	12.89	0.64	0.15
5	1.1	0.066	14.54	9.3	5.45	0.59	0.2

G159

Clump ID	ΔV (km/s)	R_{eff} (pc)	T (K)	M ($M_\odot$)	M_{vir} ($M_\odot$)	α_{vir}	α_{BE}
2*	2.08	0.04	11.39	23.9	10.15	0.42	0.04
4*	2.06	0.02	12.33	2.4	5.0	2.08	0.2
5	2.1	0.023	12.99	1.3	5.98	4.6	0.47
6	2.03	0.036	11.96	3.5	8.74	2.5	0.24

G202

Clump ID	ΔV (km/s)	R_{eff} (pc)	T (K)	M ($M_\odot$)	M_{vir} ($M_\odot$)	α_{vir}	α_{BE}
1*	2.71	0.046	16.05	22.6	19.67	0.87	0.06
2*	2.29	0.041	14.54	13.2	12.65	0.96	0.09
3*	2.13	0.093	12.71	33.4	24.83	0.74	0.07
6*	1.57	0.069	13.09	14.4	10.44	0.73	0.12
7*	2.16	0.064	12.32	10.6	17.52	1.65	0.15

Table B.17: Calculated virial masses M_{vir}, α values, and input values for appropriate clumps in the three fields with CO data. Clumps marked with an asterisk (*) have a detection in either 70 or 100 μm from the PACS point source catalog.

B.9 Clump characteristics

The tables B.18-B.38 list the physical characteristics of the extracted clumps. The uncertainties are discussed in Sect. 4.8 and summarized below.

	coordinates	R_{eff}	F_ν	T	I_{250}	$N(\mathrm{H_2})$	M	M_{BE}	α_{BE}	N_*
error [%]	0	30	10	10	10	50	80	30	85	35

G001.36+20.96													
clump No.	RA (J2000)	dec (J2000)	pos. angle (°)	R_{eff} [pc]	F_ν (Jy)	T [K]	I_{250} [MJy/sr]	N(H_2) [10^{21}cm^{-2}]	M ($M_\odot$)	M_{BE} ($M_\odot$)	α_{BE}	N_*	type
1	-111.3746	-15.78281	264.0	-	1.909	-	-	-	-	-	-	2	ps
2	-111.3479	-15.78574	310.0	-	5.833	-	-	-	-	-	-	0	-
3	-111.3657	-15.77261	308.0	-	1.171	-	-	-	-	-	-	0	-
4	-111.4617	-15.80433	256.0	-	0.102	-	-	-	-	-	-	1	ps
5	-111.3914	-15.78631	195.0	-	0.706	-	-	-	-	-	-	0	-

G005.93-01.00													
clump No.	RA (J2000)	dec (J2000)	pos. angle (°)	R_{eff} [pc]	F_ν (Jy)	T [K]	I_{250} [MJy/sr]	N(H_2) [10^{21}cm^{-2}]	M ($M_\odot$)	M_{BE} ($M_\odot$)	α_{BE}	N_*	type
1	-89.32781	-24.31859	186.0	-	4.465	-	-	-	-	-	-	1	ps
2	-89.28649	-24.37962	323.0	-	7.785	-	-	-	-	-	-	2	ps
3	-89.28506	-24.33738	273.0	-	10.492	-	-	-	-	-	-	4	ps
4	-89.2608	-24.35461	313.0	-	5.546	-	-	-	-	-	-	2	ps
5	-89.27913	-24.36339	315.0	-	6.427	-	-	-	-	-	-	0	-
6	-89.3454	-24.33135	348.0	-	1.309	-	-	-	-	-	-	0	-
7	-89.31667	-24.39088	209.0	-	1.894	-	-	-	-	-	-	1	ps
8	-89.30579	-24.37866	335.0	-	2.281	-	-	-	-	-	-	0	-
9	-89.35441	-24.31664	263.0	-	1.46	-	-	-	-	-	-	0	-
10	-89.35394	-24.3505	186.0	-	3.597	-	-	-	-	-	-	2	ps
11	-89.30409	-24.39851	315.0	-	0.861	-	-	-	-	-	-	0	-
12	-89.30378	-24.31645	289.0	-	0.641	-	-	-	-	-	-	0	-
13	-89.22086	-24.35775	358.0	-	0.247	-	-	-	-	-	-	1	ps
14	-89.22096	-24.3437	261.0	-	0.604	-	-	-	-	-	-	1	ps
15	-89.2264	-24.28342	272.0	-	0.26	-	-	-	-	-	-	1	ps
16	-89.203	-24.34	317.0	-	0.381	-	-	-	-	-	-	0	-
17	-89.27018	-24.29276	308.0	-	0.267	-	-	-	-	-	-	0	-

Table B.18: $N(H_2)$, T, and I_{250} are derived for fields with matching Herschel data and mass estimates for fields with distance estimates.

G006.01+36.74													
clump No.	RA (J2000)	dec (J2000)	pos. angle (°)	R_{eff} [pc]	F_ν (Jy)	T [K]	I_{250} [MJy/sr]	N(H_2) [10^{21}cm^{-2}]	M ($M_\odot$)	M_{BE} ($M_\odot$)	α_{BE}	N_*	type
1	-121.4644	-2.872602	354.0	0.013	3.561	10.6	171.0	23.47	0.82	0.3	0.33	0	pre
2	-121.4593	-2.813538	251.0	0.008	0.47	10.9	188.4	21.69	0.1	0.2	1.68	0	pre
3	-121.4982	-2.873737	336.0	0.006	0.195	11.21	149.3	14.7	0.04	0.1	3.31	0	sl

G010.21+02.40													
clump No.	RA (J2000)	dec (J2000)	pos. angle (°)	R_{eff} [pc]	F_ν (Jy)	T [K]	I_{250} [MJy/sr]	N(H_2) [10^{21}cm^{-2}]	M ($M_\odot$)	M_{BE} ($M_\odot$)	α_{BE}	N_*	type
1	-90.19283	-18.95029	213.0	0.122	3.679	15.71	572.9	12.86	23.69	3.8	0.16	2	ps
2	-90.10765	-18.8847	350.0	0.035	0.373	16.07	374.6	7.59	2.31	1.1	0.48	1	ps
3	-90.16625	-18.96469	224.0	0.028	0.307	15.63	334.3	7.56	2.0	0.9	0.43	1	ps
4	-90.09011	-18.92375	283.0	0.016	0.153	17.74	407.7	5.87	0.81	0.6	0.69	1	ps
5	-90.10893	-18.89805	203.0	0.044	0.367	16.0	406.9	8.47	2.29	1.4	0.61	0	pre
6	-90.21107	-18.95283	286.0	0.041	0.331	15.52	394.1	9.27	2.17	1.3	0.58	0	pre
7	-90.1585	-18.91989	301.0	0.037	0.212	16.82	419.1	7.32	1.22	1.2	1.0	2	ps
8	-90.15228	-18.87332	316.0	0.019	0.11	16.39	331.7	6.33	0.66	0.6	0.93	1	ps
9	-90.14558	-18.94956	355.0	0.03	0.167	16.74	379.3	6.69	0.97	1.0	1.02	1	ps
10	-90.11171	-18.90999	328.0	0.019	0.087	16.28	429.2	8.34	0.53	0.6	1.16	0	pre

G014.14-00.55													
clump No.	RA (J2000)	dec (J2000)	pos. angle (°)	R_{eff} [pc]	F_ν (Jy)	T [K]	I_{250} [MJy/sr]	N(H_2) [10^{21}cm^{-2}]	M ($M_\odot$)	M_{BE} ($M_\odot$)	α_{BE}	N_*	type
1	-85.44873	-16.95285	251.0	-	36.462	-	-	-	-	-	-	25	ps
2	-85.4488	-16.8383	201.0	-	11.238	-	-	-	-	-	-	6	ps
3	-85.45413	-16.87665	189.0	-	6.599	-	-	-	-	-	-	12	ps
4	-85.47984	-16.97026	282.0	-	3.58	-	-	-	-	-	-	6	ps
5	-85.47113	-16.85636	244.0	-	9.542	-	-	-	-	-	-	10	ps
6	-85.47987	-16.98663	222.0	-	8.915	-	-	-	-	-	-	4	ps
7	-85.47172	-16.96453	346.0	-	2.221	-	-	-	-	-	-	1	ps
8	-85.45228	-16.85928	202.0	-	2.885	-	-	-	-	-	-	4	ps
9	-85.46026	-16.84166	190.0	-	1.803	-	-	-	-	-	-	0	-
10	-85.48774	-16.92	197.0	-	5.746	-	-	-	-	-	-	6	ps

Table B.19: $N(H_2)$, T, and I_{250} are derived for fields with matching Herschel data and mass estimates for fields with distance estimates.

G014.14-00.55, con't													
clump No.	RA (J2000)	dec (J2000)	pos. angle (°)	R_{eff} [pc]	F_ν (Jy)	T [K]	I_{250} [MJy/sr]	N(H_2) [10^{21}cm^{-2}]	M ($M_\odot$)	M_{BE} ($M_\odot$)	α_{BE}	N_*	type
11	-85.43682	-16.91151	343.0	-	4.674	-	-	-	-	-	-	7	ps
12	-85.48061	-16.87454	221.0	-	4.311	-	-	-	-	-	-	4	ps
13	-85.47853	-16.8942	313.0	-	1.118	-	-	-	-	-	-	4	ps
14	-85.47991	-16.90351	318.0	-	1.495	-	-	-	-	-	-	3	ps
15	-85.44818	-16.9194	262.0	-	2.48	-	-	-	-	-	-	1	ps
16	-85.4182	-16.93131	264.0	-	1.611	-	-	-	-	-	-	0	-
17	-85.41971	-16.91859	228.0	-	4.1	-	-	-	-	-	-	2	ps
18	-85.39679	-16.90198	224.0	-	2.445	-	-	-	-	-	-	2	ps
19	-85.38534	-16.92341	244.0	-	1.975	-	-	-	-	-	-	9	ps
20	-85.49035	-16.89654	186.0	-	2.207	-	-	-	-	-	-	7	ps
21	-85.46041	-16.93738	241.0	-	2.304	-	-	-	-	-	-	5	ps
22	-85.39625	-16.93768	357.0	-	2.133	-	-	-	-	-	-	5	ps
23	-85.41012	-16.94108	217.0	-	3.551	-	-	-	-	-	-	2	ps
24	-85.45903	-16.90357	338.0	-	3.579	-	-	-	-	-	-	1	ps
25	-85.3781	-16.88304	211.0	-	2.16	-	-	-	-	-	-	4	ps
26	-85.49578	-16.96075	236.0	-	1.06	-	-	-	-	-	-	0	-
27	-85.43311	-16.84664	300.0	-	0.693	-	-	-	-	-	-	2	ps
28	-85.50571	-16.94503	187.0	-	2.284	-	-	-	-	-	-	1	ps
29	-85.4253	-16.86782	305.0	-	0.277	-	-	-	-	-	-	1	ps
30	-85.3966	-16.87667	230.0	-	0.504	-	-	-	-	-	-	0	-
31	-85.41024	-16.84734	182.0	-	0.313	-	-	-	-	-	-	1	ps
32	-85.52269	-16.96182	268.0	-	0.775	-	-	-	-	-	-	1	ps
33	-85.42219	-16.86044	203.0	-	0.094	-	-	-	-	-	-	0	-
34	-85.4139	-16.97546	271.0	-	0.707	-	-	-	-	-	-	4	ps
35	-85.42569	-17.00027	327.0	-	0.205	-	-	-	-	-	-	0	-

Table B.20: $N(H_2)$, T, and I_{250} are derived for fields with matching Herschel data and mass estimates for fields with distance estimates.

G014.15-00.55													
clump No.	RA (J2000)	dec (J2000)	pos. angle (°)	R_{eff} [pc]	F_ν (Jy)	T [K]	I_{250} [MJy/sr]	N(H_2) [10^{21}cm^{-2}]	M ($M_\odot$)	M_{BE} ($M_\odot$)	α_{BE}	N_*	type
1	-85.44842	-16.83207	190.0	-	26.816	-	-	-	-	-	-	14	ps
2	-85.44868	-16.95474	251.0	-	36.118	-	-	-	-	-	-	28	ps
3	-85.4544	-16.8787	192.0	-	5.972	-	-	-	-	-	-	13	ps
4	-85.47966	-16.97254	285.0	-	3.711	-	-	-	-	-	-	3	ps
5	-85.47836	-16.98495	266.0	-	6.161	-	-	-	-	-	-	3	ps
6	-85.46993	-16.85578	227.0	-	11.517	-	-	-	-	-	-	11	ps
7	-85.47326	-16.96555	314.0	-	2.53	-	-	-	-	-	-	1	ps
8	-85.45284	-16.86107	205.0	-	3.001	-	-	-	-	-	-	5	ps
9	-85.48782	-16.92099	197.0	-	5.822	-	-	-	-	-	-	5	ps
10	-85.47688	-16.8964	304.0	-	1.608	-	-	-	-	-	-	7	ps
11	-85.48185	-16.87616	347.0	-	4.0	-	-	-	-	-	-	3	ps
12	-85.49052	-16.89808	185.0	-	2.573	-	-	-	-	-	-	10	ps
13	-85.43723	-16.91366	327.0	-	3.877	-	-	-	-	-	-	6	ps
14	-85.48056	-16.90459	321.0	-	1.487	-	-	-	-	-	-	1	ps
15	-85.41821	-16.93255	210.0	-	1.405	-	-	-	-	-	-	1	ps
16	-85.44822	-16.9207	246.0	-	2.205	-	-	-	-	-	-	2	ps
17	-85.39619	-16.94129	193.0	-	1.515	-	-	-	-	-	-	3	ps
18	-85.38776	-16.92555	212.0	-	1.277	-	-	-	-	-	-	4	ps
19	-85.46101	-16.93953	243.0	-	2.172	-	-	-	-	-	-	3	ps
20	-85.42039	-16.92032	225.0	-	2.931	-	-	-	-	-	-	3	ps
21	-85.41044	-16.94269	218.0	-	3.083	-	-	-	-	-	-	2	ps
22	-85.39383	-16.90022	221.0	-	1.159	-	-	-	-	-	-	4	ps
23	-85.45832	-16.90622	348.0	-	2.998	-	-	-	-	-	-	1	ps
24	-85.37857	-16.88476	212.0	-	1.946	-	-	-	-	-	-	5	ps
25	-85.37937	-16.92461	313.0	-	0.51	-	-	-	-	-	-	1	ps
26	-85.43411	-16.84795	303.0	-	0.664	-	-	-	-	-	-	0	-
27	-85.49518	-16.96237	245.0	-	0.783	-	-	-	-	-	-	0	-
28	-85.50563	-16.94434	188.0	-	2.277	-	-	-	-	-	-	4	ps
29	-85.46721	-16.82366	247.0	-	0.096	-	-	-	-	-	-	0	-
30	-85.42143	-16.83186	182.0	-	0.23	-	-	-	-	-	-	0	-
31	-85.40164	-16.90995	294.0	-	0.43	-	-	-	-	-	-	0	-
32	-85.39635	-16.87743	240.0	-	0.429	-	-	-	-	-	-	1	ps

Table B.21: $N(H_2)$, T, and I_{250} are derived for fields with matching Herschel data and mass estimates for fields with distance estimates.

G014.22-00.19													
clump No.	RA (J2000)	dec (J2000)	pos. angle (°)	R_{eff} [pc]	F_ν (Jy)	T [K]	I_{250} [MJy/sr]	N(H_2) [10^{21}cm^{-2}]	M ($M_\odot$)	M_{BE} ($M_\odot$)	α_{BE}	N_*	type
1	-85.75632	-16.70842	235.0	-	17.823	-	-	-	-	-	-	4	ps
2	-85.75018	-16.6931	252.0	-	10.613	-	-	-	-	-	-	0	-
3	-85.73644	-16.70063	269.0	-	3.925	-	-	-	-	-	-	1	ps
4	-85.77504	-16.69557	220.0	-	6.567	-	-	-	-	-	-	0	-
5	-85.7255	-16.7317	302.0	-	7.92	-	-	-	-	-	-	1	ps
6	-85.73354	-16.71274	267.0	-	3.719	-	-	-	-	-	-	2	ps
7	-85.75045	-16.65904	220.0	-	7.139	-	-	-	-	-	-	2	ps
8	-85.76518	-16.65465	239.0	-	2.852	-	-	-	-	-	-	1	ps
9	-85.80301	-16.6616	180.0	-	4.403	-	-	-	-	-	-	1	ps
10	-85.7796	-16.67675	200.0	-	3.181	-	-	-	-	-	-	2	ps
11	-85.80349	-16.68917	298.0	-	6.776	-	-	-	-	-	-	1	ps
12	-85.8257	-16.65309	272.0	-	1.253	-	-	-	-	-	-	2	ps
13	-85.71651	-16.68478	209.0	-	2.384	-	-	-	-	-	-	1	ps
14	-85.71335	-16.61789	222.0	-	1.06	-	-	-	-	-	-	1	ps
15	-85.69569	-16.74028	184.0	-	0.287	-	-	-	-	-	-	2	ps
16	-85.75378	-16.59803	245.0	-	0.537	-	-	-	-	-	-	3	ps

G014.72-00.19													
clump No.	RA (J2000)	dec (J2000)	pos. angle (°)	R_{eff} [pc]	F_ν (Jy)	T [K]	I_{250} [MJy/sr]	N(H_2) [10^{21}cm^{-2}]	M ($M_\odot$)	M_{BE} ($M_\odot$)	α_{BE}	N_*	type
1	-85.5308	-16.22638	230.0	-	11.33	-	-	-	-	-	-	4	ps
2	-85.49551	-16.28702	259.0	-	15.031	-	-	-	-	-	-	2	ps
3	-85.48791	-16.22904	340.0	-	20.868	-	-	-	-	-	-	2	ps
4	-85.4696	-16.26493	268.0	-	5.159	-	-	-	-	-	-	2	ps
5	-85.48613	-16.18539	291.0	-	1.403	-	-	-	-	-	-	1	ps
6	-85.45499	-16.18472	356.0	-	2.574	-	-	-	-	-	-	2	ps
7	-85.46603	-16.1833	282.0	-	1.885	-	-	-	-	-	-	0	-
8	-85.56006	-16.2352	300.0	-	2.811	-	-	-	-	-	-	1	ps
9	-85.47046	-16.17127	297.0	-	1.099	-	-	-	-	-	-	1	ps
10	-85.45647	-16.23975	324.0	-	0.915	-	-	-	-	-	-	0	-
11	-85.5113	-16.31255	243.0	-	0.975	-	-	-	-	-	-	0	-

Table B.22: $N(H_2)$, T, and I_{250} are derived for fields with matching Herschel data and mass estimates for fields with distance estimates.

G014.73-00.19													
clump No.	RA (J2000)	dec (J2000)	pos. angle (°)	R_{eff} [pc]	F_ν (Jy)	T [K]	I_{250} [MJy/sr]	N(H_2) [10^{21}cm^{-2}]	M ($M_\odot$)	M_{BE} ($M_\odot$)	α_{BE}	N_*	type
1	-85.53097	-16.22693	224.0	-	10.854	-	-	-	-	-	-	4	ps
2	-85.48809	-16.28714	243.0	-	6.969	-	-	-	-	-	-	0	-
3	-85.49211	-16.23085	327.0	-	11.601	-	-	-	-	-	-	0	-
4	-85.48676	-16.18528	301.0	-	1.196	-	-	-	-	-	-	0	-
5	-85.47263	-16.26268	353.0	-	2.842	-	-	-	-	-	-	1	ps
6	-85.45602	-16.18415	359.0	-	1.364	-	-	-	-	-	-	1	ps
7	-85.46591	-16.18321	303.0	-	1.44	-	-	-	-	-	-	0	-
8	-85.55875	-16.23645	281.0	-	2.188	-	-	-	-	-	-	1	ps
9	-85.46743	-16.17311	264.0	-	0.633	-	-	-	-	-	-	0	-
10	-85.4564	-16.23951	353.0	-	0.32	-	-	-	-	-	-	1	ps
11	-85.49226	-16.1995	305.0	-	2.014	-	-	-	-	-	-	0	-
12	-85.45725	-16.16776	322.0	-	0.386	-	-	-	-	-	-	0	-
13	-85.47889	-16.16602	333.0	-	0.216	-	-	-	-	-	-	0	-
14	-85.53582	-16.29529	246.0	-	1.464	-	-	-	-	-	-	0	-

G016.28-00.45													
clump No.	RA (J2000)	dec (J2000)	pos. angle (°)	R_{eff} [pc]	F_ν (Jy)	T [K]	I_{250} [MJy/sr]	N(H_2) [10^{21}cm^{-2}]	M ($M_\odot$)	M_{BE} ($M_\odot$)	α_{BE}	N_*	type
1	-84.42012	-15.00251	306.0	-	6.213	19.42	2735.8	-	-	-	-	1	ps
2	-84.4572	-14.97075	246.0	-	2.116	21.86	2480.6	-	-	-	-	3	ps
3	-84.46495	-14.94146	193.0	-	2.007	21.55	2472.1	-	-	-	-	3	ps
4	-84.56057	-14.92951	191.0	-	1.456	20.47	2237.3	-	-	-	-	2	ps
5	-84.44987	-14.98638	274.0	-	2.236	21.2	2312.5	-	-	-	-	1	ps
6	-84.43992	-15.00559	211.0	-	0.333	21.01	2223.8	-	-	-	-	0	-
7	-84.4503	-14.92265	344.0	-	0.837	21.21	2382.1	-	-	-	-	0	-
8	-84.44785	-14.9402	356.0	-	0.842	20.62	2362.8	-	-	-	-	0	-
9	-84.42716	-14.93879	340.0	-	0.173	22.56	2132.8	-	-	-	-	0	-
10	-84.47216	-15.04437	269.0	-	0.179	21.56	1894.9	-	-	-	-	0	-

Table B.23: $N(H_2)$, T, and I_{250} are derived for fields with matching Herschel data and mass estimates for fields with distance estimates.

G016.37-00.61													
clump No.	RA (J2000)	dec (J2000)	pos. angle (°)	R_{eff} [pc]	F_ν (Jy)	T [K]	I_{250} [MJy/sr]	$N(H_2)$ [10^{21}cm^{-2}]	M ($M_\odot$)	M_{BE} ($M_\odot$)	α_{BE}	N_*	type
1	-84.34565	-15.0001	288.0	-	6.061	18.92	2706.1	32.02	-	-	-	1	ps
2	-84.37895	-14.99672	291.0	-	2.836	18.79	2554.8	30.56	-	-	-	1	ps
3	-84.26437	-14.95359	227.0	-	9.648	18.13	2017.7	28.5	-	-	-	1	ps
4	-84.29311	-14.97459	247.0	-	6.263	18.99	2141.6	25.3	-	-	-	2	ps
5	-84.38044	-15.01289	274.0	-	2.996	19.46	2573.6	27.78	-	-	-	2	ps
6	-84.23675	-14.96312	226.0	-	3.996	17.89	1804.6	25.63	-	-	-	1	ps
7	-84.32193	-14.98129	235.0	-	2.513	19.44	2114.7	22.76	-	-	-	0	-
8	-84.32775	-14.99906	202.0	-	1.963	19.39	2435.5	26.33	-	-	-	0	-
9	-84.30299	-14.95537	269.0	-	0.751	20.2	2017.4	19.27	-	-	-	0	-
10	-84.34622	-14.97916	245.0	-	3.022	20.47	2236.1	20.52	-	-	-	0	-
11	-84.29488	-14.95949	237.0	-	0.947	19.35	2295.0	24.88	-	-	-	0	-
12	-84.37024	-14.9842	346.0	-	1.479	20.34	2389.7	22.5	-	-	-	0	-
13	-84.30939	-14.9962	194.0	-	2.67	20.28	1938.5	18.52	-	-	-	1	ps
14	-84.35673	-15.01297	261.0	-	1.097	20.18	2215.7	21.23	-	-	-	0	-
15	-84.24492	-14.93741	195.0	-	0.465	17.97	1758.8	24.39	-	-	-	0	-
16	-84.22364	-14.97196	230.0	-	0.24	18.1	1634.7	22.0	-	-	-	1	ps
17	-84.23228	-15.00047	341.0	-	0.379	20.74	1410.7	12.41	-	-	-	1	ps
18	-84.23318	-14.97908	299.0	-	0.195	19.85	1534.9	15.48	-	-	-	0	-
19	-84.26994	-15.06393	261.0	-	0.145	20.29	1419.8	13.45	-	-	-	1	ps
20	-84.26284	-14.92042	273.0	-	0.222	20.49	1863.7	16.97	-	-	-	0	-
21	-84.30821	-14.93752	267.0	-	0.313	21.3	1883.0	15.31	-	-	-	0	-
22	-84.32812	-15.063	259.0	-	0.965	20.95	1684.1	14.4	-	-	-	4	ps
23	-84.25603	-14.99528	289.0	-	0.225	21.38	1445.6	11.63	-	-	-	0	-
24	-84.35667	-15.04514	309.0	-	1.089	21.53	1903.4	15.01	-	-	-	1	ps
25	-84.36336	-15.02871	276.0	-	0.25	20.77	1999.0	17.5	-	-	-	0	-
26	-84.26096	-15.03915	325.0	-	0.067	20.57	1348.2	12.15	-	-	-	1	ps
27	-84.33046	-14.94655	315.0	-	0.256	21.21	1881.8	15.55	-	-	-	0	-
28	-84.25992	-15.05482	293.0	-	0.062	19.55	1393.3	14.62	-	-	-	0	-

Table B.24: $N(H_2)$, T, and I_{250} are derived for fields with matching Herschel data and mass estimates for fields with distance estimates.

G016.43-00.62													
clump No.	RA (J2000)	dec (J2000)	pos. angle (°)	R_{eff} [pc]	F_ν (Jy)	T [K]	I_{250} [MJy/sr]	N(H_2) [10^{21}cm^{-2}]	M ($M_\odot$)	M_{BE} ($M_\odot$)	α_{BE}	N_*	type
1	-84.2108	-14.9329	194.0	-	3.815	18.69	1836.3	13.67	-	-	-	4	ps
2	-84.25667	-14.94527	191.0	-	5.628	18.03	1880.1	21.54	-	-	-	0	-
3	-84.27203	-14.95852	318.0	-	6.251	19.11	2054.6	19.8	-	-	-	0	-
4	-84.22201	-14.9538	230.0	-	1.761	17.8	1713.3	10.47	-	-	-	1	ps
5	-84.29367	-14.97439	245.0	-	5.736	19.19	2084.9	15.36	-	-	-	1	ps
6	-84.21987	-14.8899	286.0	-	0.972	18.62	1627.0	30.06	-	-	-	1	ps
7	-84.22452	-14.89582	302.0	-	1.017	20.52	1580.4	17.68	-	-	-	0	-
8	-84.22909	-14.90684	264.0	-	2.737	19.15	1705.4	30.51	-	-	-	1	ps
9	-84.23757	-14.96178	219.0	-	4.611	18.18	1792.5	9.89	-	-	-	2	ps
10	-84.23305	-14.93233	249.0	-	2.554	18.3	1770.3	17.79	-	-	-	1	ps
11	-84.29895	-14.95712	286.0	-	2.057	20.14	2152.4	31.74	-	-	-	0	-
12	-84.32277	-14.98241	221.0	-	2.894	19.29	2333.1	-	-	-	-	1	ps
13	-84.21499	-14.88109	260.0	-	1.511	19.95	1627.2	18.31	-	-	-	0	-
14	-84.21588	-14.97876	328.0	-	3.095	19.6	1374.2	-	-	-	-	2	ps
15	-84.30809	-14.99357	343.0	-	1.812	19.58	2124.2	-	-	-	-	1	ps
16	-84.33775	-14.97509	225.0	-	1.479	20.5	2181.6	-	-	-	-	1	ps
17	-84.26351	-14.91665	347.0	-	0.973	21.39	1706.1	21.5	-	-	-	0	-
18	-84.31379	-15.00643	307.0	-	0.611	20.7	1933.2	-	-	-	-	0	-
19	-84.23181	-14.85647	282.0	-	0.556	20.54	1641.9	12.91	-	-	-	1	ps
20	-84.23201	-15.00261	328.0	-	0.413	20.92	1408.2	-	-	-	-	1	ps
21	-84.195	-14.90006	273.0	-	0.505	19.89	1381.3	26.55	-	-	-	0	-
22	-84.30386	-14.93828	268.0	-	0.819	21.37	1806.5	26.51	-	-	-	0	-
23	-84.23272	-14.97948	308.0	-	0.212	20.09	1488.5	10.69	-	-	-	0	-
24	-84.23463	-14.99214	221.0	-	0.158	20.84	1427.7	-	-	-	-	0	-
25	-84.25514	-14.99496	286.0	-	0.293	21.63	1429.9	-	-	-	-	0	-
26	-84.33096	-14.94564	260.0	-	0.207	21.19	1893.1	-	-	-	-	0	-
27	-84.28281	-14.90997	306.0	-	0.083	21.61	1651.2	16.44	-	-	-	0	-

Table B.25: $N(H_2)$, T, and I_{250} are derived for fields with matching Herschel data and mass estimates for fields with distance estimates.

G016.97+00.28													
clump No.	RA (J2000)	dec (J2000)	pos. angle (°)	R_{eff} [pc]	F_ν (Jy)	T [K]	I_{250} [MJy/sr]	N(H_2) [10^{21}cm^{-2}]	M ($M_\odot$)	M_{BE} ($M_\odot$)	α_{BE}	N_*	type
1	-84.78888	-14.09805	296.0	-	4.221	20.61	1769.4	16.08	-	-	-	3	ps
2	-84.81567	-14.09118	275.0	-	5.546	19.78	1926.6	19.79	-	-	-	1	ps
3	-84.8326	-14.08136	283.0	-	4.647	20.15	2013.3	19.31	-	-	-	2	ps
4	-84.85474	-14.06896	273.0	-	4.939	21.02	1835.2	15.49	-	-	-	5	ps
5	-84.80599	-14.10831	289.0	-	6.793	20.44	1914.1	17.85	-	-	-	0	-
6	-84.8918	-14.0645	300.0	-	4.476	20.39	1789.5	16.65	-	-	-	1	ps
7	-84.84584	-13.95482	298.0	-	0.961	18.75	1217.9	14.67	-	-	-	1	ps
8	-84.79202	-13.97028	291.0	-	0.529	19.1	1208.7	13.73	-	-	-	0	-
9	-84.84609	-14.02385	186.0	-	3.013	21.63	1394.8	10.83	-	-	-	2	ps
10	-84.80057	-13.98859	200.0	-	0.459	19.27	1328.8	14.62	-	-	-	2	ps
11	-84.82041	-14.01498	232.0	-	0.565	20.17	1500.5	14.34	-	-	-	0	-
12	-84.81872	-13.96428	335.0	-	0.481	19.03	1177.3	13.47	-	-	-	1	ps
13	-84.81328	-14.04207	324.0	-	0.637	20.48	1396.7	12.73	-	-	-	0	-
14	-84.80824	-14.06021	280.0	-	0.117	20.62	1362.6	12.17	-	-	-	0	-

G017.23-01.47													
clump No.	RA (J2000)	dec (J2000)	pos. angle (°)	R_{eff} [pc]	F_ν (Jy)	T [K]	I_{250} [MJy/sr]	N(H_2) [10^{21}cm^{-2}]	M ($M_\odot$)	M_{BE} ($M_\odot$)	α_{BE}	N_*	type
1	-83.12272	-14.62966	318.0	-	4.296	9.76	436.8	8.78	-	-	-	0	-
2	-83.12043	-14.64824	195.0	-	3.402	-0.01	-0.6	-0.0208	-	-	-	0	-
3	-83.09321	-14.57794	296.0	-	0.786	13.3	481.9	8.15	-	-	-	2	ps
4	-83.10682	-14.61649	358.0	-	1.298	11.44	597.5	10.8	-	-	-	1	ps
5	-83.08442	-14.58399	214.0	-	1.131	7.95	378.0	8.19	-	-	-	1	ps
6	-83.11959	-14.61556	310.0	-	0.668	17.04	746.8	12.61	-	-	-	0	-
7	-83.12535	-14.67718	225.0	-	1.401	0.18	7.4	0.151	-	-	-	1	ps
8	-83.0622	-14.6224	257.0	-	1.628	0.0	0.0	0.0	-	-	-	2	ps
9	-83.14111	-14.69346	197.0	-	1.156	6.48	265.1	5.0	-	-	-	0	-
10	-83.0944	-14.60716	223.0	-	0.202	10.78	480.6	9.25	-	-	-	0	-
11	-83.07749	-14.5983	216.0	-	1.346	4.39	219.5	4.42	-	-	-	1	ps
12	-83.13307	-14.65586	313.0	-	0.202	0.71	26.1	0.467	-	-	-	0	-
13	-83.09279	-14.59805	336.0	-	0.148	9.8	387.7	8.27	-	-	-	0	-
14	-83.18936	-14.58852	307.0	-	0.227	17.98	737.9	10.15	-	-	-	0	-
15	-83.07738	-14.61911	304.0	-	0.097	0.0	0.0	0.0	-	-	-	0	-
16	-83.13268	-14.58341	232.0	-	0.113	19.28	633.8	6.96	-	-	-	0	-

Table B.26: $N(H_2)$, T, and I_{250} are derived for fields with matching Herschel data and mass estimates for fields with distance estimates.

G017.38+02.26													
clump No.	RA (J2000)	dec (J2000)	pos. angle (°)	R_{eff} [pc]	F_ν (Jy)	T [K]	I_{250} [MJy/sr]	N(H_2) [10^{21}cm^{-2}]	M ($M_\odot$)	M_{BE} ($M_\odot$)	α_{BE}	N_*	type
1	-86.41128	-12.7458	246.0	-	2.068	-	-	-	-	-	-	1	ps
2	-86.40035	-12.76538	201.0	-	1.822	-	-	-	-	-	-	2	ps
3	-86.40663	-12.75642	221.0	-	0.851	-	-	-	-	-	-	1	ps
4	-86.42313	-12.73416	350.0	-	1.83	-	-	-	-	-	-	0	-
5	-86.41861	-12.71933	313.0	-	0.697	-	-	-	-	-	-	0	-
6	-86.44424	-12.70558	313.0	-	0.867	-	-	-	-	-	-	1	ps

G023.35-00.26													
clump No.	RA (J2000)	dec (J2000)	pos. angle (°)	R_{eff} [pc]	F_ν (Jy)	T [K]	I_{250} [MJy/sr]	N(H_2) [10^{21}cm^{-2}]	M ($M_\odot$)	M_{BE} ($M_\odot$)	α_{BE}	N_*	type
1	-81.29998	-8.562178	326.0	-	14.351	-	-	-	-	-	-	2	ps
2	-81.27515	-8.634685	358.0	-	11.26	-	-	-	-	-	-	6	ps
3	-81.30971	-8.571341	329.0	-	21.026	-	-	-	-	-	-	0	-
4	-81.34888	-8.70679	301.0	-	23.223	-	-	-	-	-	-	3	ps
5	-81.28861	-8.676776	349.0	-	24.697	-	-	-	-	-	-	11	ps
6	-81.34797	-8.679415	260.0	-	6.936	-	-	-	-	-	-	0	-
7	-81.33361	-8.576304	355.0	-	20.784	-	-	-	-	-	-	1	ps
8	-81.29088	-8.556714	338.0	-	2.803	-	-	-	-	-	-	4	ps
9	-81.29139	-8.594897	334.0	-	18.778	-	-	-	-	-	-	1	ps
10	-81.37965	-8.67855	200.0	-	6.267	-	-	-	-	-	-	1	ps
11	-81.29693	-8.629169	195.0	-	11.756	-	-	-	-	-	-	4	ps
12	-81.30377	-8.693733	357.0	-	9.743	-	-	-	-	-	-	4	ps
13	-81.29888	-8.607103	314.0	-	2.957	-	-	-	-	-	-	0	-
14	-81.35939	-8.568113	356.0	-	3.683	-	-	-	-	-	-	0	-
15	-81.31273	-8.626709	215.0	-	5.025	-	-	-	-	-	-	0	-
16	-81.35975	-8.630127	201.0	-	3.991	-	-	-	-	-	-	1	ps
17	-81.31977	-8.706766	251.0	-	3.144	-	-	-	-	-	-	0	-
18	-81.33119	-8.551407	266.0	-	1.319	-	-	-	-	-	-	0	-
19	-81.2418	-8.672003	242.0	-	3.688	-	-	-	-	-	-	5	ps
20	-81.34557	-8.645987	205.0	-	8.684	-	-	-	-	-	-	0	-
21	-81.38879	-8.63054	238.0	-	0.947	-	-	-	-	-	-	1	ps
22	-81.28994	-8.716836	231.0	-	4.159	-	-	-	-	-	-	0	-
23	-81.38601	-8.643149	211.0	-	1.073	-	-	-	-	-	-	0	-
24	-81.26523	-8.575315	223.0	-	1.922	-	-	-	-	-	-	4	ps
25	-81.30962	-8.649728	337.0	-	0.411	-	-	-	-	-	-	1	ps
26	-81.3216	-8.610328	277.0	-	0.682	-	-	-	-	-	-	1	ps

Table B.27: $N(H_2)$, T, and I_{250} are derived for fields with matching Herschel data and mass estimates for fields with distance estimates.

G023.68+00.58													
clump No.	RA (J2000)	dec (J2000)	pos. angle (°)	R_{eff} [pc]	F_ν (Jy)	T [K]	I_{250} [MJy/sr]	N(H_2) [10^{21}cm^{-2}]	M ($M_\odot$)	M_{BE} ($M_\odot$)	α_{BE}	N_*	type
1	-81.91062	-7.948483	234.0	-	8.162	-	-	-	-	-	-	4	ps
2	-81.93745	-8.000097	181.0	-	10.58	-	-	-	-	-	-	3	ps
3	-81.91488	-7.968799	277.0	-	2.812	-	-	-	-	-	-	1	ps
4	-81.9262	-7.978612	345.0	-	2.072	-	-	-	-	-	-	0	-
5	-81.85746	-7.902986	256.0	-	2.264	-	-	-	-	-	-	1	ps
6	-81.86958	-7.922497	228.0	-	2.88	-	-	-	-	-	-	0	-
7	-81.89734	-8.025856	197.0	-	0.542	-	-	-	-	-	-	0	-
8	-81.84765	-7.966422	343.0	-	1.202	-	-	-	-	-	-	0	-
9	-81.88342	-8.02107	186.0	-	0.43	-	-	-	-	-	-	3	ps
10	-81.88977	-8.010988	193.0	-	0.369	-	-	-	-	-	-	0	-

G023.69+00.58													
clump No.	RA (J2000)	dec (J2000)	pos. angle (°)	R_{eff} [pc]	F_ν (Jy)	T [K]	I_{250} [MJy/sr]	N(H_2) [10^{21}cm^{-2}]	M ($M_\odot$)	M_{BE} ($M_\odot$)	α_{BE}	N_*	type
1	-81.91247	-7.948849	232.0	-	7.651	-	-	-	-	-	-	3	ps
2	-81.9369	-7.994925	196.0	-	12.138	-	-	-	-	-	-	3	ps
3	-81.91482	-7.968881	269.0	-	2.587	-	-	-	-	-	-	1	ps
4	-81.85847	-7.902633	222.0	-	3.03	-	-	-	-	-	-	1	ps
5	-81.86884	-7.91902	286.0	-	1.628	-	-	-	-	-	-	0	-
6	-81.87467	-7.929259	193.0	-	0.729	-	-	-	-	-	-	0	-
7	-81.84936	-7.957463	181.0	-	0.74	-	-	-	-	-	-	1	ps
8	-81.83984	-7.885779	340.0	-	0.175	-	-	-	-	-	-	0	-
9	-81.89802	-8.025541	187.0	-	0.272	-	-	-	-	-	-	0	-
10	-81.88958	-8.011262	319.0	-	0.324	-	-	-	-	-	-	0	-

Table B.28: $N(H_2)$, T, and I_{250} are derived for fields with matching Herschel data and mass estimates for fields with distance estimates.

G024.04+00.27													
clump No.	RA (J2000)	dec (J2000)	pos. angle (°)	R_{eff} [pc]	F_ν (Jy)	T [K]	I_{250} [MJy/sr]	$N(H_2)$ [10^{21}cm^{-2}]	M ($M_\odot$)	M_{BE} ($M_\odot$)	α_{BE}	N_*	type
1	-81.40635	-7.830588	324.0	0.345	5.072	-	-	-	1152.46	9.5	0.01	1	ps
2	-81.42173	-7.829489	218.0	0.477	6.525	-	-	-	1482.73	13.1	0.01	0	pre
3	-81.39998	-7.817096	312.0	0.289	2.165	-	-	-	491.9	8.0	0.02	0	pre
4	-81.4017	-7.801553	297.0	0.558	7.636	-	-	-	1735.24	15.4	0.01	1	ps
5	-81.44468	-7.811962	321.0	0.604	6.182	-	-	-	1404.86	16.6	0.01	1	ps
6	-81.42001	-7.813209	311.0	0.331	2.792	-	-	-	634.5	9.1	0.01	0	pre
7	-81.38759	-7.813034	198.0	0.244	1.44	-	-	-	327.31	6.7	0.02	0	pre
8	-81.41314	-7.723797	244.0	0.492	3.951	-	-	-	897.91	13.6	0.02	1	ps
9	-81.41729	-7.843433	326.0	0.258	1.483	-	-	-	337.04	7.1	0.02	0	pre
10	-81.41997	-7.790374	357.0	0.197	0.778	-	-	-	176.84	5.4	0.03	1	ps
11	-81.47842	-7.851168	221.0	0.467	1.644	-	-	-	373.56	12.9	0.03	2	ps
12	-81.42186	-7.77172	309.0	0.565	3.283	-	-	-	746.0	15.6	0.02	1	ps
13	-81.44555	-7.790156	208.0	0.274	1.01	-	-	-	229.53	7.5	0.03	1	ps
14	-81.43991	-7.733247	217.0	0.459	1.592	-	-	-	361.81	12.6	0.03	1	ps
15	-81.46113	-7.827471	236.0	0.296	0.757	-	-	-	172.09	8.2	0.05	1	ps
16	-81.39124	-7.775163	289.0	0.28	0.492	-	-	-	111.71	7.7	0.07	0	pre
17	-81.51072	-7.713777	353.0	0.234	0.477	-	-	-	108.35	6.4	0.06	0	pre
18	-81.45993	-7.76779	343.0	0.45	1.174	-	-	-	266.71	12.4	0.05	0	pre
19	-81.54295	-7.768534	192.0	0.291	0.616	-	-	-	139.91	8.0	0.06	1	ps

G026.54+00.72													
clump No.	RA (J2000)	dec (J2000)	pos. angle (°)	R_{eff} [pc]	F_ν (Jy)	T [K]	I_{250} [MJy/sr]	$N(H_2)$ [10^{21}cm^{-2}]	M ($M_\odot$)	M_{BE} ($M_\odot$)	α_{BE}	N_*	type
1	-80.7197	-5.401684	228.0	0.393	7.65	-	-	-	1556.24	10.8	0.01	4	ps
2	-80.71944	-5.386769	317.0	0.115	0.344	-	-	-	69.9	3.2	0.05	0	pre
3	-80.71377	-5.343536	181.0	0.261	0.707	-	-	-	143.79	7.2	0.05	0	pre
4	-80.74882	-5.424548	195.0	0.378	0.955	-	-	-	194.31	10.4	0.05	0	pre

Table B.29: $N(H_2)$, T, and I_{250} are derived for fields with matching Herschel data and mass estimates for fields with distance estimates.

G033.73-00.01													
clump No.	RA (J2000)	dec (J2000)	pos. angle (°)	R_{eff} [pc]	F_ν (Jy)	T [K]	I_{250} [MJy/sr]	N(H_2) [10^{21}cm^{-2}]	M ($M_\odot$)	M_{BE} ($M_\odot$)	α_{BE}	N_*	type
1	-76.75578	0.7101739	254.0	-	8.107	-	-	-	-	-	-	3	ps
2	-76.79439	0.6387888	359.0	-	3.824	-	-	-	-	-	-	3	ps
3	-76.78642	0.628384	252.0	-	7.574	-	-	-	-	-	-	1	ps
4	-76.76854	0.7199641	250.0	-	8.717	-	-	-	-	-	-	2	ps
5	-76.77269	0.6435341	289.0	-	5.008	-	-	-	-	-	-	1	ps
6	-76.75803	0.6860129	196.0	-	1.816	-	-	-	-	-	-	1	ps
7	-76.77937	0.6815734	220.0	-	5.416	-	-	-	-	-	-	2	ps
8	-76.76595	0.6971789	285.0	-	2.643	-	-	-	-	-	-	0	-
9	-76.75821	0.7367358	231.0	-	2.981	-	-	-	-	-	-	1	ps
10	-76.78064	0.6596093	282.0	-	1.654	-	-	-	-	-	-	1	ps
11	-76.76995	0.6700253	250.0	-	1.265	-	-	-	-	-	-	1	ps
12	-76.76533	0.6612786	286.0	-	1.116	-	-	-	-	-	-	1	ps
13	-76.8328	0.6877186	345.0	-	2.452	-	-	-	-	-	-	3	ps
14	-76.78767	0.7551416	202.0	-	1.564	-	-	-	-	-	-	3	ps
15	-76.83337	0.7389526	283.0	-	0.523	-	-	-	-	-	-	1	ps
16	-76.72644	0.6820119	340.0	-	0.741	-	-	-	-	-	-	0	-
17	-76.80058	0.7857782	340.0	-	0.125	-	-	-	-	-	-	0	-
18	-76.69898	0.7022434	217.0	-	0.489	-	-	-	-	-	-	3	ps

G034.74-01.39													
clump No.	RA (J2000)	dec (J2000)	pos. angle (°)	R_{eff} [pc]	F_ν (Jy)	T [K]	I_{250} [MJy/sr]	N(H_2) [10^{21}cm^{-2}]	M ($M_\odot$)	M_{BE} ($M_\odot$)	α_{BE}	N_*	type
1	-75.05856	1.01922	240.0	-	26.275	-	-	-	-	-	-	4	ps
2	-75.07511	0.9868728	300.0	-	13.095	-	-	-	-	-	-	2	ps
3	-75.05614	0.999269	284.0	-	0.828	-	-	-	-	-	-	0	-
4	-75.03356	1.016304	223.0	-	0.567	-	-	-	-	-	-	1	ps
5	-75.09668	0.9681734	201.0	-	2.652	-	-	-	-	-	-	1	ps
6	-75.12232	0.9134011	283.0	-	1.356	-	-	-	-	-	-	0	-
7	-75.05218	0.9464671	299.0	-	0.115	-	-	-	-	-	-	2	ps
8	-75.10287	1.001177	350.0	-	0.577	-	-	-	-	-	-	0	-
9	-75.11475	0.8988725	235.0	-	0.182	-	-	-	-	-	-	0	-
10	-75.11801	0.9639387	198.0	-	0.319	-	-	-	-	-	-	0	-
11	-75.13148	0.951594	334.0	-	0.05	-	-	-	-	-	-	0	-

Table B.30: $N(H_2)$, T, and I_{250} are derived for fields with matching Herschel data and mass estimates for fields with distance estimates.

G035.38-01.77													
clump No.	RA (J2000)	dec (J2000)	pos. angle (°)	R_{eff} [pc]	F_ν (Jy)	T [K]	I_{250} [MJy/sr]	N(H_2) [10^{21}cm^{-2}]	M ($M_\odot$)	M_{BE} ($M_\odot$)	α_{BE}	N_*	type
1	-74.45615	1.350998	302.0	-	2.727	-	-	-	-	-	-	3	ps
2	-74.44651	1.348537	196.0	-	2.114	-	-	-	-	-	-	0	-
3	-74.45097	1.359428	279.0	-	2.032	-	-	-	-	-	-	0	-
4	-74.42472	1.324141	333.0	-	4.364	-	-	-	-	-	-	1	ps
5	-74.48617	1.369633	267.0	-	2.776	-	-	-	-	-	-	1	ps
6	-74.43485	1.345952	325.0	-	1.74	-	-	-	-	-	-	0	-
7	-74.41041	1.347526	235.0	-	0.481	-	-	-	-	-	-	0	-
8	-74.43892	1.36742	200.0	-	0.696	-	-	-	-	-	-	1	ps
9	-74.46767	1.363146	206.0	-	1.359	-	-	-	-	-	-	0	-
10	-74.43434	1.317542	182.0	-	0.247	-	-	-	-	-	-	1	ps
11	-74.40704	1.359414	200.0	-	0.432	-	-	-	-	-	-	0	-
12	-74.5023	1.357778	297.0	-	0.573	-	-	-	-	-	-	0	-
13	-74.40622	1.377598	317.0	-	0.689	-	-	-	-	-	-	0	-
14	-74.45839	1.320975	181.0	-	0.23	-	-	-	-	-	-	0	-
15	-74.42798	1.387164	250.0	-	0.133	-	-	-	-	-	-	0	-

G035.50-00.31													
clump No.	RA (J2000)	dec (J2000)	pos. angle (°)	R_{eff} [pc]	F_ν (Jy)	T [K]	I_{250} [MJy/sr]	N(H_2) [10^{21}cm^{-2}]	M ($M_\odot$)	M_{BE} ($M_\odot$)	α_{BE}	N_*	type
1	-75.72927	2.110829	312.0	-	2.14	-	-	-	-	-	-	2	ps
2	-75.74897	2.085692	252.0	-	1.494	-	-	-	-	-	-	0	-
3	-75.71573	2.18263	349.0	-	6.329	-	-	-	-	-	-	1	ps
4	-75.72184	2.143025	349.0	-	2.911	-	-	-	-	-	-	1	ps
5	-75.71255	2.141233	200.0	-	1.534	-	-	-	-	-	-	2	ps
6	-75.71483	2.156444	354.0	-	3.251	-	-	-	-	-	-	1	ps
7	-75.70214	2.119148	357.0	-	4.612	-	-	-	-	-	-	0	-
8	-75.71411	2.128915	214.0	-	3.578	-	-	-	-	-	-	1	ps
9	-75.72777	2.210819	315.0	-	1.103	-	-	-	-	-	-	2	ps
10	-75.68957	2.149937	256.0	-	1.846	-	-	-	-	-	-	1	ps
11	-75.63786	2.202066	187.0	-	0.375	-	-	-	-	-	-	2	ps
12	-75.65496	2.109701	304.0	-	0.431	-	-	-	-	-	-	0	-
13	-75.74883	2.118778	308.0	-	0.303	-	-	-	-	-	-	1	ps
14	-75.70452	2.206264	314.0	-	0.294	-	-	-	-	-	-	0	-
15	-75.68811	2.217488	248.0	-	0.098	-	-	-	-	-	-	0	-

Table B.31: $N(H_2)$, T, and I_{250} are derived for fields with matching Herschel data and mass estimates for fields with distance estimates.

G037.93+02.18													
clump No.	RA (J2000)	dec (J2000)	pos. angle (°)	R_{eff} [pc]	F_ν (Jy)	T [K]	I_{250} [MJy/sr]	N(H_2) [10^{21}cm^{-2}]	M ($M_\odot$)	M_{BE} ($M_\odot$)	α_{BE}	N_*	type
1	-76.77704	5.418807	210.0	0.085	0.989	15.32	323.8	8.0	10.82	2.6	0.24	4	ps
2	-76.78959	5.401775	207.0	0.055	0.207	15.38	286.3	6.9	2.25	1.7	0.74	0	pre
3	-76.80312	5.366689	331.0	0.067	0.23	16.06	303.6	6.21	2.33	2.1	0.91	0	pre

G039.74+01.98													
clump No.	RA (J2000)	dec (J2000)	pos. angle (°)	R_{eff} [pc]	F_ν (Jy)	T [K]	I_{250} [MJy/sr]	N(H_2) [10^{21}cm^{-2}]	M ($M_\odot$)	M_{BE} ($M_\odot$)	α_{BE}	N_*	type
1	-75.80524	6.961327	186.0	0.049	0.79	15.09	518.4	13.45	7.73	1.5	0.19	1	ps
2	-75.74245	6.972074	193.0	0.099	2.343	15.3	598.6	14.9	22.41	3.0	0.13	0	pre

G057.12+03.63													
clump No.	RA (J2000)	dec (J2000)	pos. angle (°)	R_{eff} [pc]	F_ν (Jy)	T [K]	I_{250} [MJy/sr]	N(H_2) [10^{21}cm^{-2}]	M ($M_\odot$)	M_{BE} ($M_\odot$)	α_{BE}	N_*	type
1	-69.0172	23.11212	266.0	-	2.223	-	-	-	-	-	-	2	ps
2	-69.0479	23.1364	316.0	-	1.316	-	-	-	-	-	-	1	ps
3	-69.06623	23.13704	309.0	-	0.085	-	-	-	-	-	-	0	-

G069.81-01.67													
clump No.	RA (J2000)	dec (J2000)	pos. angle (°)	R_{eff} [pc]	F_ν (Jy)	T [K]	I_{250} [MJy/sr]	N(H_2) [10^{21}cm^{-2}]	M ($M_\odot$)	M_{BE} ($M_\odot$)	α_{BE}	N_*	type
1	-56.60935	31.36828	349.0	0.073	0.732	14.68	509.5	14.2	24.24	2.1	0.09	2	ps
2	-56.61721	31.36499	332.0	0.092	0.767	13.82	461.8	16.98	28.18	2.5	0.09	2	ps
3	-56.61341	31.38326	355.0	0.064	0.182	14.83	434.6	12.01	5.94	1.9	0.32	2	ps

G070.40-01.40													
clump No.	RA (J2000)	dec (J2000)	pos. angle (°)	R_{eff} [pc]	F_ν (Jy)	T [K]	I_{250} [MJy/sr]	N(H_2) [10^{21}cm^{-2}]	M ($M_\odot$)	M_{BE} ($M_\odot$)	α_{BE}	N_*	type
1	-56.49179	32.01853	233.0	0.232	2.085	15.2	473.0	11.87	89.87	7.0	0.08	3	ps
2	-56.51999	32.01208	205.0	0.146	1.107	15.73	502.2	11.19	45.08	4.5	0.1	2	ps
3	-56.53617	32.00976	318.0	0.153	0.595	16.03	405.8	8.56	23.52	4.8	0.21	1	ps
4	-56.46119	32.03881	270.0	0.191	1.387	16.0	396.2	8.27	54.95	6.0	0.11	1	ps
5	-56.46041	31.93378	243.0	0.075	0.171	15.38	494.0	11.88	7.25	2.3	0.31	0	pre

Table B.32: $N(H_2)$, T, and I_{250} are derived for fields with matching Herschel data and mass estimates for fields with distance estimates.

G074.13+00.11													
clump No.	RA (J2000)	dec (J2000)	pos. angle (°)	R_{eff} [pc]	F_ν (Jy)	T [K]	I_{250} [MJy/sr]	N(H_2) [10^{21}cm^{-2}]	M ($M_\odot$)	M_{BE} ($M_\odot$)	α_{BE}	N_*	type
1	-55.51817	35.92256	297.0	-	2.846	-	-	-	-	-	-	1	ps
2	-55.50035	35.93349	243.0	-	2.988	-	-	-	-	-	-	1	ps
3	-55.51676	35.93133	319.0	-	0.837	-	-	-	-	-	-	0	-
4	-55.52372	35.94375	306.0	-	0.391	-	-	-	-	-	-	1	ps
5	-55.47312	35.95391	209.0	-	0.488	-	-	-	-	-	-	1	ps
6	-55.44753	36.01757	189.0	-	0.138	-	-	-	-	-	-	0	-
7	-55.54344	35.98394	309.0	-	0.39	-	-	-	-	-	-	1	ps
8	-55.50345	35.97845	182.0	-	0.579	-	-	-	-	-	-	1	ps
9	-55.55907	35.94634	222.0	-	0.176	-	-	-	-	-	-	0	-
10	-55.53764	35.95446	241.0	-	0.145	-	-	-	-	-	-	0	-

G082.40-01.84													
clump No.	RA (J2000)	dec (J2000)	pos. angle (°)	R_{eff} [pc]	F_ν (Jy)	T [K]	I_{250} [MJy/sr]	N(H_2) [10^{21}cm^{-2}]	M ($M_\odot$)	M_{BE} ($M_\odot$)	α_{BE}	N_*	type
1	-47.14967	41.41101	211.0	0.093	1.9	12.83	317.7	16.52	25.13	2.4	0.09	2	ps
2	-47.13281	41.42305	287.0	0.084	1.722	12.66	285.6	16.8	23.32	2.1	0.09	0	pre
3	-47.18083	41.38303	284.0	0.087	1.052	12.91	252.2	12.77	13.75	2.2	0.16	0	pre
4	-47.12372	41.43384	257.0	0.091	1.928	12.61	279.3	16.82	26.31	2.3	0.09	0	pre
5	-47.09382	41.44597	255.0	0.106	2.449	12.82	301.8	16.05	32.44	2.7	0.08	0	pre
6	-47.05065	41.4503	257.0	0.07	0.673	12.83	338.0	17.29	8.9	1.8	0.2	0	pre
7	-47.17598	41.40489	321.0	0.066	0.622	12.88	250.8	12.76	8.16	1.7	0.21	0	pre

G082.42-01.84													
clump No.	RA (J2000)	dec (J2000)	pos. angle (°)	R_{eff} [pc]	F_ν (Jy)	T [K]	I_{250} [MJy/sr]	N(H_2) [10^{21}cm^{-2}]	M ($M_\odot$)	M_{BE} ($M_\odot$)	α_{BE}	N_*	type
1	-47.14989	41.41103	218.0	0.064	1.554	12.8	329.8	17.26	20.64	1.6	0.08	2	ps
2	-47.12951	41.42726	234.0	0.064	2.573	12.25	311.4	20.77	37.02	1.6	0.04	0	pre
3	-47.17862	41.38233	292.0	0.064	0.36	12.61	276.2	15.45	4.91	1.6	0.32	0	pre
4	-47.04391	41.45235	232.0	0.064	0.545	13.05	363.4	17.27	6.99	1.6	0.24	1	ps
5	-47.09908	41.44473	249.0	0.064	1.234	12.55	326.4	18.75	16.99	1.6	0.09	0	pre
6	-47.17647	41.40499	345.0	0.064	0.296	12.77	274.3	14.51	3.95	1.6	0.41	0	pre
7	-47.02101	41.42318	288.0	0.064	0.215	13.64	275.9	10.87	2.55	1.7	0.68	1	ps

G087.07-04.20													
clump No.	RA (J2000)	dec (J2000)	pos. angle (°)	R_{eff} [pc]	F_ν (Jy)	T [K]	I_{250} [MJy/sr]	N(H_2) [10^{21}cm^{-2}]	M ($M_\odot$)	M_{BE} ($M_\odot$)	α_{BE}	N_*	type
1	-40.56431	43.31029	305.0	0.068	0.914	13.88	153.2	5.7	5.15	1.9	0.36	2	ps

Table B.33: $N(H_2)$, T, and I_{250} are derived for fields with matching Herschel data and mass estimates for fields with distance estimates.

G089.66-06.62													
clump No.	RA (J2000)	dec (J2000)	pos. angle (°)	R_{eff} [pc]	F_ν (Jy)	T [K]	I_{250} [MJy/sr]	N(H_2) [10^{21}cm^{-2}]	M ($M_\odot$)	M_{BE} ($M_\odot$)	α_{BE}	N_*	type
1	-35.70358	43.34443	325.0	0.091	1.039	13.6	221.2	8.71	18.13	2.4	0.13	4	ps

G091.88+04.17													
clump No.	RA (J2000)	dec (J2000)	pos. angle (°)	R_{eff} [pc]	F_ν (Jy)	T [K]	I_{250} [MJy/sr]	N(H_2) [10^{21}cm^{-2}]	M ($M_\odot$)	M_{BE} ($M_\odot$)	α_{BE}	N_*	type
1	-44.84408	52.47297	336.0	-	3.632	12.29	314.5	20.07	-	-	-	2	ps
2	-44.89852	52.51374	182.0	-	1.99	13.17	393.4	17.79	-	-	-	2	ps
3	-44.91097	52.45275	320.0	-	1.159	14.08	328.4	11.02	-	-	-	7	ps
4	-44.98308	52.4946	334.0	-	0.37	11.68	222.0	11.7	-	-	-	0	-
5	-44.81652	52.44857	336.0	-	0.241	12.75	235.1	12.42	-	-	-	0	-
6	-44.93121	52.44942	346.0	-	0.212	13.13	249.8	11.55	-	-	-	1	ps
7	-44.85759	52.43571	266.0	-	0.06	13.46	234.1	9.72	-	-	-	0	-
8	-44.8946	52.54656	189.0	-	0.427	13.11	292.4	13.61	-	-	-	0	-
9	-44.90562	52.49291	267.0	-	0.117	13.16	320.1	14.87	-	-	-	0	-
10	-44.96678	52.46578	311.0	-	0.039	13.4	223.7	9.55	-	-	-	0	-

G092.04+03.92													
clump No.	RA (J2000)	dec (J2000)	pos. angle (°)	R_{eff} [pc]	F_ν (Jy)	T [K]	I_{250} [MJy/sr]	N(H_2) [10^{21}cm^{-2}]	M ($M_\odot$)	M_{BE} ($M_\odot$)	α_{BE}	N_*	type
1	-44.47825	52.48075	273.0	0.036	0.487	13.93	372.3	13.34	3.57	1.0	0.28	3	ps
2	-44.40437	52.47834	342.0	0.103	3.389	12.4	415.0	25.6	30.51	2.5	0.08	0	pre
3	-44.5003	52.48225	284.0	0.035	0.355	13.6	328.4	13.02	2.71	0.9	0.35	2	ps
4	-44.33723	52.50718	255.0	0.088	1.766	13.0	378.0	18.34	14.59	2.3	0.15	1	ps
5	-44.2978	52.51606	268.0	0.06	0.75	12.9	394.9	19.77	6.28	1.5	0.24	2	ps
6	-44.43393	52.46663	244.0	0.053	0.672	12.46	375.1	22.27	5.99	1.3	0.22	0	pre
7	-44.27504	52.52196	233.0	0.044	0.387	12.75	406.9	21.49	3.31	1.1	0.33	0	pre
8	-44.39861	52.43926	194.0	0.08	1.001	12.71	393.8	21.16	8.62	2.0	0.23	0	pre

G092.28+03.79													
clump No.	RA (J2000)	dec (J2000)	pos. angle (°)	R_{eff} [pc]	F_ν (Jy)	T [K]	I_{250} [MJy/sr]	N(H_2) [10^{21}cm^{-2}]	M ($M_\odot$)	M_{BE} ($M_\odot$)	α_{BE}	N_*	type
1	-43.98144	52.56507	208.0	0.111	10.058	12.97	656.6	31.0	83.48	2.8	0.03	8	ps
2	-43.90447	52.53113	302.0	0.017	0.198	13.79	432.6	16.15	1.47	0.5	0.31	2	ps

Table B.34: $N(H_2)$, T, and I_{250} are derived for fields with matching Herschel data and mass estimates for fields with distance estimates.

G093.51-04.31													
clump No.	RA (J2000)	dec (J2000)	pos. angle (°)	R_{eff} [pc]	F_ν (Jy)	T [K]	I_{250} [MJy/sr]	N(H_2) [10^{21}cm^{-2}]	M ($M_\odot$)	M_{BE} ($M_\odot$)	α_{BE}	N_*	type
1	-33.71417	47.55241	253.0	-	0.892	14.59	371.9	10.99	-	-	-	3	ps
2	-33.78246	47.67466	290.0	-	2.137	13.44	274.3	11.4	-	-	-	3	ps
3	-33.75871	47.69911	295.0	-	0.391	13.22	182.7	8.41	-	-	-	1	ps
4	-33.76021	47.66201	256.0	-	2.481	11.87	177.0	13.76	-	-	-	0	-
5	-33.74018	47.55235	294.0	-	0.263	13.11	185.2	8.58	-	-	-	1	ps
6	-33.71619	47.5632	274.0	-	0.177	12.92	155.5	7.76	-	-	-	0	-
7	-33.75108	47.56791	339.0	-	0.321	12.67	149.1	8.13	-	-	-	0	-
8	-33.78862	47.61729	249.0	-	0.333	12.74	180.3	9.56	-	-	-	1	ps

G105.44+09.88													
clump No.	RA (J2000)	dec (J2000)	pos. angle (°)	R_{eff} [pc]	F_ν (Jy)	T [K]	I_{250} [MJy/sr]	N(H_2) [10^{21}cm^{-2}]	M ($M_\odot$)	M_{BE} ($M_\odot$)	α_{BE}	N_*	type
1	-34.24698	66.05585	325.0	0.067	5.822	3.88	131.0	3.1	1725.46	0.5	0.0	3	ps
2	-34.22749	66.11793	342.0	0.106	10.982	20.71	1357.3	10.48	53.06	4.3	0.08	27	ps
3	-34.25684	66.08813	222.0	0.082	2.643	21.27	813.0	6.82	12.28	3.5	0.28	5	ps
4	-34.18627	66.1299	331.0	0.096	2.861	16.26	505.8	9.76	20.03	3.1	0.15	8	ps
5	-34.16285	66.14258	312.0	0.066	1.105	14.54	295.6	8.02	9.3	1.9	0.2	3	ps
6	-34.14689	66.05523	261.0	0.052	0.439	4.43	77.1	3.36	74.94	0.5	0.01	1	ps
7	-34.30018	66.06288	201.0	0.039	0.309	8.79	186.6	4.85	6.92	0.7	0.1	0	pre
8	-34.23164	66.18611	291.0	0.076	0.453	14.28	178.5	5.75	3.93	2.1	0.55	2	ps
9	-34.23677	66.17733	290.0	0.034	0.147	14.31	189.4	6.1	1.28	1.0	0.75	1	ps
10	-34.17202	66.17469	181.0	0.013	0.037	14.46	174.4	5.34	0.31	0.4	1.19	0	pre

G107.18+05.44													
clump No.	RA (J2000)	dec (J2000)	pos. angle (°)	R_{eff} [pc]	F_ν (Jy)	T [K]	I_{250} [MJy/sr]	N(H_2) [10^{21}cm^{-2}]	M ($M_\odot$)	M_{BE} ($M_\odot$)	α_{BE}	N_*	type
1	-24.6074	63.62026	311.0	0.08	6.047	-	-	-	44.21	2.2	0.05	4	ps
2	-24.6548	63.62566	182.0	0.042	1.099	-	-	-	8.03	1.2	0.14	0	pre
3	-24.67876	63.6287	231.0	0.045	1.249	-	-	-	9.13	1.2	0.14	2	ps
4	-24.69482	63.64687	284.0	0.087	2.67	-	-	-	19.52	2.4	0.12	3	ps
5	-24.6673	63.58996	220.0	0.031	0.281	-	-	-	2.06	0.8	0.42	0	pre

G107.26+05.71													
clump No.	RA (J2000)	dec (J2000)	pos. angle (°)	R_{eff} [pc]	F_ν (Jy)	T [K]	I_{250} [MJy/sr]	N(H_2) [10^{21}cm^{-2}]	M ($M_\odot$)	M_{BE} ($M_\odot$)	α_{BE}	N_*	type
1	-24.64496	63.86031	355.0	0.08	12.308	-	-	-	89.99	2.2	0.02	1	ps
2	-24.65313	63.87947	299.0	0.038	0.823	-	-	-	6.01	1.1	0.17	0	pre
3	-24.6872	63.87848	282.0	0.05	0.792	-	-	-	5.79	1.4	0.24	0	pre
4	-24.71897	63.88493	301.0	0.046	0.545	-	-	-	3.99	1.3	0.32	0	pre
5	-24.78313	63.85675	230.0	0.075	0.933	-	-	-	6.82	2.1	0.3	1	ps

Table B.35: $N(H_2)$, T, and I_{250} are derived for fields with matching Herschel data and mass estimates for fields with distance estimates.

G109.70+02.52													
clump No.	RA (J2000)	dec (J2000)	pos. angle (°)	R_{eff} [pc]	F_ν (Jy)	T [K]	I_{250} [MJy/sr]	N(H_2) [10^{21}cm^{-2}]	M ($M_\odot$)	M_{BE} ($M_\odot$)	α_{BE}	N_*	type
1	-16.54789	62.40362	353.0	0.035	0.573	20.56	690.7	6.18	2.26	1.4	0.63	3	ps
2	-16.64547	62.30537	224.0	0.023	0.325	15.52	580.4	13.63	1.98	0.7	0.36	1	ps
3	-16.70406	62.28828	226.0	0.024	0.281	16.8	534.7	9.4	1.51	0.8	0.53	2	ps
4	-16.49578	62.35025	191.0	0.028	0.21	19.53	761.4	8.07	0.89	1.1	1.21	2	ps
5	-16.68918	62.37006	314.0	0.063	0.4	15.84	432.9	9.41	2.36	2.0	0.83	2	ps

G109.81+02.72													
clump No.	RA (J2000)	dec (J2000)	pos. angle (°)	R_{eff} [pc]	F_ν (Jy)	T [K]	I_{250} [MJy/sr]	N(H_2) [10^{21}cm^{-2}]	M ($M_\odot$)	M_{BE} ($M_\odot$)	α_{BE}	N_*	type
1	-16.57727	62.52967	313.0	0.054	2.36	14.31	596.9	18.36	16.5	1.5	0.09	14	ps
2	-16.62741	62.54477	195.0	0.067	1.205	14.14	342.3	11.59	8.6	1.9	0.22	8	ps

G139.14-03.23													
clump No.	RA (J2000)	dec (J2000)	pos. angle (°)	R_{eff} [pc]	F_ν (Jy)	T [K]	I_{250} [MJy/sr]	N(H_2) [10^{21}cm^{-2}]	M ($M_\odot$)	M_{BE} ($M_\odot$)	α_{BE}	N_*	type
1	42.59483	55.85764	304.0	0.206	1.946	15.09	322.6	8.02	121.45	6.1	0.05	1	ps
2	42.5859	55.8479	308.0	0.2	1.922	15.22	394.4	10.31	118.3	6.0	0.05	3	ps

G159.23-20.09													
clump No.	RA (J2000)	dec (J2000)	pos. angle (°)	R_{eff} [pc]	F_ν (Jy)	T [K]	I_{250} [MJy/sr]	N(H_2) [10^{21}cm^{-2}]	M ($M_\odot$)	M_{BE} ($M_\odot$)	α_{BE}	N_*	type
1	53.32615	31.15789	309.0	0.039	7.27	12.37	554.0	31.35	14.07	0.9	0.07	2	ps
2	53.33676	31.12664	188.0	0.04	10.569	11.39	515.6	48.98	23.88	0.9	0.04	3	ps
3	53.308	31.11748	276.0	0.045	7.084	11.79	413.2	32.19	14.99	1.1	0.07	2	ps
4	53.31735	31.13111	276.0	0.02	1.246	12.33	519.1	31.78	2.42	0.5	0.2	2	ps
5	53.36107	31.11442	184.0	0.023	0.708	12.99	388.6	19.12	1.25	0.6	0.47	1	ps
6	53.28259	31.08613	235.0	0.036	1.723	11.96	309.1	22.98	3.55	0.8	0.24	1	ps
7	53.26963	31.11062	245.0	0.019	0.508	11.73	247.4	19.54	1.09	0.4	0.41	0	pre
8	53.35446	31.09559	198.0	0.019	0.424	12.6	298.4	16.83	0.79	0.5	0.6	0	pre
9	53.2943	31.14992	245.0	0.023	0.208	12.43	266.8	16.01	0.4	0.6	1.42	0	pre

G162.46-08.69													
clump No.	RA (J2000)	dec (J2000)	pos. angle (°)	R_{eff} [pc]	F_ν (Jy)	T [K]	I_{250} [MJy/sr]	N(H_2) [10^{21}cm^{-2}]	M ($M_\odot$)	M_{BE} ($M_\odot$)	α_{BE}	N_*	type
1	65.40603	37.57992	350.0	0.041	2.284	-	-	-	5.28	1.1	0.21	3	ps
2	65.42395	37.56251	298.0	0.051	1.932	-	-	-	4.47	1.4	0.31	1	ps
3	65.3094	37.62622	186.0	0.022	0.416	-	-	-	0.96	0.6	0.63	0	pre
4	65.32206	37.5595	194.0	0.031	0.706	-	-	-	1.63	0.8	0.52	0	pre
5	65.30843	37.61044	343.0	0.025	0.421	-	-	-	0.97	0.7	0.71	0	pre

Table B.36: $N(H_2)$, T, and I_{250} are derived for fields with matching Herschel data and mass estimates for fields with distance estimates.

G171.53-14.91													
clump No.	RA (J2000)	dec (J2000)	pos. angle (°)	R_{eff} [pc]	F_ν (Jy)	T [K]	I_{250} [MJy/sr]	N(H_2) [10^{21}cm^{-2}]	M ($M_\odot$)	M_{BE} ($M_\odot$)	α_{BE}	N_*	type
1	67.16399	26.86062	351.0	-	2.309	-	-	-	-	-	-	3	ps
2	67.26996	26.81911	278.0	-	0.164	-	-	-	-	-	-	2	ps

G172.89+02.28													
clump No.	RA (J2000)	dec (J2000)	pos. angle (°)	R_{eff} [pc]	F_ν (Jy)	T [K]	I_{250} [MJy/sr]	N(H_2) [10^{21}cm^{-2}]	M ($M_\odot$)	M_{BE} ($M_\odot$)	α_{BE}	N_*	type
1	84.22747	36.17014	342.0	-	4.988	-	-	-	-	-	-	1	ps
2	84.21362	36.17966	210.0	-	4.24	-	-	-	-	-	-	2	ps
3	84.32088	36.19331	229.0	-	0.889	-	-	-	-	-	-	0	-
4	84.19201	36.17916	302.0	-	0.196	-	-	-	-	-	-	0	-
5	84.29967	36.18505	218.0	-	0.037	-	-	-	-	-	-	0	-
6	84.22339	36.21441	182.0	-	0.089	-	-	-	-	-	-	0	-

G173.15+02.40													
clump No.	RA (J2000)	dec (J2000)	pos. angle (°)	R_{eff} [pc]	F_ν (Jy)	T [K]	I_{250} [MJy/sr]	N(H_2) [10^{21}cm^{-2}]	M ($M_\odot$)	M_{BE} ($M_\odot$)	α_{BE}	N_*	type
1	84.50722	35.97131	261.0	0.121	4.163	-	-	-	190.23	3.3	0.02	1	ps
2	84.50439	35.98595	221.0	0.276	10.4	-	-	-	475.25	7.6	0.02	2	ps
3	84.5052	35.95872	321.0	0.178	3.702	-	-	-	169.16	4.9	0.03	3	ps
4	84.5194	36.01046	337.0	0.101	0.975	-	-	-	44.53	2.8	0.06	1	ps
5	84.51306	36.02051	248.0	0.117	0.898	-	-	-	41.05	3.2	0.08	3	ps
6	84.48726	36.0134	310.0	0.176	1.149	-	-	-	52.51	4.8	0.09	1	ps
7	84.55107	35.94138	185.0	0.109	0.458	-	-	-	20.93	3.0	0.14	0	pre
8	84.46385	36.0274	334.0	0.076	0.305	-	-	-	13.95	2.1	0.15	1	ps
9	84.51352	35.93403	215.0	0.036	0.099	-	-	-	4.51	1.0	0.22	1	ps
10	84.48981	36.03336	199.0	0.061	0.187	-	-	-	8.56	1.7	0.2	0	pre

G178.28-00.60													
clump No.	RA (J2000)	dec (J2000)	pos. angle (°)	R_{eff} [pc]	F_ν (Jy)	T [K]	I_{250} [MJy/sr]	N(H_2) [10^{21}cm^{-2}]	M ($M_\odot$)	M_{BE} ($M_\odot$)	α_{BE}	N_*	type
1	84.77476	30.09266	346.0	-	1.189	12.89	258.9	13.1	-	-	-	1	ps
2	84.78268	30.07977	267.0	-	0.884	13.31	267.1	11.65	-	-	-	2	ps
3	84.78477	30.06294	328.0	-	0.814	13.18	284.0	12.84	-	-	-	1	ps
4	84.77772	30.11327	221.0	-	0.692	13.14	223.9	10.36	-	-	-	0	-
5	84.82614	30.14082	282.0	-	0.37	13.62	205.2	8.11	-	-	-	0	-
6	84.80849	30.05803	196.0	-	0.339	14.04	223.6	7.73	-	-	-	2	ps
7	84.77361	30.0519	244.0	-	0.64	13.99	231.0	8.23	-	-	-	0	-

Table B.37: $N(H_2)$, T, and I_{250} are derived for fields with matching Herschel data and mass estimates for fields with distance estimates.

G195.73-02.28													
clump No.	RA (J2000)	dec (J2000)	pos. angle (°)	R_{eff} [pc]	F_ν (Jy)	T [K]	I_{250} [MJy/sr]	N(H_2) [10^{21}cm^{-2}]	M ($M_\odot$)	M_{BE} ($M_\odot$)	α_{BE}	N_*	type
1	92.74169	14.15736	290.0	0.088	3.994	14.04	488.1	15.47	45.07	2.4	0.05	3	ps
2	92.71184	14.17126	299.0	0.092	2.52	13.41	326.5	13.85	30.8	2.4	0.08	3	ps
3	92.75408	14.15042	337.0	0.039	0.496	12.5	238.6	13.66	6.88	1.0	0.14	0	pre

G202.31+02.53													
clump No.	RA (J2000)	dec (J2000)	pos. angle (°)	R_{eff} [pc]	F_ν (Jy)	T [K]	I_{250} [MJy/sr]	N(H_2) [10^{21}cm^{-2}]	M ($M_\odot$)	M_{BE} ($M_\odot$)	α_{BE}	N_*	type
1	100.2427	10.61498	187.0	0.046	4.328	16.05	961.3	17.42	22.56	1.5	0.06	3	ps
2	100.2471	10.60208	217.0	0.041	2.153	14.54	686.0	19.7	13.22	1.2	0.09	2	ps
3	100.2603	10.59641	220.0	0.093	4.299	12.71	406.0	22.33	33.4	2.3	0.07	3	ps
4	100.2813	10.52251	277.0	0.036	0.881	12.75	311.1	16.23	6.81	0.9	0.13	3	ps
5	100.2221	10.55431	231.0	0.069	0.497	13.72	293.6	11.26	3.37	1.9	0.55	2	ps
6	100.2665	10.57407	192.0	0.069	1.949	13.09	326.3	15.45	14.36	1.8	0.12	5	ps
7	100.2482	10.63891	208.0	0.064	1.286	12.32	208.2	13.09	10.57	1.6	0.15	1	ps
8	100.274	10.52893	261.0	0.016	0.15	12.77	248.5	13.07	1.15	0.4	0.35	1	ps
9	100.2342	10.55251	357.0	0.021	0.225	13.99	307.3	10.77	1.47	0.6	0.39	0	pre
10	100.2461	10.5329	259.0	0.021	0.216	13.71	263.7	10.06	1.47	0.6	0.39	0	pre
11	100.2866	10.55751	336.0	0.026	0.268	13.74	252.4	9.47	1.82	0.7	0.39	0	pre

G215.87-17.50													
clump No.	RA (J2000)	dec (J2000)	pos. angle (°)	R_{eff} [pc]	F_ν (Jy)	T [K]	I_{250} [MJy/sr]	N(H_2) [10^{21}cm^{-2}]	M ($M_\odot$)	M_{BE} ($M_\odot$)	α_{BE}	N_*	type
1	88.38435	-10.41943	235.0	0.03	1.297	-	-	-	2.68	0.8	0.31	0	pre
2	88.42803	-10.40275	295.0	0.041	1.622	-	-	-	3.35	1.1	0.34	7	ps
3	88.43248	-10.39512	351.0	0.021	0.539	-	-	-	1.11	0.6	0.52	2	ps
4	88.35876	-10.45928	256.0	0.026	0.691	-	-	-	1.43	0.7	0.5	3	ps
5	88.40052	-10.4201	248.0	0.016	0.204	-	-	-	0.42	0.4	1.05	0	pre

Table B.38: $N(H_2)$, T, and I_{250} are derived for fields with matching Herschel data and mass estimates for fields with distance estimates.

C. Figures

Intensity maps of all available wavelengths: Sect. C.1

$N(H_2)$ maps with SCUBA-2 contours on top: Sect. C.2

Clumps and YSOs plotted on SCUBA-2 fields: Sect. C.3

CO line plots: Sect. C.4

C.1 Intensity maps of all available wavelengths

Intensity maps of all available data in the seven wavelengths (clockwise from top left: 70 μm, 100 μm, 160 μm, 850 μm, 500 μm, 350 μm, and 250 μm). Blank space denotes a lack of data in that particular wavelength. The wavelength of the field is written above the colorbar and the name of the SCUBA-2 field is at the bottom of each 850-μm image, along with coordinates in the Equatorial J2000 coordinate system. The units of the 850-μm maps are mJy/arcsec^2, all others are in MJy/sr.

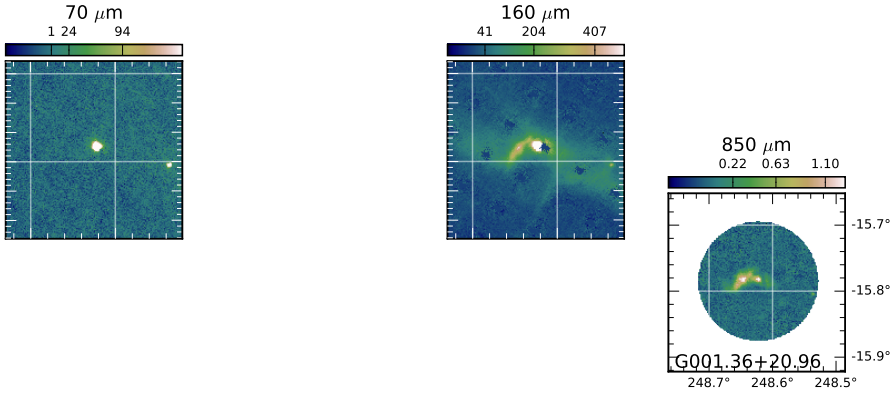

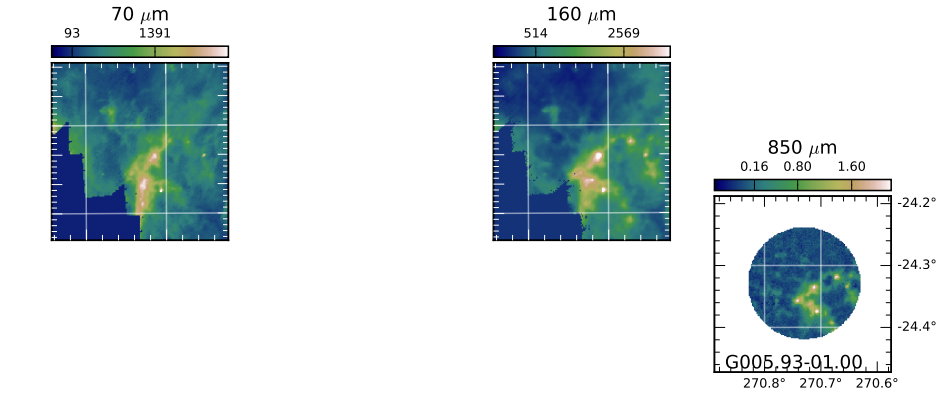
70 μm
93 1391
160 μm
514 2569
850 μm
0.16 0.80 1.60
-24.2°
-24.3°
-24.4°
G005.93-01.00
270.8° 270.7° 270.6°

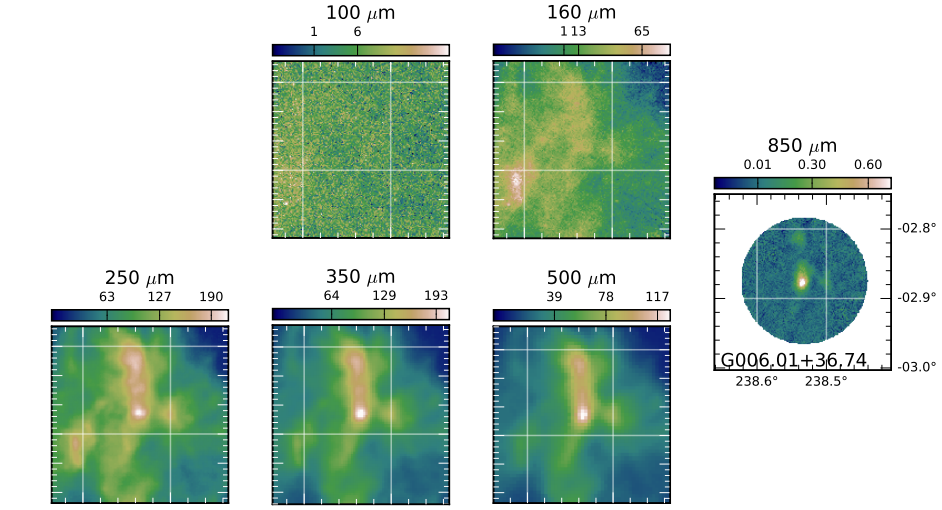
100 μm
1 6
160 μm
1 13 65
850 μm
0.01 0.30 0.60
-02.8°
-02.9°
-03.0°
G006.01+36.74
238.6° 238.5°
250 μm
63 127 190
350 μm
64 129 193
500 μm
39 78 117

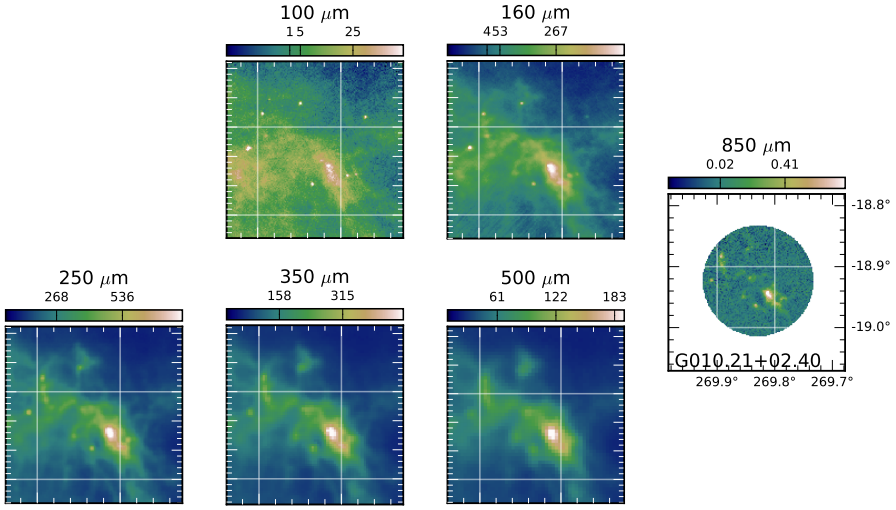
100 μm
1 5 25
160 μm
453 267
850 μm
0.02 0.41
-18.8°
-18.9°
-19.0°
G010.21+02.40
269.9° 269.8° 269.7°
250 μm
268 536
350 μm
158 315
500 μm
61 122 183

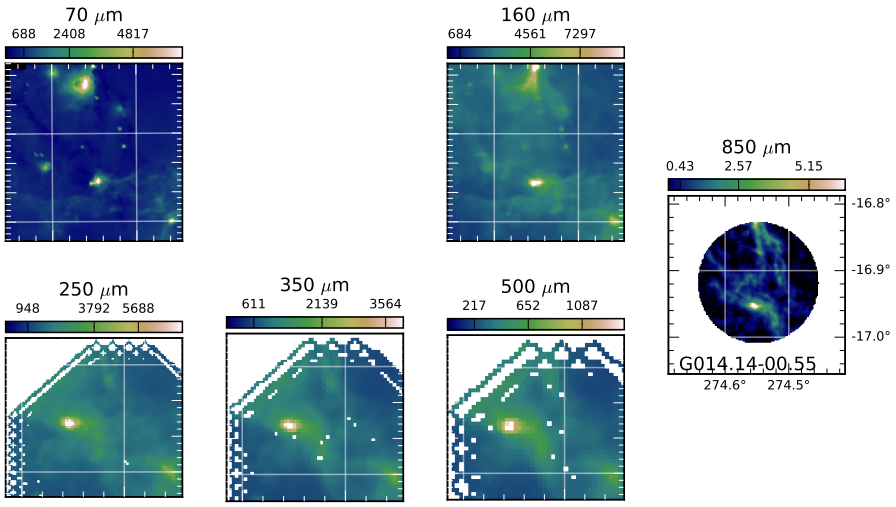
70 μm
688 2408 4817
160 μm
684 4561 7297
850 μm
0.43 2.57 5.15
-16.8°
-16.9°
-17.0°
G014.14-00.55
274.6° 274.5°
250 μm
948 3792 5688
350 μm
611 2139 3564
500 μm
217 652 1087

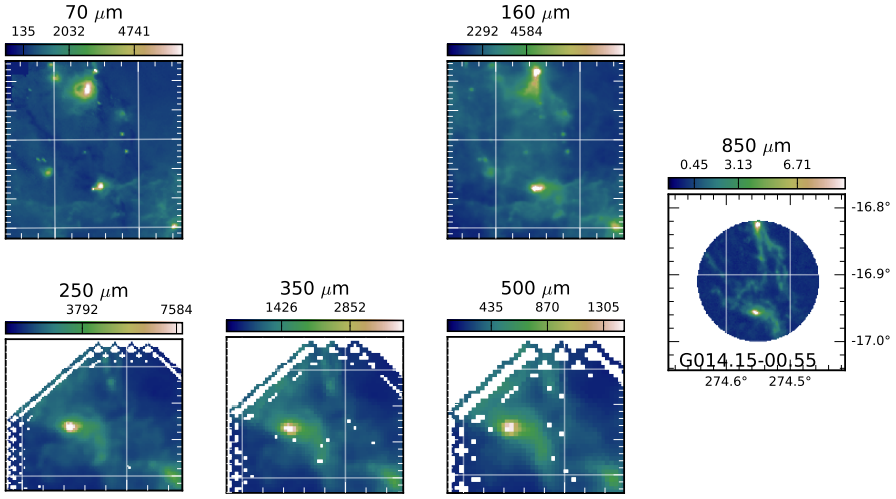
70 μm
135 2032 4741
160 μm
2292 4584
850 μm
0.45 3.13 6.71
250 μm
3792 7584
350 μm
1426 2852
500 μm
435 870 1305
-16.8°
-16.9°
-17.0°
G014.15-00.55
274.6° 274.5°

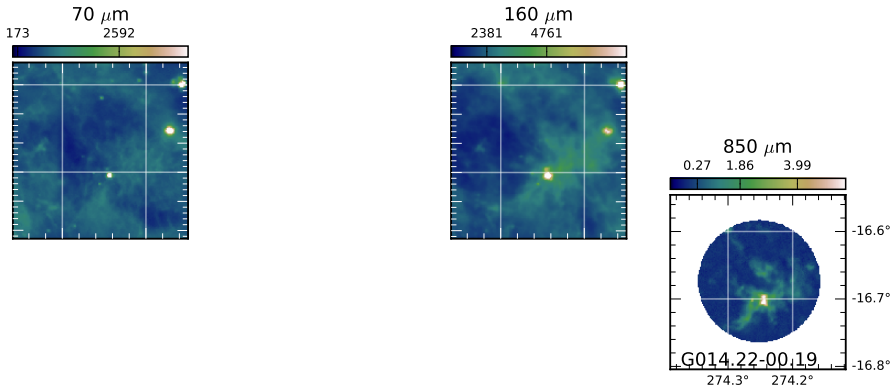
70 μm
173 2592
160 μm
2381 4761
850 μm
0.27 1.86 3.99
-16.6°
-16.7°
-16.8°
G014.22-00.19
274.3° 274.2°

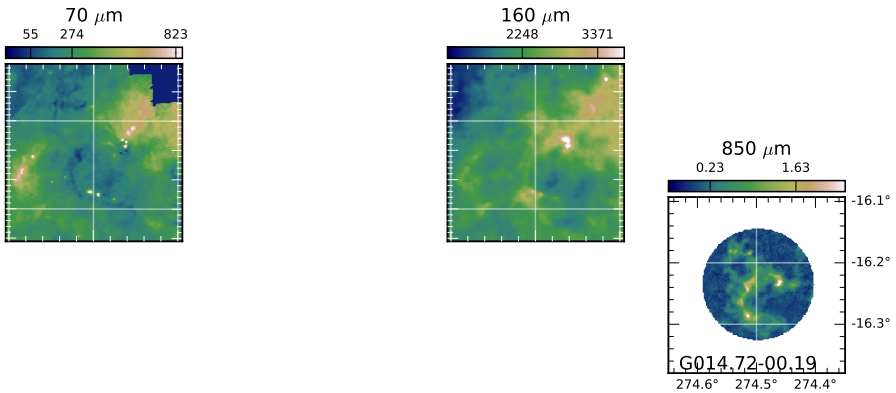
70 μm
55 274 823
160 μm
2248 3371
850 μm
0.23 1.63
-16.1°
-16.2°
-16.3°
G014.72-00.19
274.6° 274.5° 274.4°

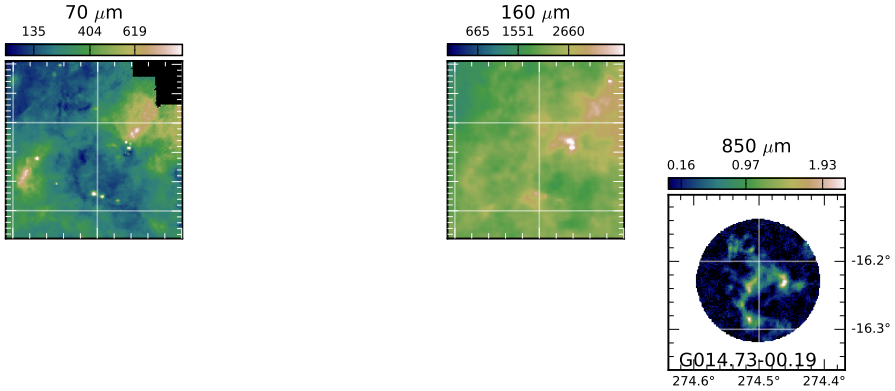
70 μm
135 404 619
160 μm
665 1551 2660
850 μm
0.16 0.97 1.93
-16.2°
-16.3°
G014.73-00.19
274.6° 274.5° 274.4°

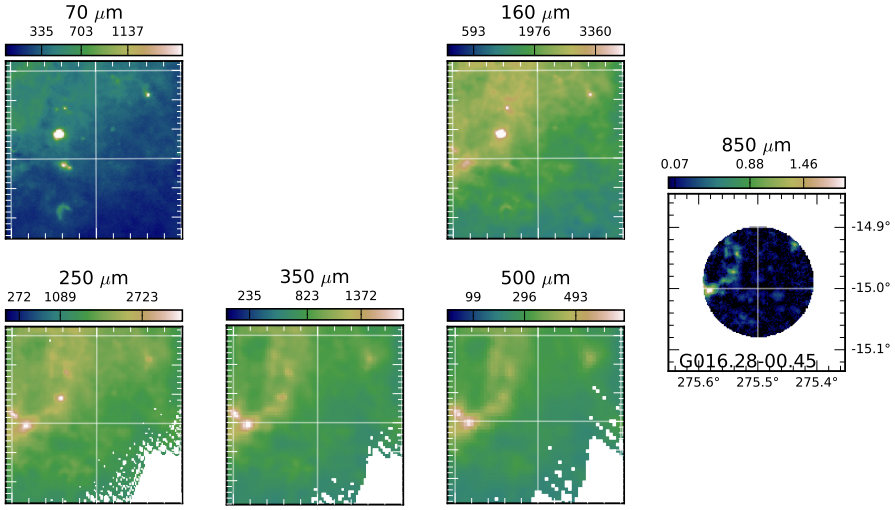
70 μm
335 703 1137
160 μm
593 1976 3360
850 μm
0.07 0.88 1.46
250 μm
272 1089 2723
350 μm
235 823 1372
500 μm
99 296 493
-14.9°
-15.0°
-15.1°
G016.28-00.45
275.6° 275.5° 275.4°

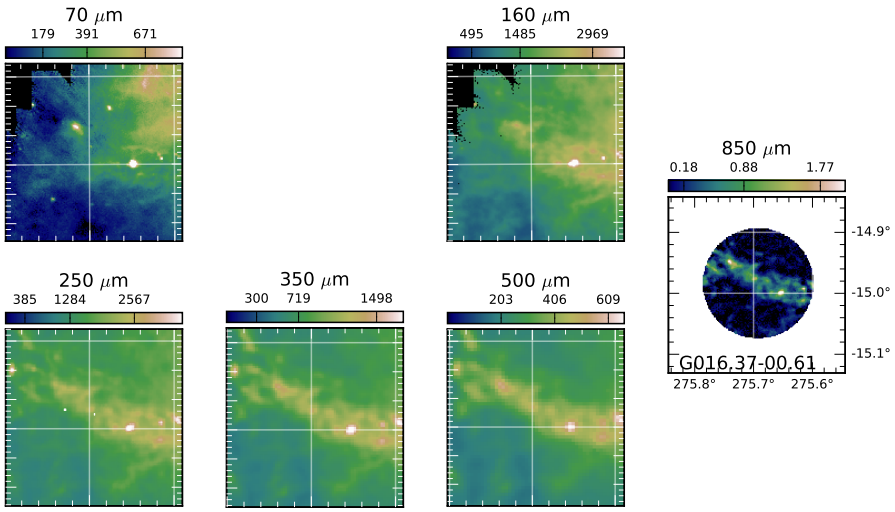
70 μm
179 391 671
160 μm
495 1485 2969
850 μm
0.18 0.88 1.77
250 μm
385 1284 2567
350 μm
300 719 1498
500 μm
203 406 609
-14.9°
-15.0°
-15.1°
G016.37-00.61
275.8° 275.7° 275.6°

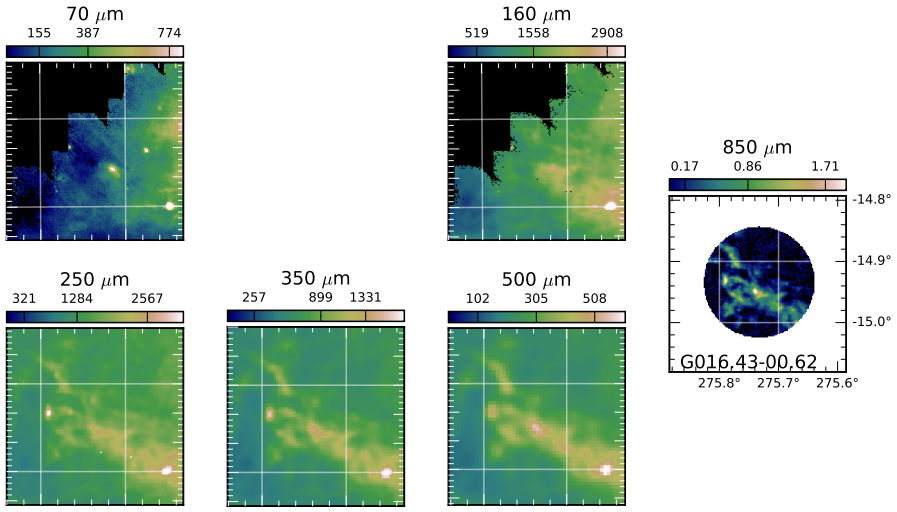
70 μm
155 387 774
160 μm
519 1558 2908
850 μm
0.17 0.86 1.71
250 μm
321 1284 2567
350 μm
257 899 1331
500 μm
102 305 508
-14.8°
-14.9°
-15.0°
G016.43-00.62
275.8° 275.7° 275.6°

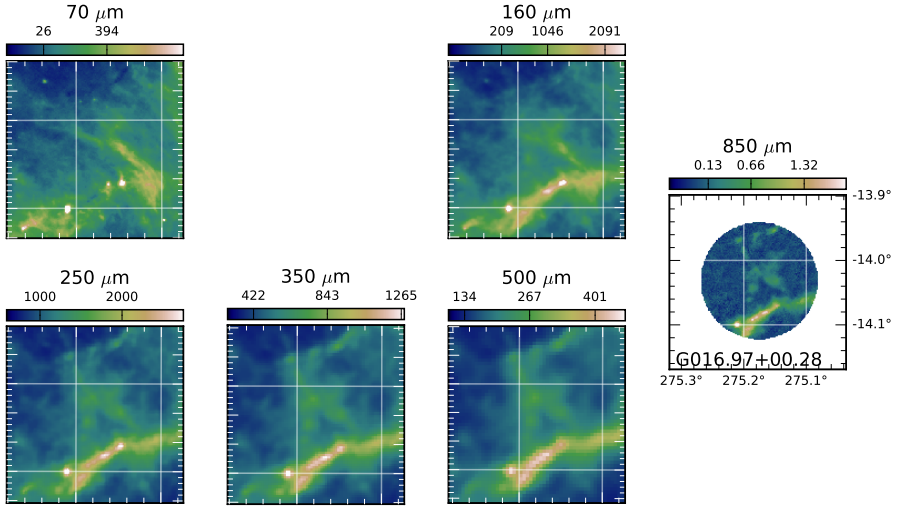
70 μm
26 394
160 μm
209 1046 2091
850 μm
0.13 0.66 1.32
250 μm
1000 2000
350 μm
422 843 1265
500 μm
134 267 401
-13.9°
-14.0°
-14.1°
G016.97+00.28
275.3° 275.2° 275.1°

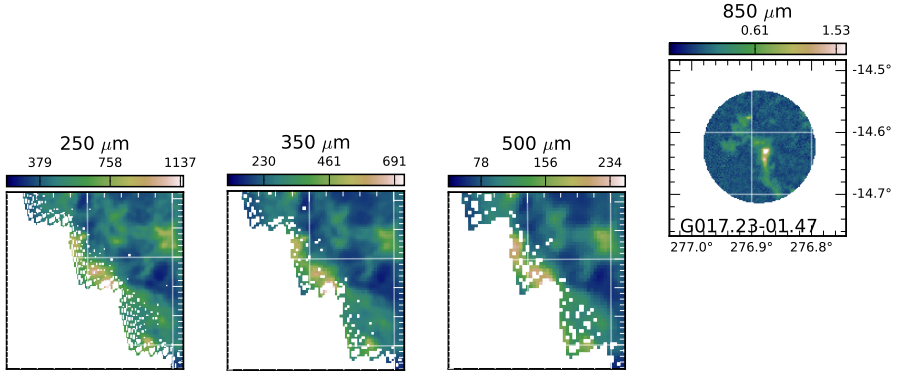
850 μm
0.61 1.53
250 μm
379 758 1137
350 μm
230 461 691
500 μm
78 156 234
-14.5°
-14.6°
-14.7°
G017.23-01.47
277.0° 276.9° 276.8°

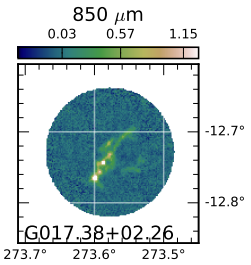
850 μm
0.03 0.57 1.15
-12.7°
-12.8°
G017.38+02.26
273.7° 273.6° 273.5°

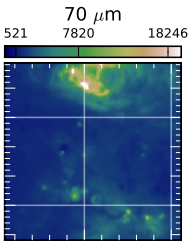
70 μm
521 7820 18246

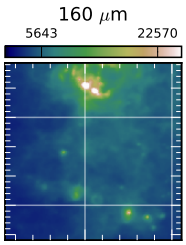
160 μm
5643 22570

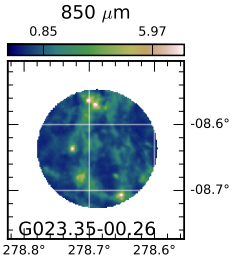
850 μm
0.85 5.97
-08.6°
-08.7°
G023.35-00.26
278.8° 278.7° 278.6°

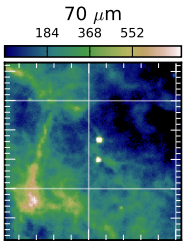
70 μm
184 368 552

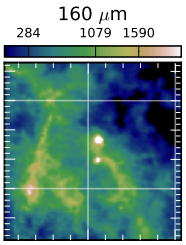
160 μm
284 1079 1590

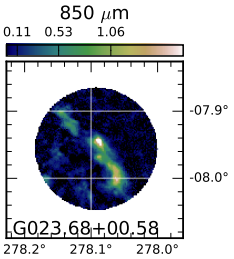
850 μm
0.11 0.53 1.06
-07.9°
-08.0°
G023.68+00.58
278.2° 278.1° 278.0°

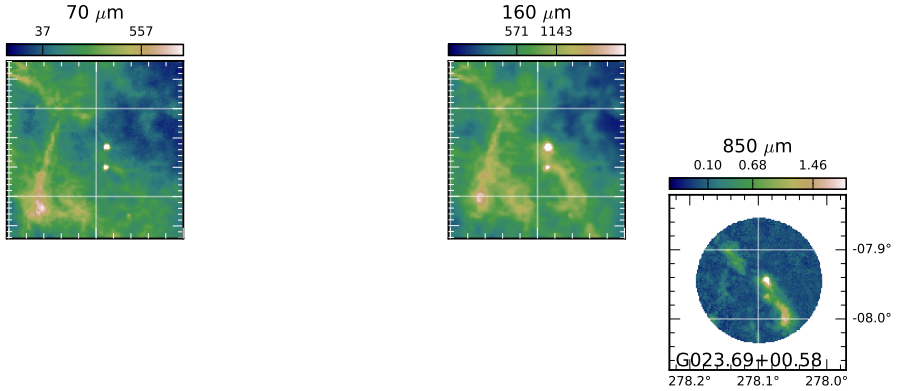
70 μm
37
557
160 μm
571
1143
850 μm
0.10
0.68
1.46
-07.9°
-08.0°
G023.69+00.58
278.2°
278.1°
278.0°

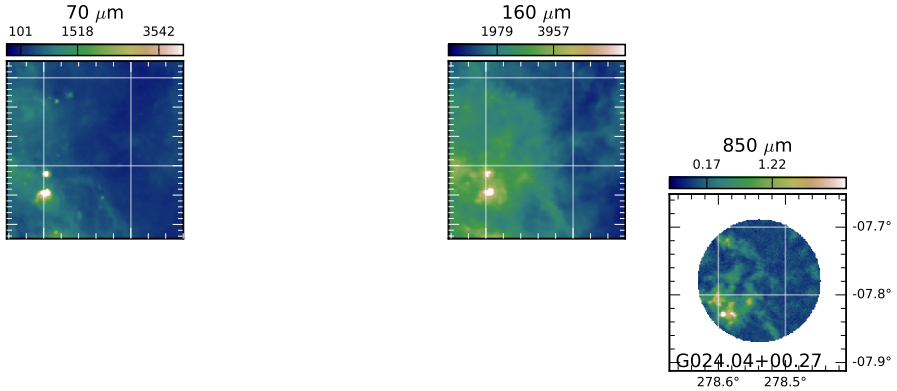
70 μm
101
1518
3542
160 μm
1979
3957
850 μm
0.17
1.22
-07.7°
-07.8°
-07.9°
G024.04+00.27
278.6°
278.5°

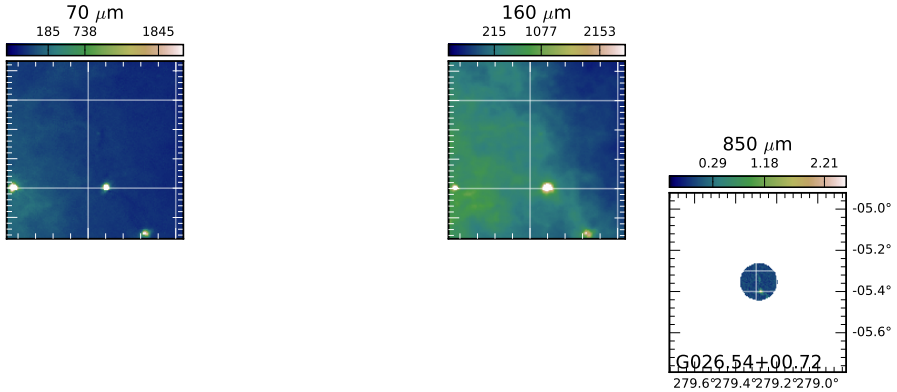
70 μm
185
738
1845
160 μm
215
1077
2153
850 μm
0.29
1.18
2.21
-05.0°
-05.2°
-05.4°
-05.6°
G026.54+00.72
279.6°279.4°279.2°279.0°

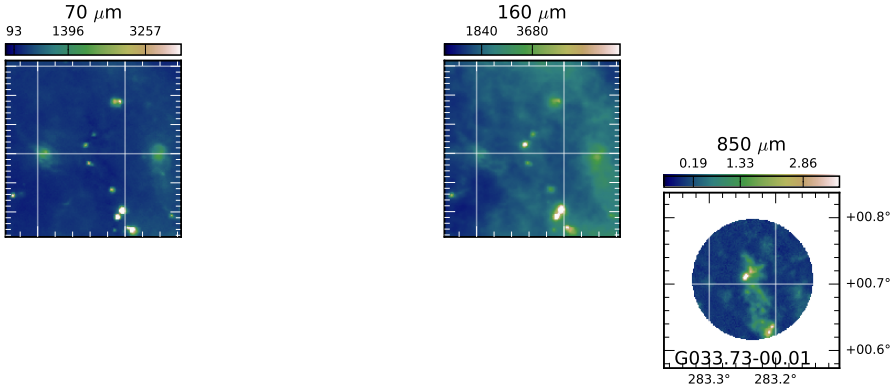
70 μm
93 1396 3257
160 μm
1840 3680
850 μm
0.19 1.33 2.86
+00.8°
+00.7°
+00.6°
G033.73-00.01
283.3° 283.2°

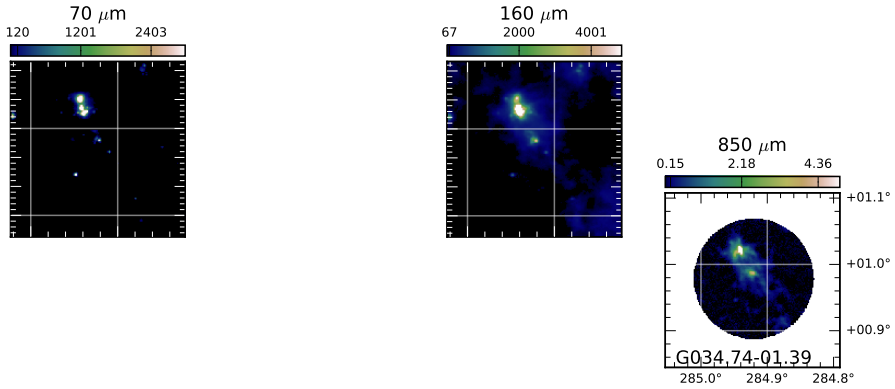
70 μm
120 1201 2403
160 μm
67 2000 4001
850 μm
0.15 2.18 4.36
+01.1°
+01.0°
+00.9°
G034.74-01.39
285.0° 284.9° 284.8°

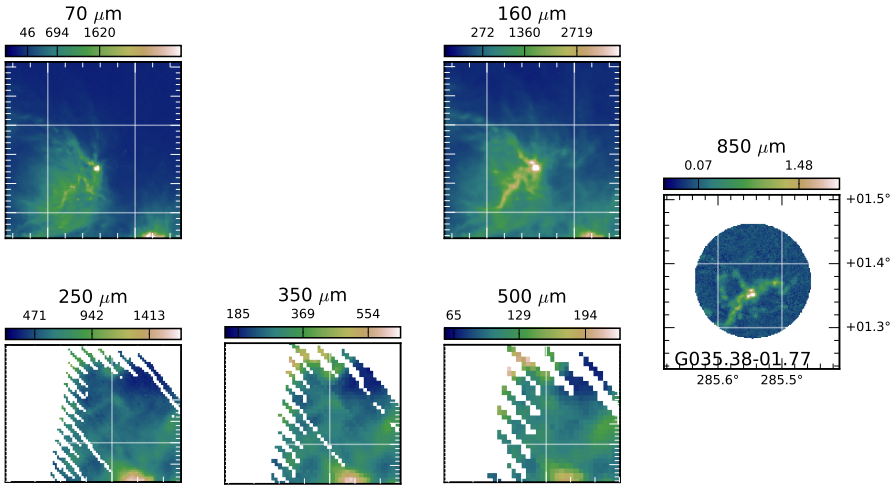
70 μm
46 694 1620
160 μm
272 1360 2719
850 μm
0.07 1.48
+01.5°
+01.4°
+01.3°
G035.38-01.77
285.6° 285.5°
250 μm
471 942 1413
350 μm
185 369 554
500 μm
65 129 194

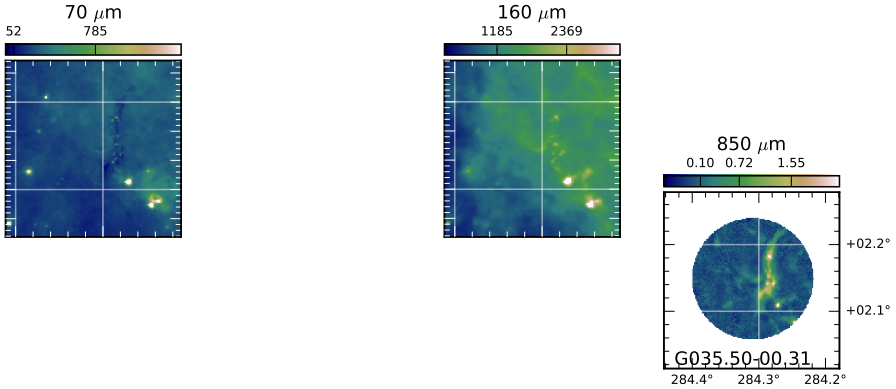
70 μm
52 785
160 μm
1185 2369
850 μm
0.10 0.72 1.55
+02.2°
+02.1°
G035.50-00.31
284.4° 284.3° 284.2°

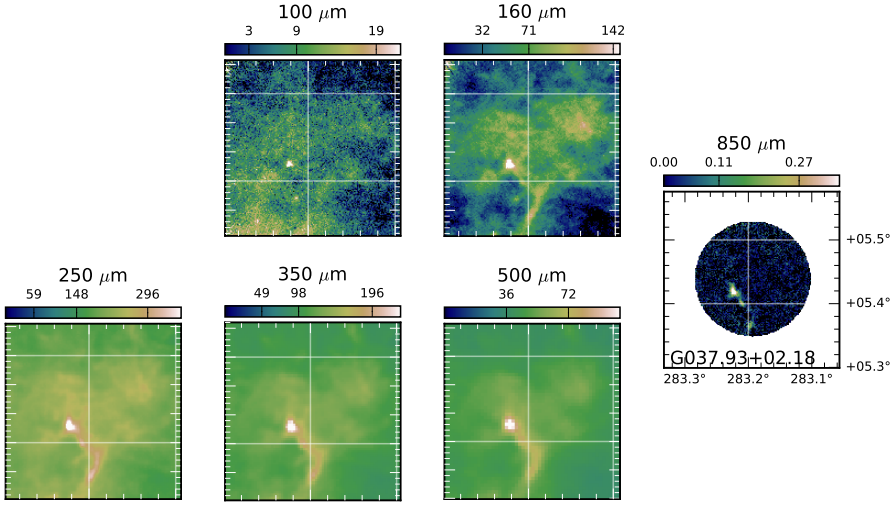
100 μm
3 9 19
160 μm
32 71 142
850 μm
0.00 0.11 0.27
250 μm
59 148 296
350 μm
49 98 196
500 μm
36 72
+05.5°
+05.4°
+05.3°
G037.93+02.18
283.3° 283.2° 283.1°

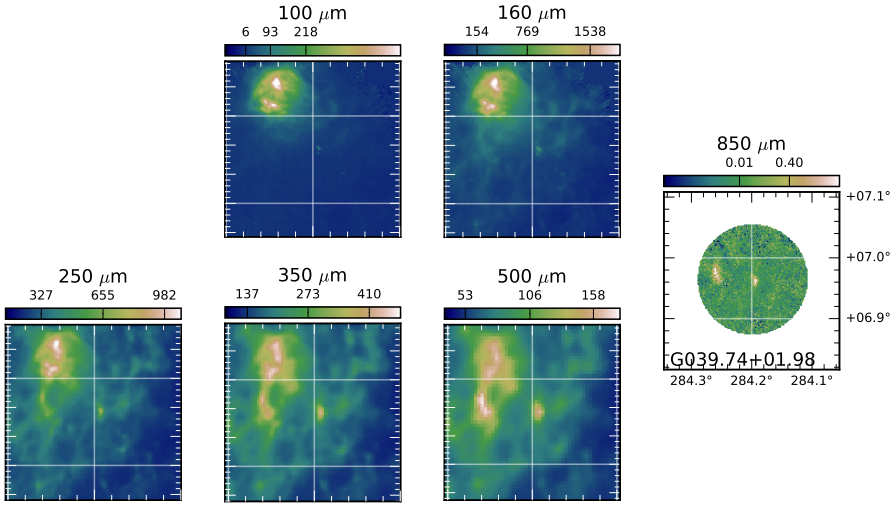
100 μm
6 93 218
160 μm
154 769 1538
850 μm
0.01 0.40
250 μm
327 655 982
350 μm
137 273 410
500 μm
53 106 158
+07.1°
+07.0°
+06.9°
G039.74+01.98
284.3° 284.2° 284.1°

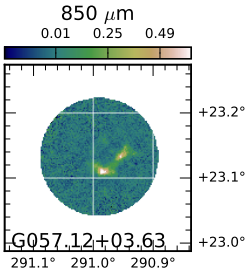
850 μm
0.01 0.25 0.49
+23.2°
+23.1°
+23.0°
G057.12+03.63
291.1° 291.0° 290.9°

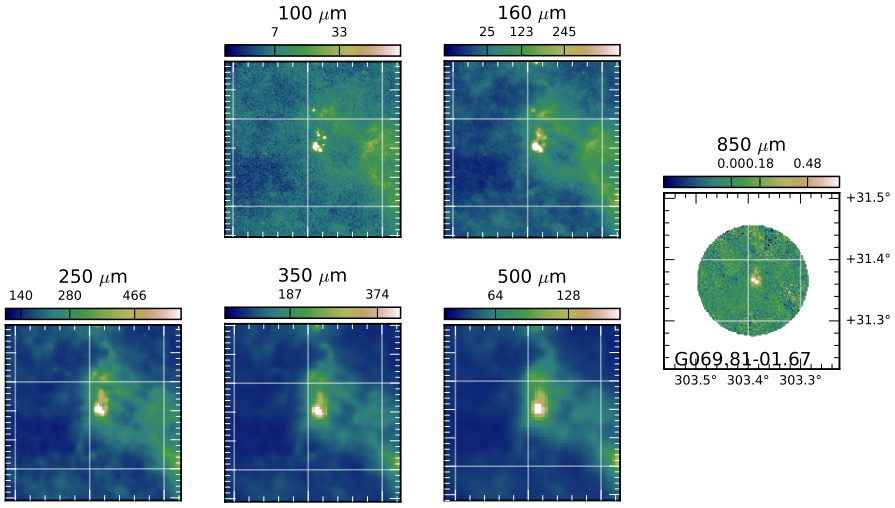
100 μm
7 33
160 μm
25 123 245
850 μm
0.000.18 0.48
+31.5°
+31.4°
+31.3°
G069.81-01.67
303.5° 303.4° 303.3°
250 μm
140 280 466
350 μm
187 374
500 μm
64 128

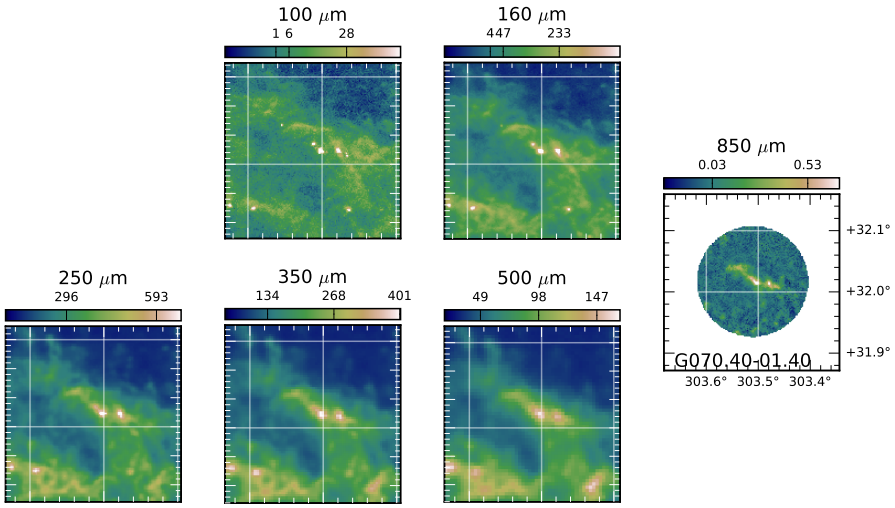
100 μm
1 6 28
160 μm
447 233
850 μm
0.03 0.53
+32.1°
+32.0°
+31.9°
G070.40-01.40
303.6° 303.5° 303.4°
250 μm
296 593
350 μm
134 268 401
500 μm
49 98 147

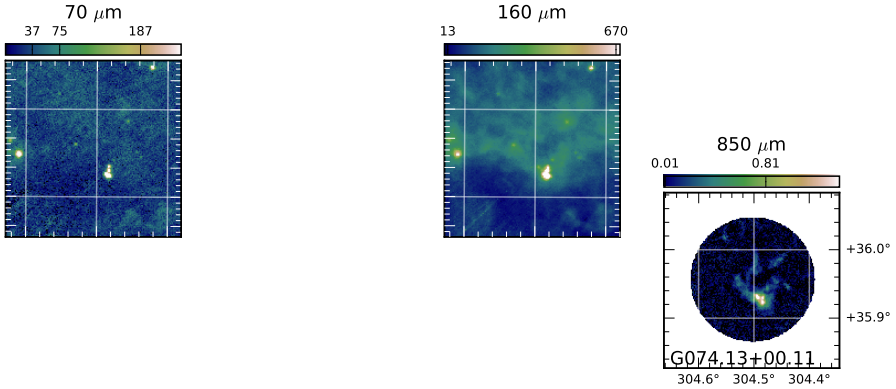
70 μm
37 75 187
160 μm
13 670
850 μm
0.01 0.81
+36.0°
+35.9°
G074.13+00.11
304.6° 304.5° 304.4°

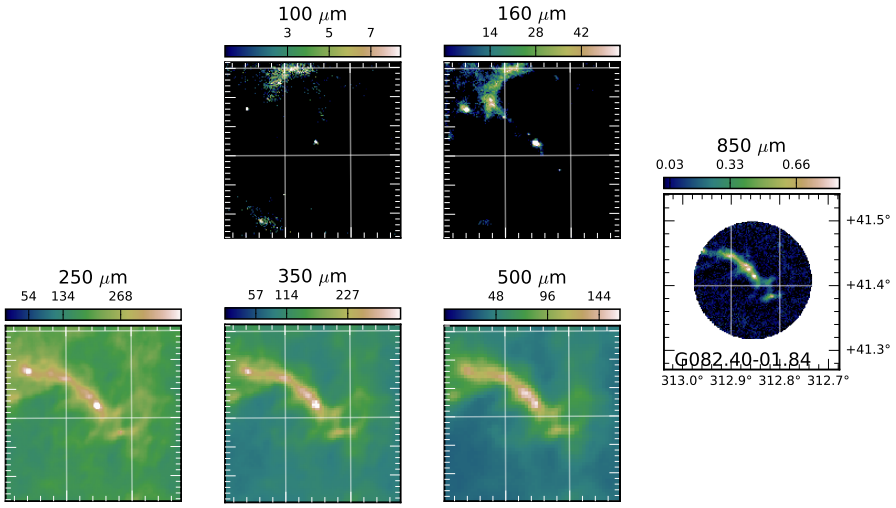
100 μm
3 5 7
160 μm
14 28 42
850 μm
0.03 0.33 0.66
250 μm
54 134 268
350 μm
57 114 227
500 μm
48 96 144
+41.5°
+41.4°
+41.3°
G082.40-01.84
313.0° 312.9° 312.8° 312.7°

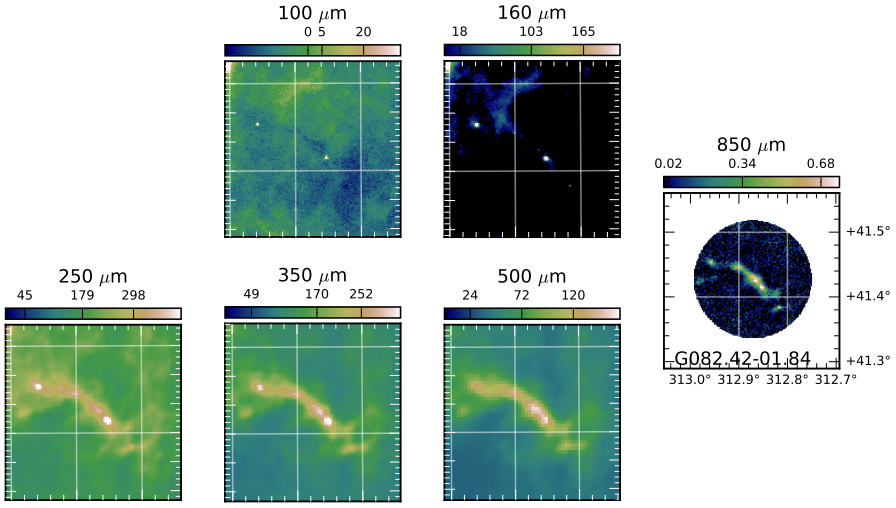
100 μm
0 5 20
160 μm
18 103 165
850 μm
0.02 0.34 0.68
250 μm
45 179 298
350 μm
49 170 252
500 μm
24 72 120
+41.5°
+41.4°
+41.3°
G082.42-01.84
313.0° 312.9° 312.8° 312.7°

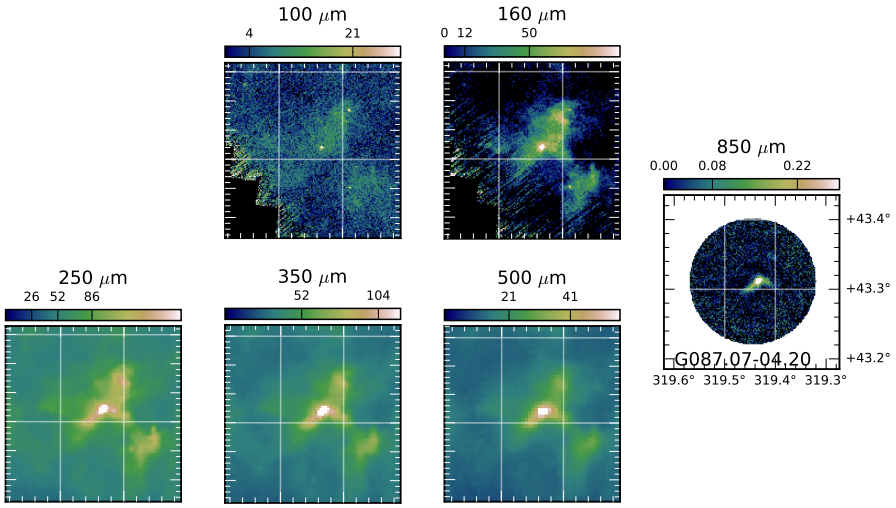
100 μm
4 21
160 μm
0 12 50
850 μm
0.00 0.08 0.22
250 μm
26 52 86
350 μm
52 104
500 μm
21 41
+43.4°
+43.3°
+43.2°
G087.07-04.20
319.6° 319.5° 319.4° 319.3°

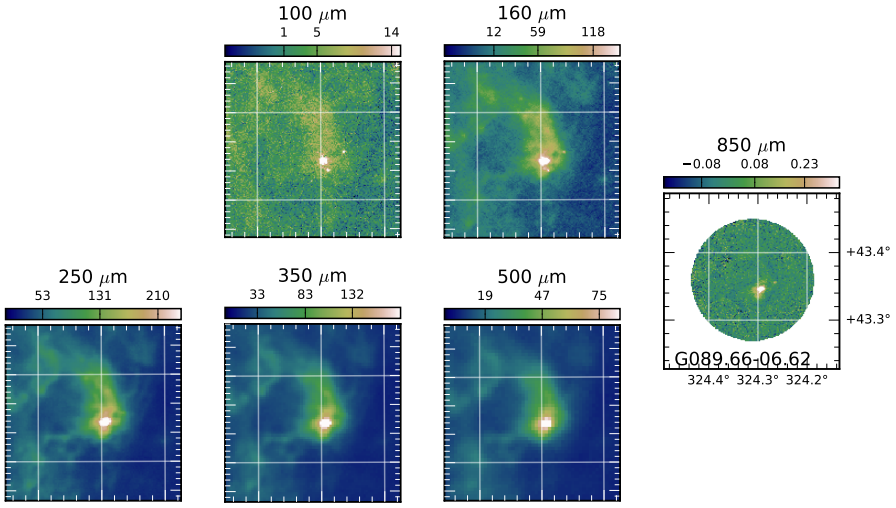
100 μm
1 5 14
160 μm
12 59 118
850 μm
−0.08 0.08 0.23
250 μm
53 131 210
350 μm
33 83 132
500 μm
19 47 75
+43.4°
+43.3°
G089.66-06.62
324.4° 324.3° 324.2°

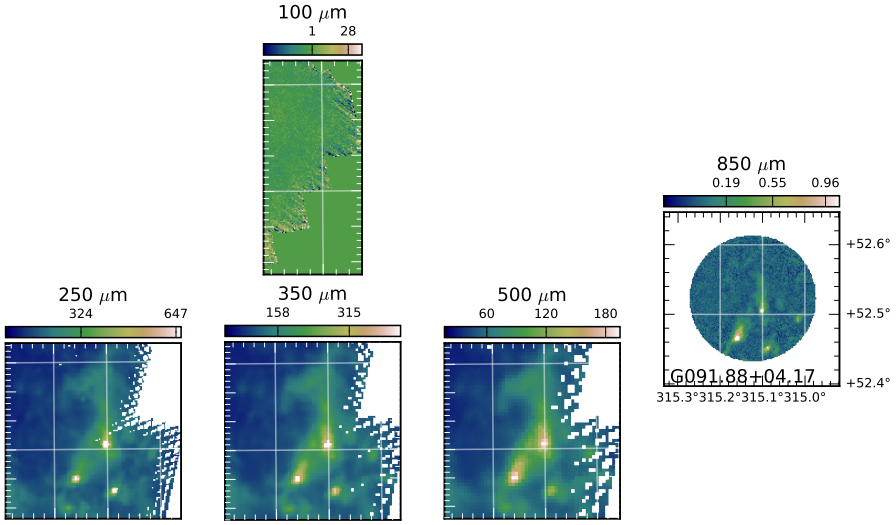
100 μm
1 28
850 μm
0.19 0.55 0.96
250 μm
324 647
350 μm
158 315
500 μm
60 120 180
+52.6°
+52.5°
+52.4°
G091.88+04.17
315.3°315.2°315.1°315.0°

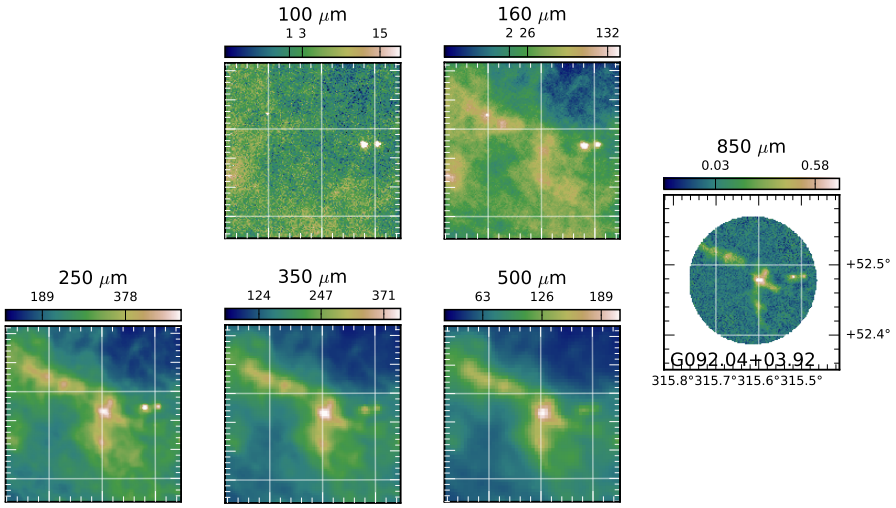
100 μm
1 3 15
160 μm
2 26 132
850 μm
0.03 0.58
250 μm
189 378
350 μm
124 247 371
500 μm
63 126 189
+52.5°
+52.4°
G092.04+03.92
315.8°315.7°315.6°315.5°

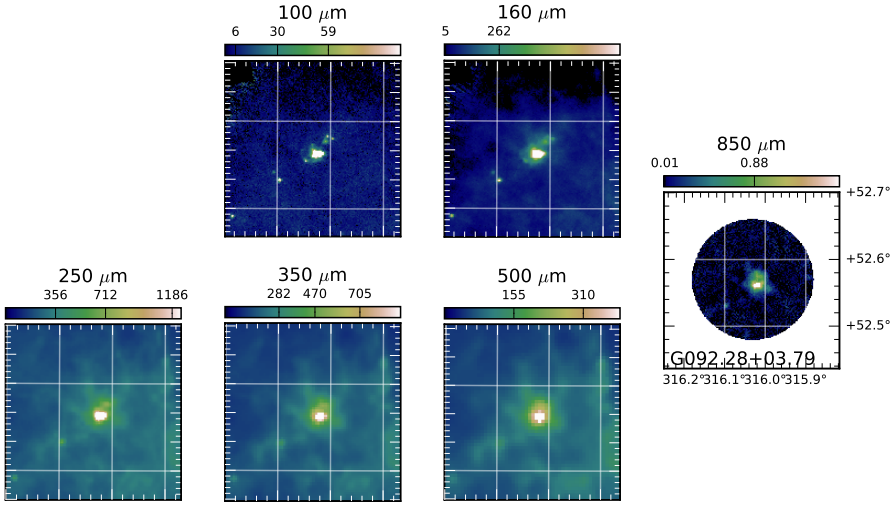
100 μm
6 30 59
160 μm
5 262
850 μm
0.01 0.88
250 μm
356 712 1186
350 μm
282 470 705
500 μm
155 310
+52.7°
+52.6°
+52.5°
G092.28+03.79
316.2°316.1°316.0°315.9°

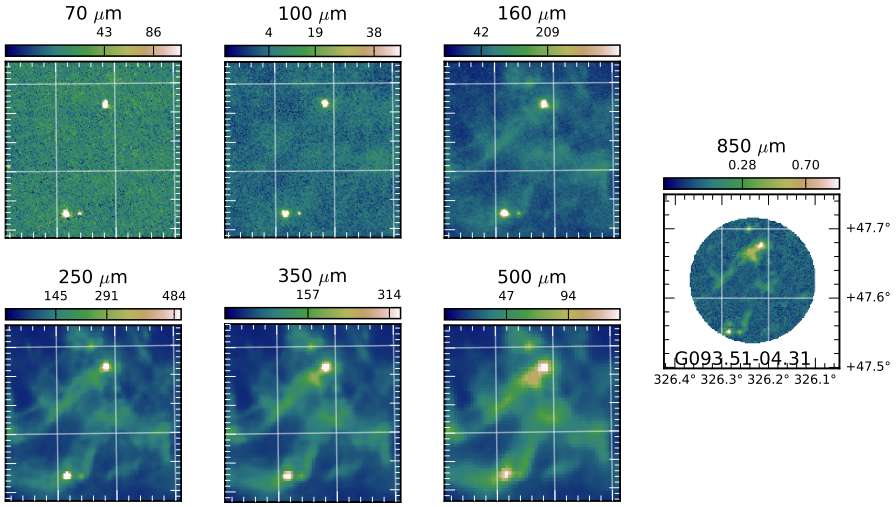
70 μm
43 86
100 μm
4 19 38
160 μm
42 209
850 μm
0.28 0.70
250 μm
145 291 484
350 μm
157 314
500 μm
47 94
+47.7°
+47.6°
+47.5°
G093.51-04.31
326.4° 326.3° 326.2° 326.1°

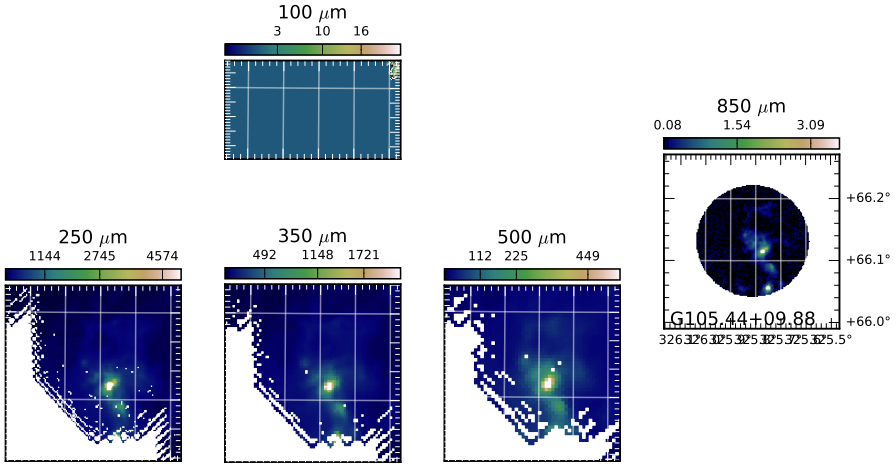
100 μm
3 10 16
850 μm
0.08 1.54 3.09
250 μm
1144 2745 4574
350 μm
492 1148 1721
500 μm
112 225 449
+66.2°
+66.1°
+66.0°
G105.44+09.88

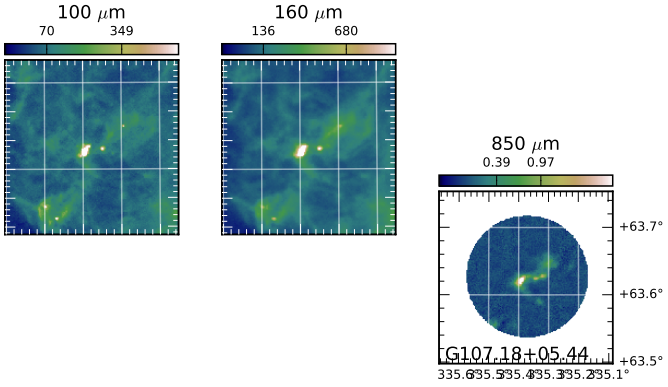
100 μm
70 349
160 μm
136 680
850 μm
0.39 0.97
+63.7°
+63.6°
+63.5°
G107.18+05.44

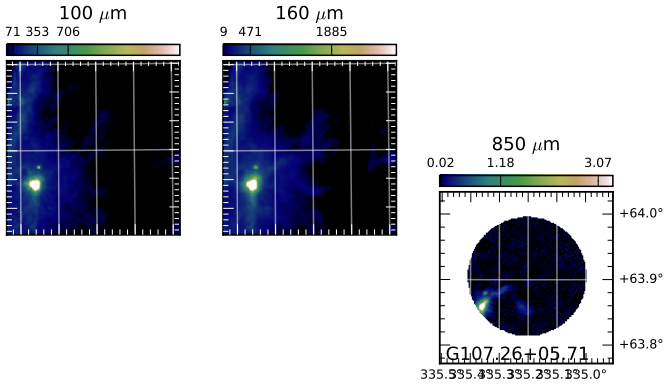
100 μm
71 353 706
160 μm
9 471 1885
850 μm
0.02 1.18 3.07
+64.0°
+63.9°
+63.8°
G107.26+05.71

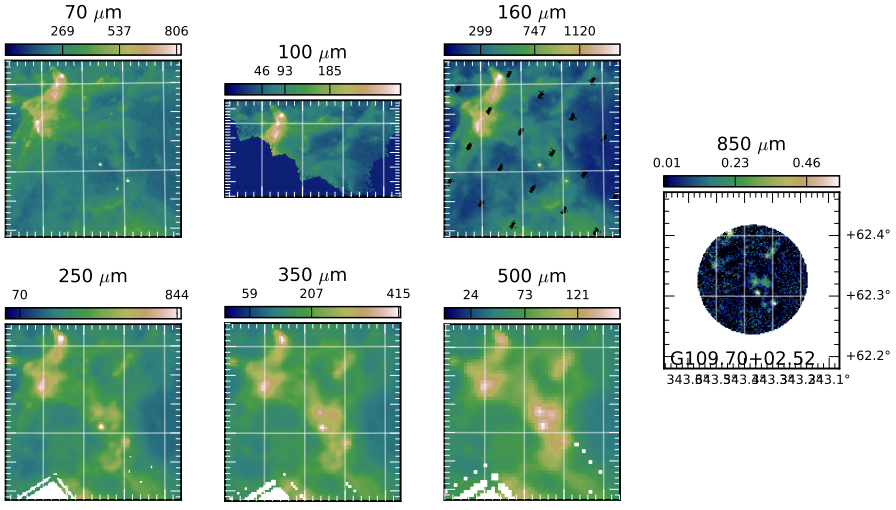
70 μm
269 537 806
100 μm
46 93 185
160 μm
299 747 1120
850 μm
0.01 0.23 0.46
250 μm
70 844
350 μm
59 207 415
500 μm
24 73 121
+62.4°
+62.3°
+62.2°
G109.70+02.52
343.1°

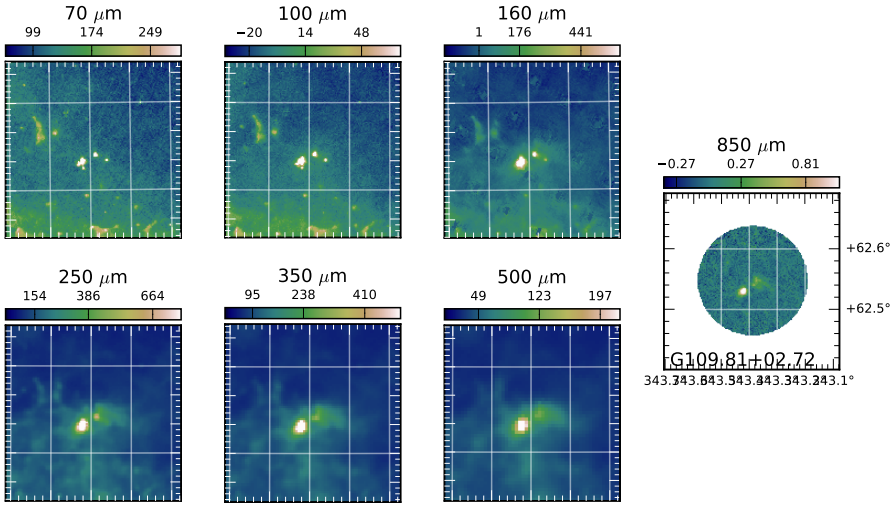
70 μm
99 174 249
100 μm
−20 14 48
160 μm
1 176 441
850 μm
−0.27 0.27 0.81
250 μm
154 386 664
350 μm
95 238 410
500 μm
49 123 197
+62.6°
+62.5°
G109.81+02.72
343.1°

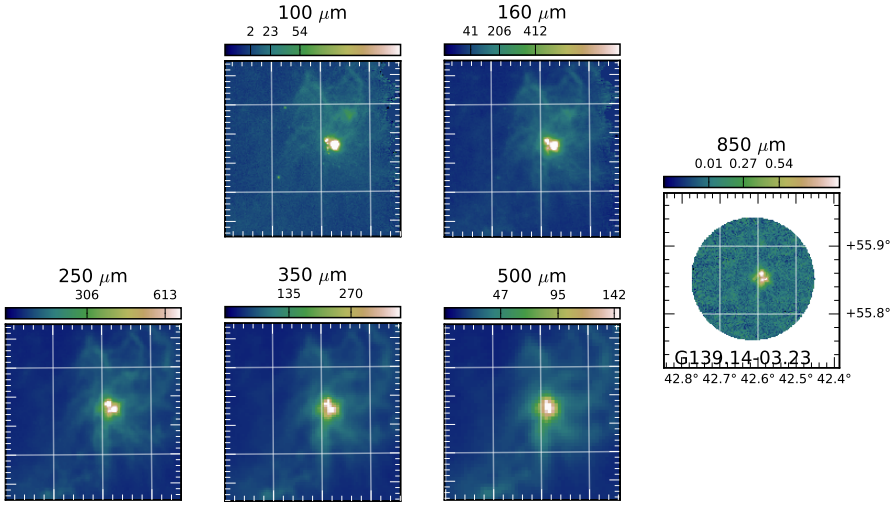
100 μm
2 23 54
160 μm
41 206 412
850 μm
0.01 0.27 0.54
250 μm
306 613
350 μm
135 270
500 μm
47 95 142
+55.9°
+55.8°
G139.14-03.23
42.8° 42.7° 42.6° 42.5° 42.4°

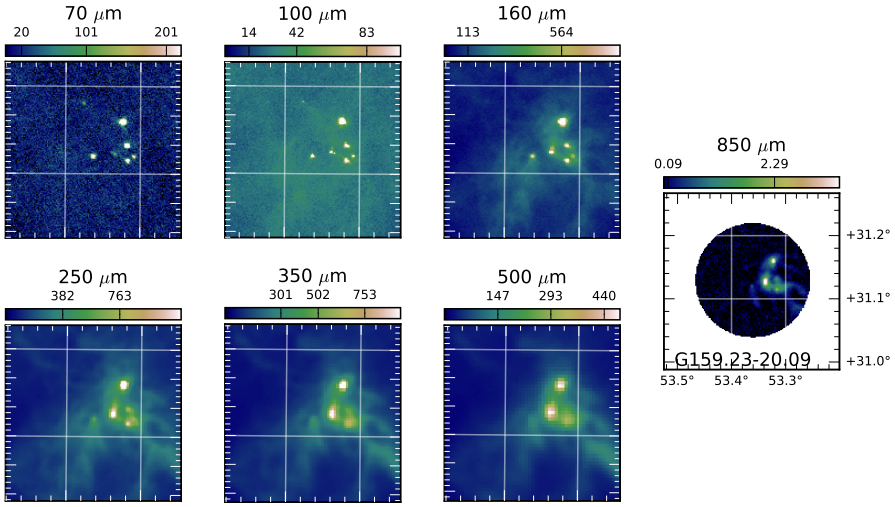
70 μm
20 101 201
100 μm
14 42 83
160 μm
113 564
850 μm
0.09 2.29
250 μm
382 763
350 μm
301 502 753
500 μm
147 293 440
+31.2°
+31.1°
+31.0°
G159.23-20.09
53.5° 53.4° 53.3°

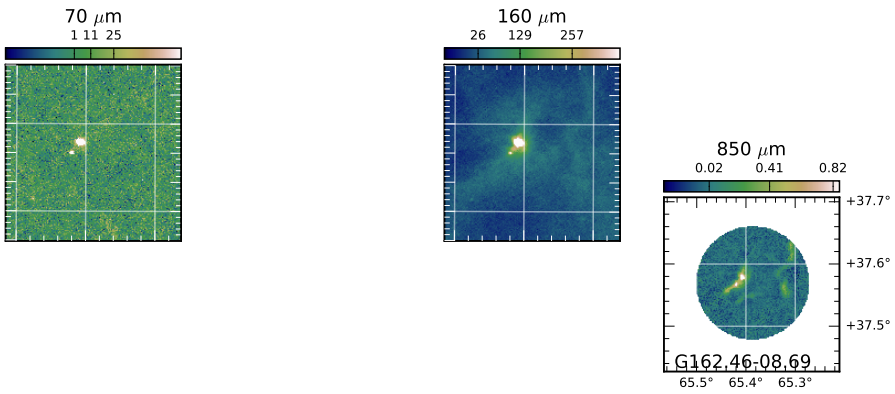
70 μm
1 11 25
160 μm
26 129 257
850 μm
0.02 0.41 0.82
+37.7°
+37.6°
+37.5°
G162.46-08.69
65.5° 65.4° 65.3°

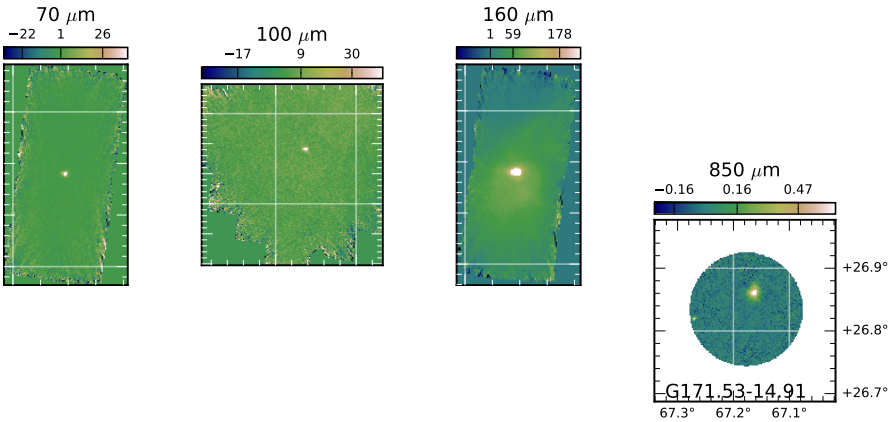
70 μm
−22 1 26
100 μm
−17 9 30
160 μm
1 59 178
850 μm
−0.16 0.16 0.47
+26.9°
+26.8°
+26.7°
G171.53-14.91
67.3° 67.2° 67.1°

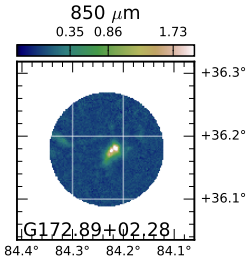
850 μm
0.35 0.86 1.73
+36.3°
+36.2°
+36.1°
G172.89+02.28
84.4° 84.3° 84.2° 84.1°

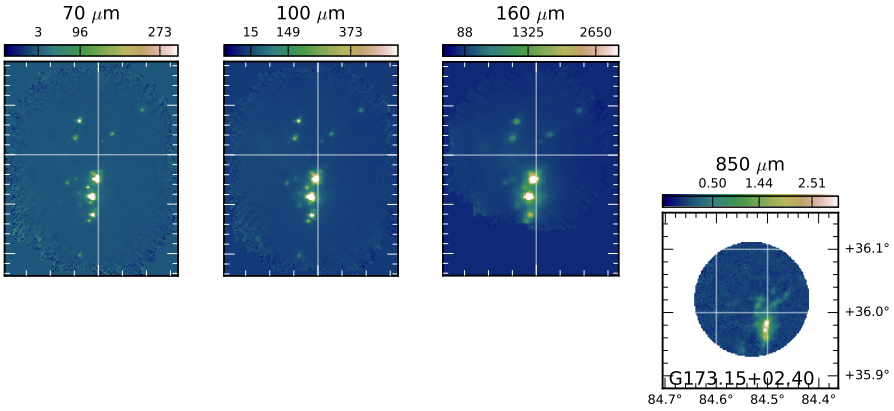
70 μm
3 96 273
100 μm
15 149 373
160 μm
88 1325 2650
850 μm
0.50 1.44 2.51
+36.1°
+36.0°
+35.9°
G173.15+02.40
84.7° 84.6° 84.5° 84.4°

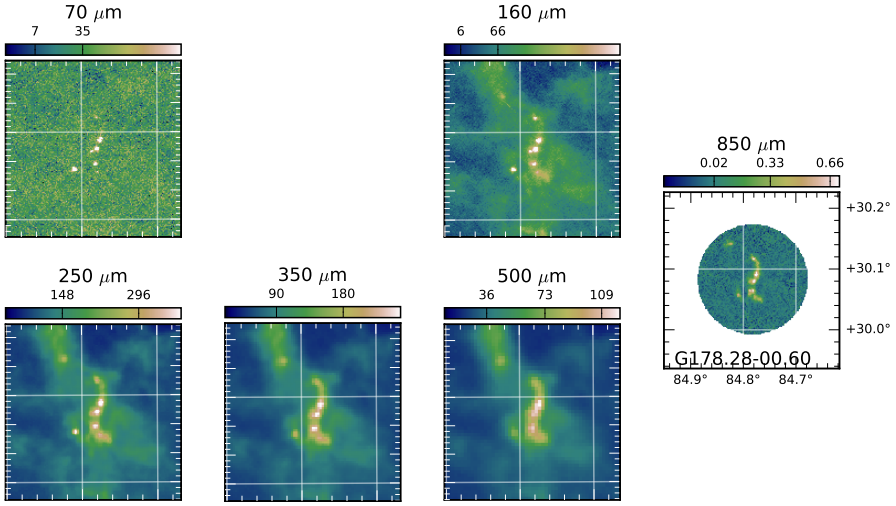
70 μm
7 35
160 μm
6 66
850 μm
0.02 0.33 0.66
250 μm
148 296
350 μm
90 180
500 μm
36 73 109
+30.2°
+30.1°
+30.0°
G178.28-00.60
84.9° 84.8° 84.7°

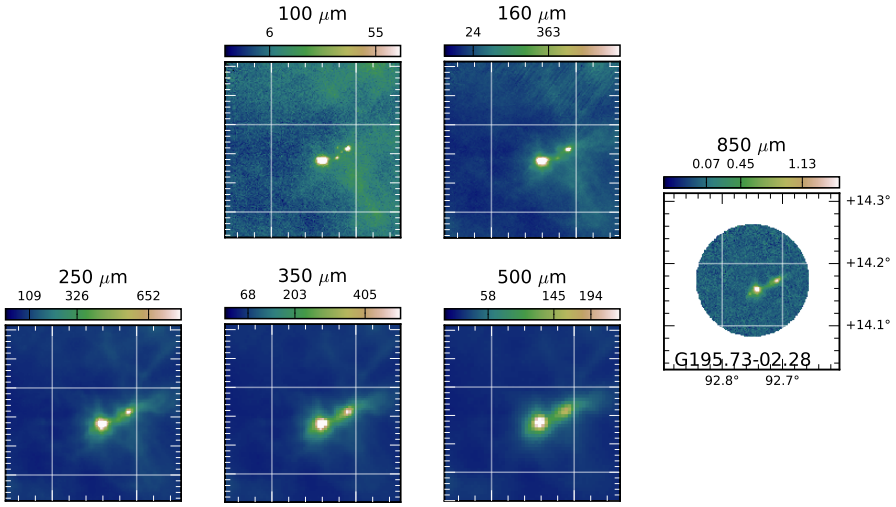
100 μm
6 55
160 μm
24 363
850 μm
0.07 0.45 1.13
250 μm
109 326 652
350 μm
68 203 405
500 μm
58 145 194
+14.3°
+14.2°
+14.1°
G195.73-02.28
92.8° 92.7°

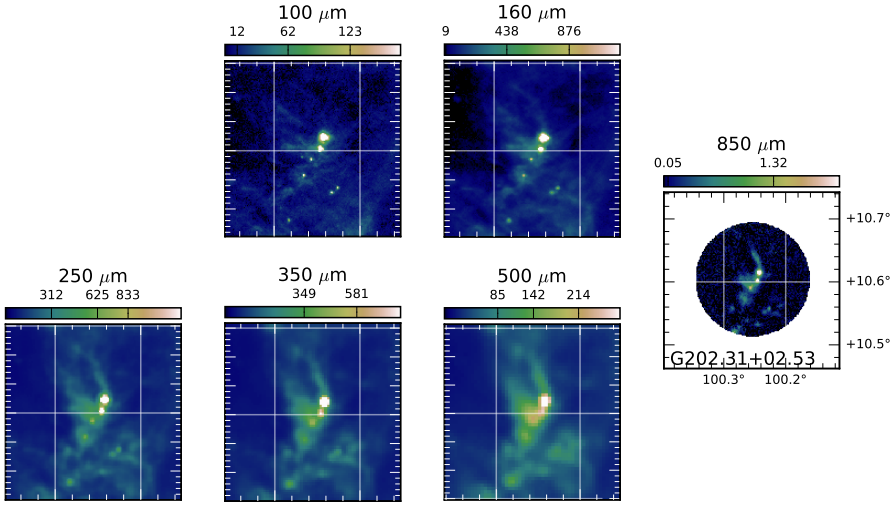
100 μm
12 62 123
160 μm
9 438 876
850 μm
0.05 1.32
250 μm
312 625 833
350 μm
349 581
500 μm
85 142 214
+10.7°
+10.6°
+10.5°
G202.31+02.53
100.3° 100.2°

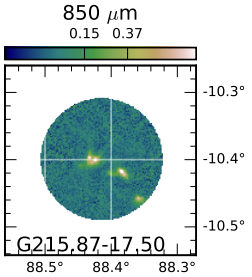
850 μm
0.15 0.37
-10.3°
-10.4°
-10.5°
G215.87-17.50
88.5° 88.4° 88.3°

C.2 Column density maps with 850-μm intensity contours

The following figures show the column density maps of the observed fields with SPIRE data. The SCUBA-2 850-μm surface brightness distribution is drawn with white contours. Column densities $N(H_2)$ are plotted in units of cm^{-2}, with exponent written in the top right corner. SCUBA-2 contours are at 20% intervals relative to the peak intensity starting from 40%.

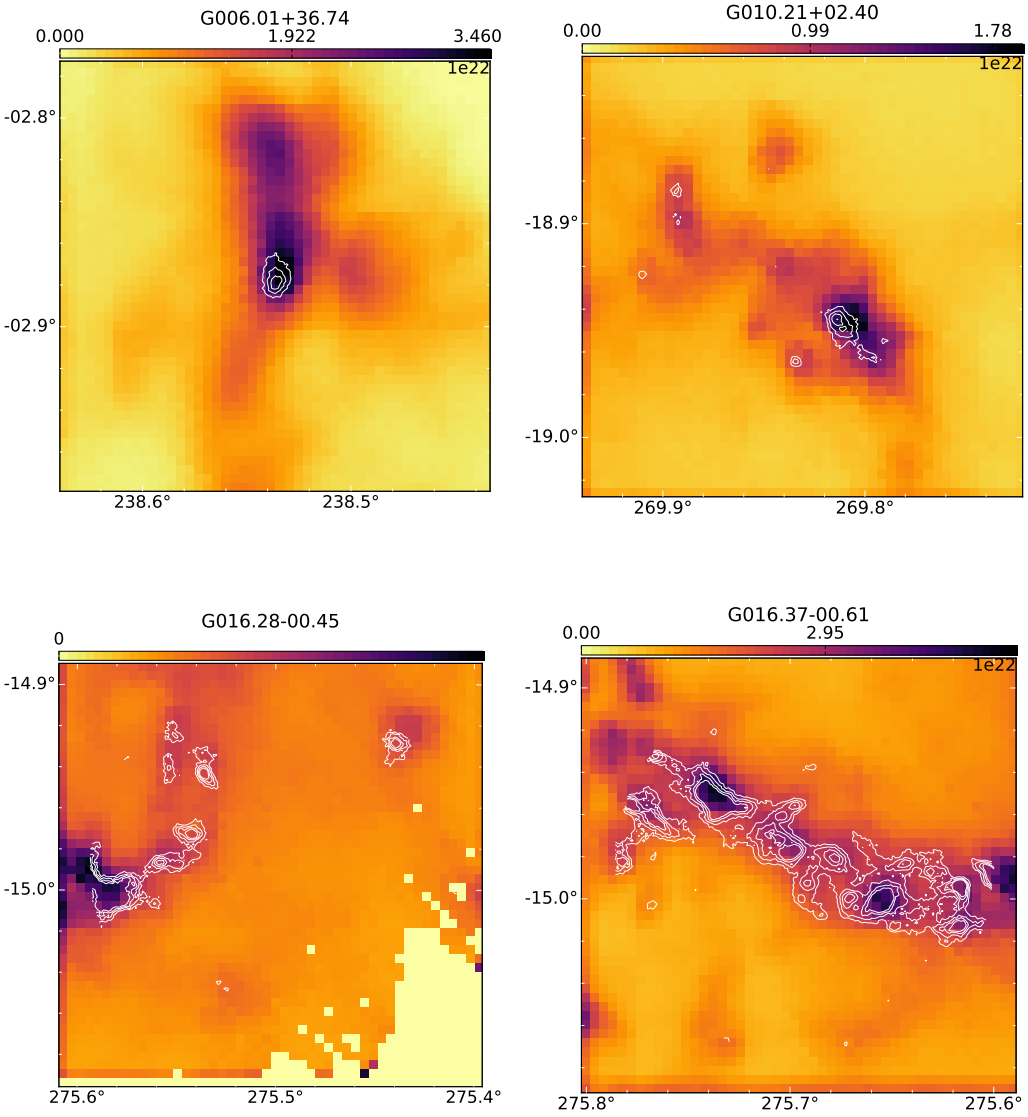

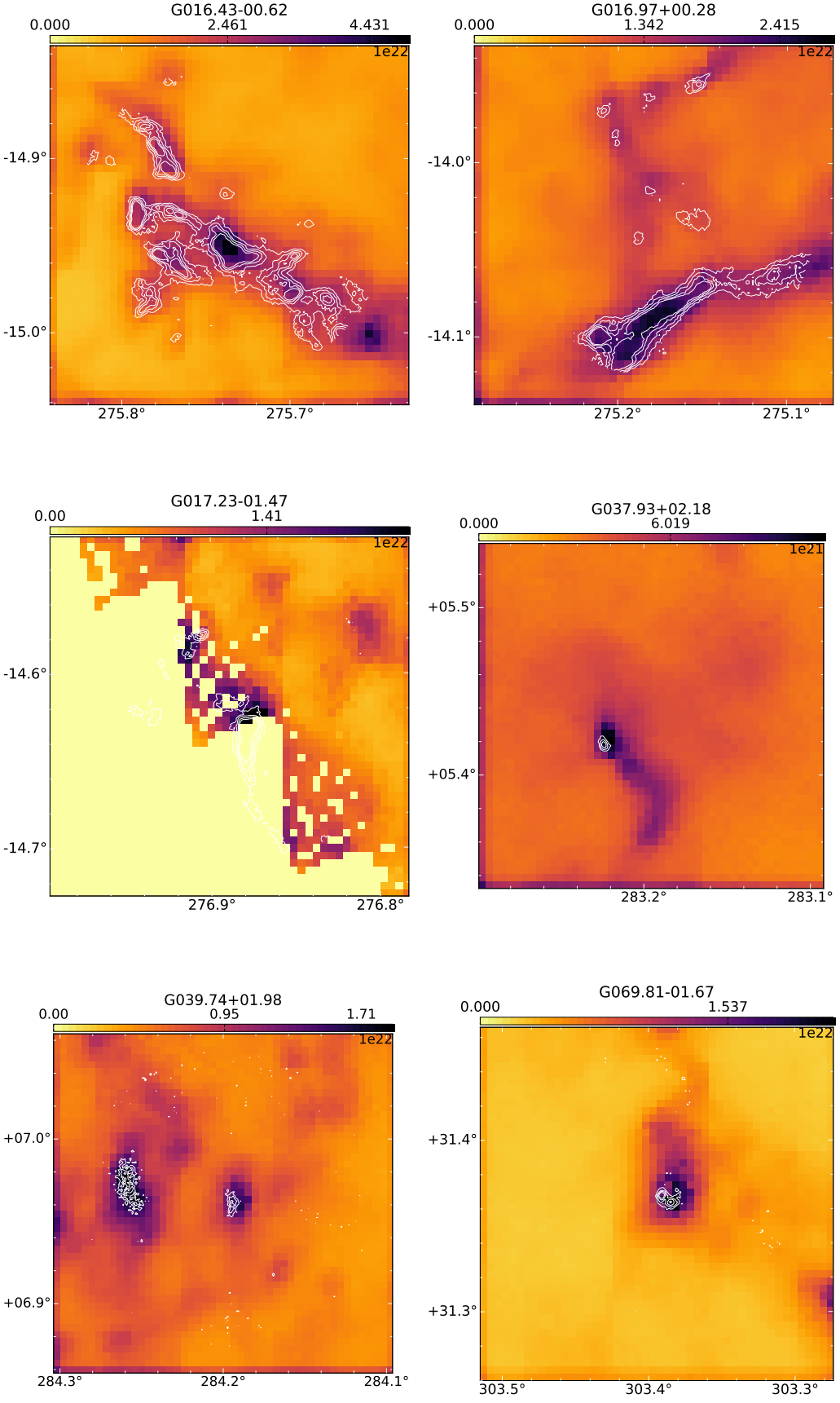
G016.43-00.62
0.000
2.461
4.431
1e22
-14.9°
-15.0°
275.8°
275.7°
G016.97+00.28
0.000
1.342
2.415
1e22
-14.0°
-14.1°
275.2°
275.1°
G017.23-01.47
0.00
1.41
1e22
-14.6°
-14.7°
276.9°
276.8°
G037.93+02.18
0.000
6.019
1e21
+05.5°
+05.4°
283.2°
283.1°
G039.74+01.98
0.00
0.95
1.71
1e22
+07.0°
+06.9°
284.3°
284.2°
284.1°
G069.81-01.67
0.000
1.537
1e22
+31.4°
+31.3°
303.5°
303.4°
303.3°

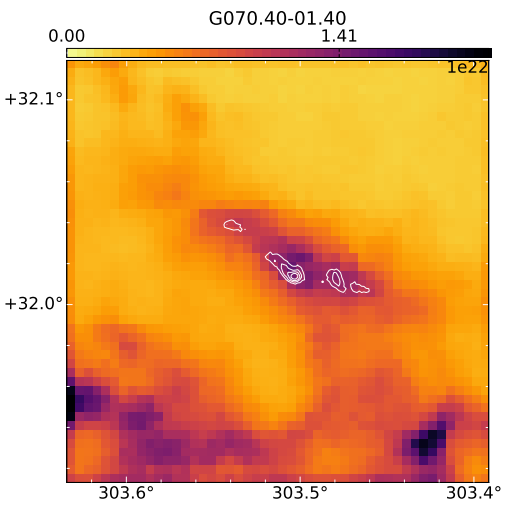
G070.40-01.40
0.00
1.41
1e22
+32.1°
+32.0°
303.6°
303.5°
303.4°

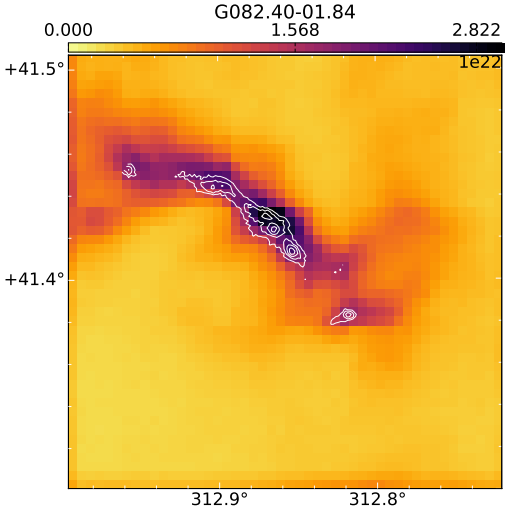
G082.40-01.84
0.000
1.568
2.822
1e22
+41.5°
+41.4°
312.9°
312.8°

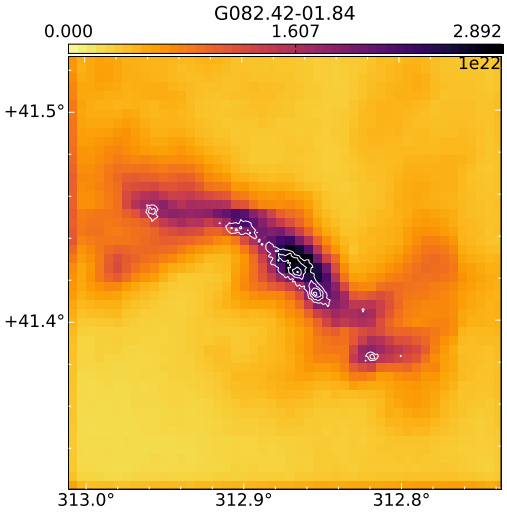
G082.42-01.84
0.000
1.607
2.892
1e22
+41.5°
+41.4°
313.0°
312.9°
312.8°

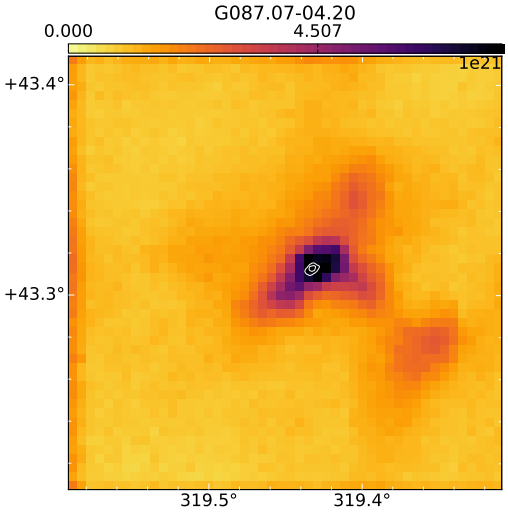
G087.07-04.20
0.000
4.507
1e21
+43.4°
+43.3°
319.5°
319.4°

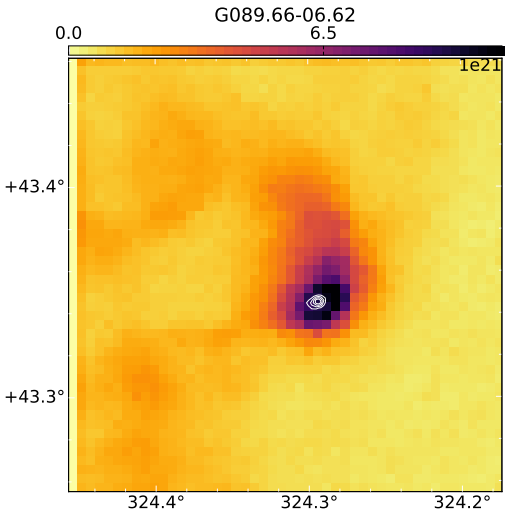
G089.66-06.62
0.0
6.5
1e21
+43.4°
+43.3°
324.4°
324.3°
324.2°

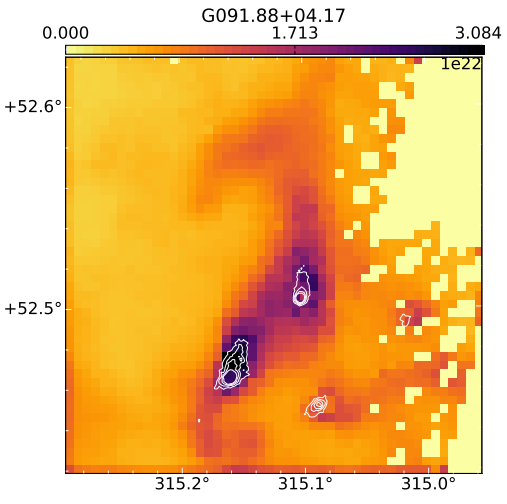
G091.88+04.17
0.000
1.713
3.084
1e22
+52.6°
+52.5°
315.2°
315.1°
315.0°

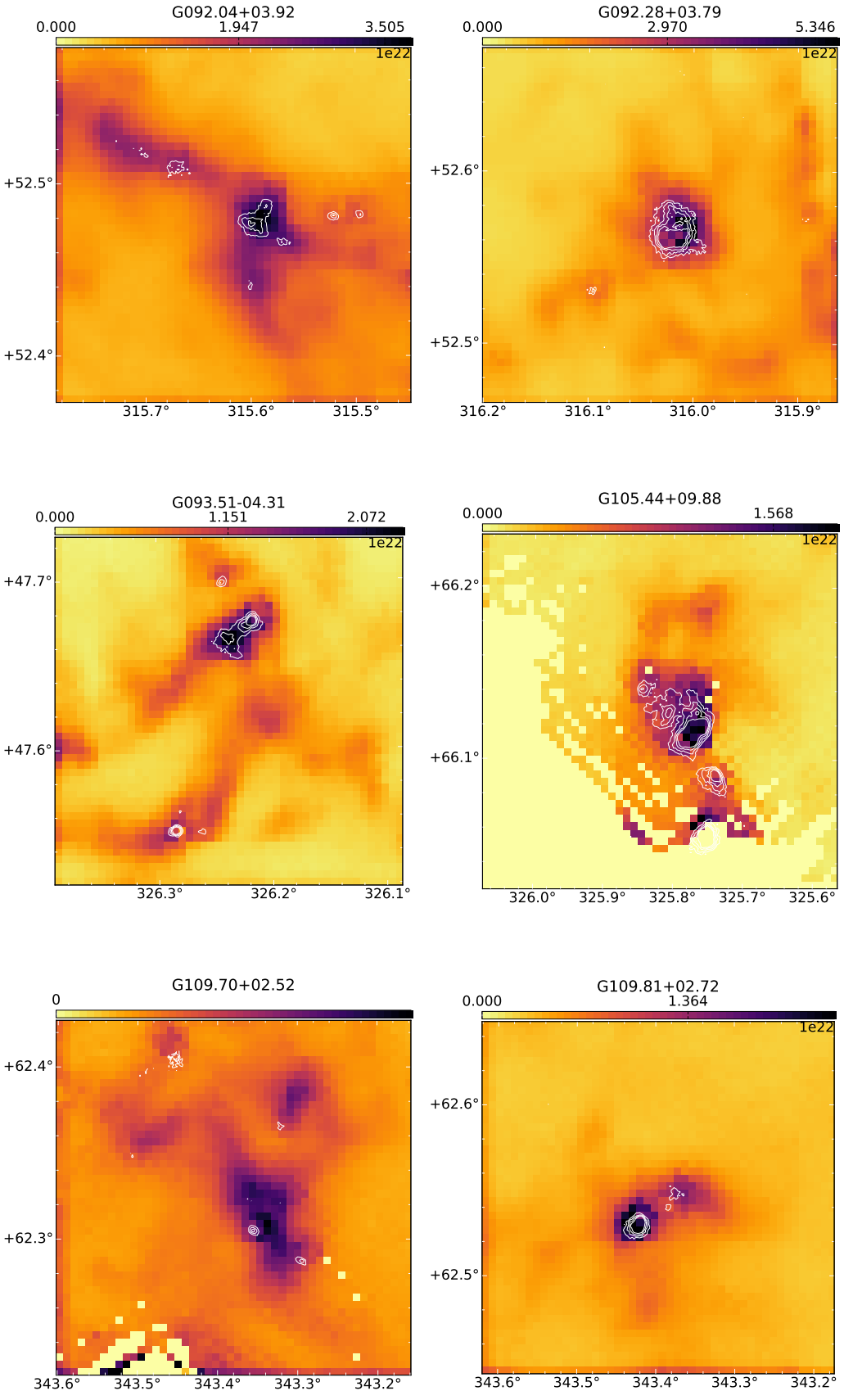
G092.04+03.92
0.000
1.947
3.505
1e22
+52.5°
+52.4°
315.7°
315.6°
315.5°
G092.28+03.79
0.000
2.970
5.346
1e22
+52.6°
+52.5°
316.2°
316.1°
316.0°
315.9°
G093.51-04.31
0.000
1.151
2.072
1e22
+47.7°
+47.6°
326.3°
326.2°
326.1°
G105.44+09.88
0.000
1.568
1e22
+66.2°
+66.1°
326.0°
325.9°
325.8°
325.7°
325.6°
G109.70+02.52
0
+62.4°
+62.3°
343.6°
343.5°
343.4°
343.3°
343.2°
G109.81+02.72
0.000
1.364
1e22
+62.6°
+62.5°
343.6°
343.5°
343.4°
343.3°
343.2°

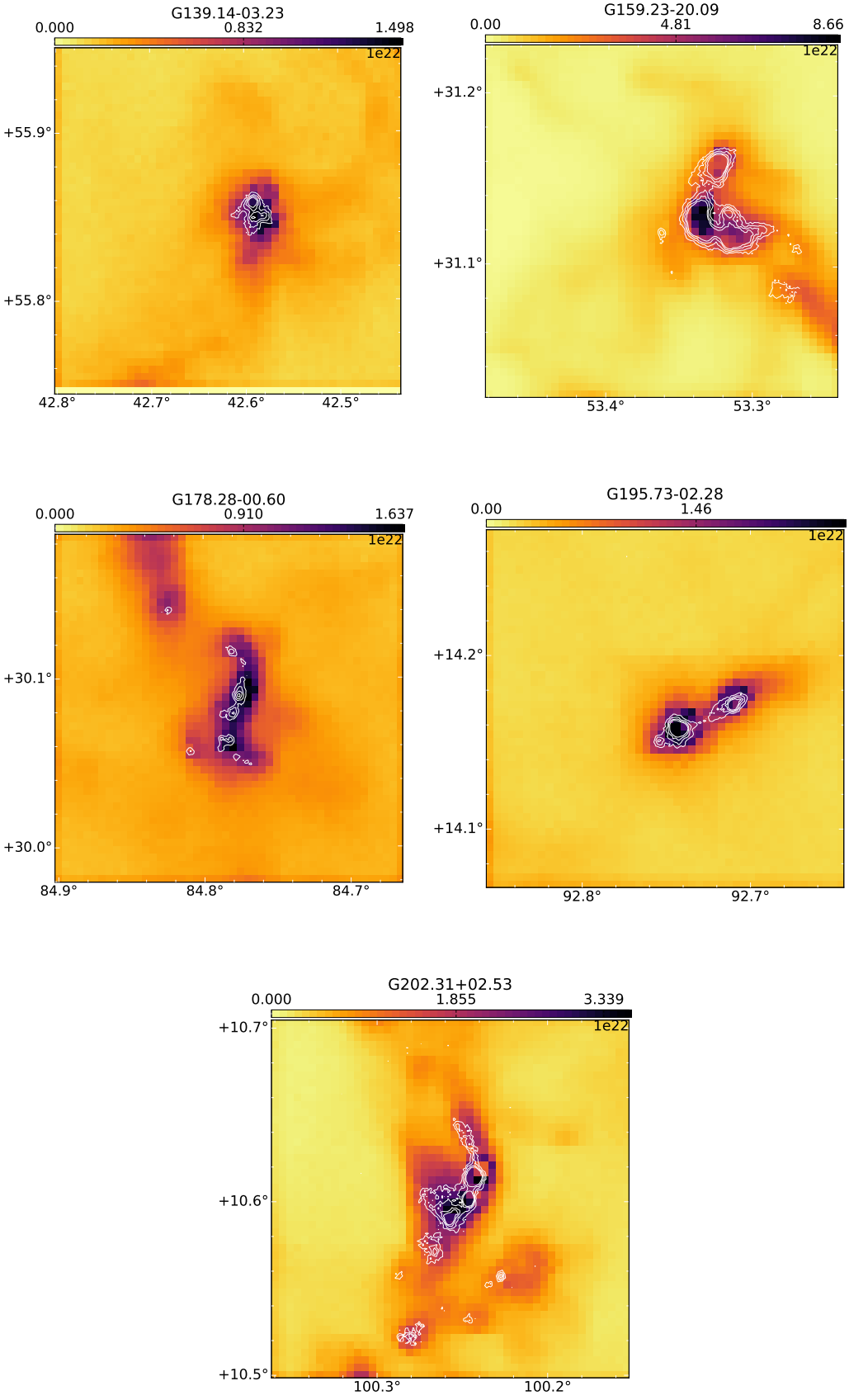
G139.14-03.23
0.000
0.832
1.498
1e22
+55.9°
+55.8°
42.8°
42.7°
42.6°
42.5°
G159.23-20.09
0.00
4.81
8.66
1e22
+31.2°
+31.1°
53.4°
53.3°
G178.28-00.60
0.000
0.910
1.637
1e22
+30.1°
+30.0°
84.9°
84.8°
84.7°
G195.73-02.28
0.00
1.46
1e22
+14.2°
+14.1°
92.8°
92.7°
G202.31+02.53
0.000
1.855
3.339
1e22
+10.7°
+10.6°
+10.5°
100.3°
100.2°

C.3 YSOs and clumps on 850-μm intensity maps

Surface brightness maps of the SCUBA-2 850-μm intensity, with units of mJy/arcsec^2. Outlines of the clumps found by `Fellwalker` are plotted with white contours. White circles show the locations of the YSOs located on the clumps. Field YSOs are not plotted and no distinction is made between YSOs from different catalogs. The coordinates are presented in degrees in Equatorial J2000 coordinates. The field names are written on top of the colorbar.

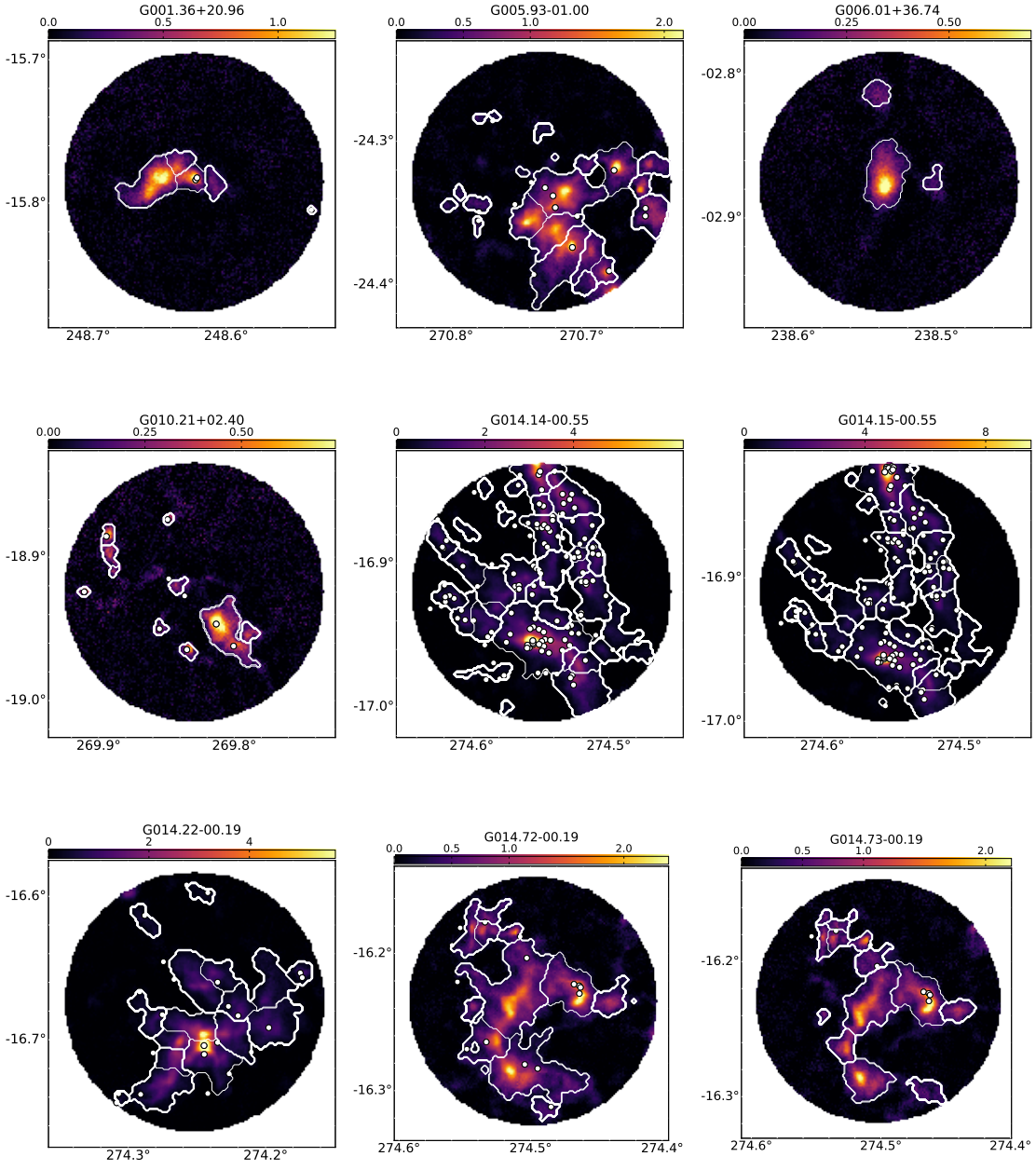

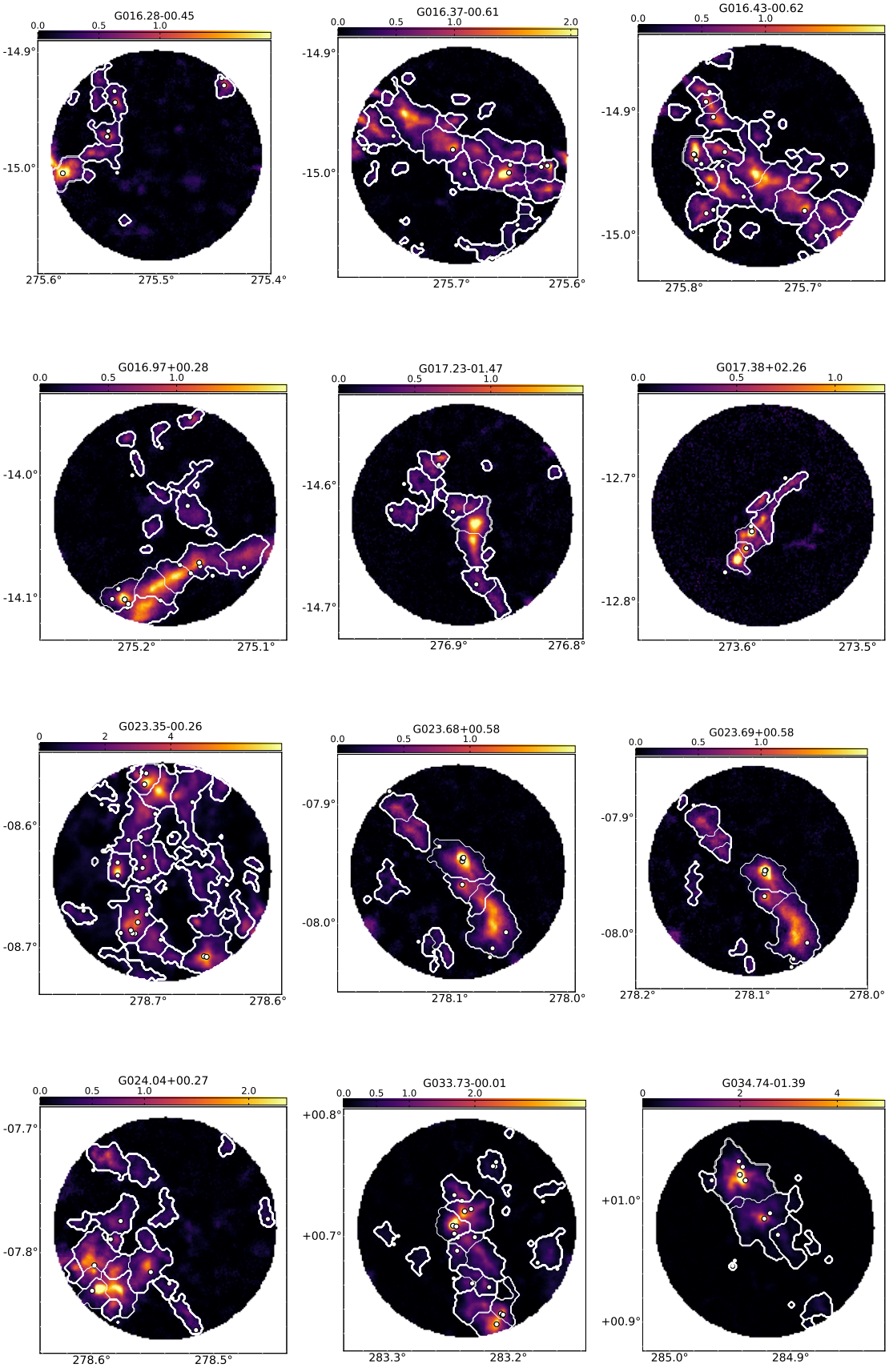
G016.28-00.45
0.0 0.5 1.0
-14.9°
-15.0°
275.6° 275.5° 275.4°
G016.37-00.61
0.0 0.5 1.0 2.0
-14.9°
-15.0°
275.7° 275.6°
G016.43-00.62
0.0 0.5 1.0
-14.9°
-15.0°
275.8° 275.7°
G016.97+00.28
0.0 0.5 1.0
-14.0°
-14.1°
275.2° 275.1°
G017.23-01.47
0.0 0.5 1.0
-14.6°
-14.7°
276.9° 276.8°
G017.38+02.26
0.0 0.5 1.0
-12.7°
-12.8°
273.6° 273.5°
G023.35-00.26
0 2 4
-08.6°
-08.7°
278.7° 278.6°
G023.68+00.58
0.0 0.5 1.0
-07.9°
-08.0°
278.1° 278.0°
G023.69+00.58
0.0 0.5 1.0
-07.9°
-08.0°
278.2° 278.1° 278.0°
G024.04+00.27
0.0 0.5 1.0 2.0
-07.7°
-07.8°
278.6° 278.5°
G033.73-00.01
0.0 0.5 1.0 2.0
+00.8°
+00.7°
283.3° 283.2°
G034.74-01.39
0 2 4
+01.0°
+00.9°
285.0° 284.9°

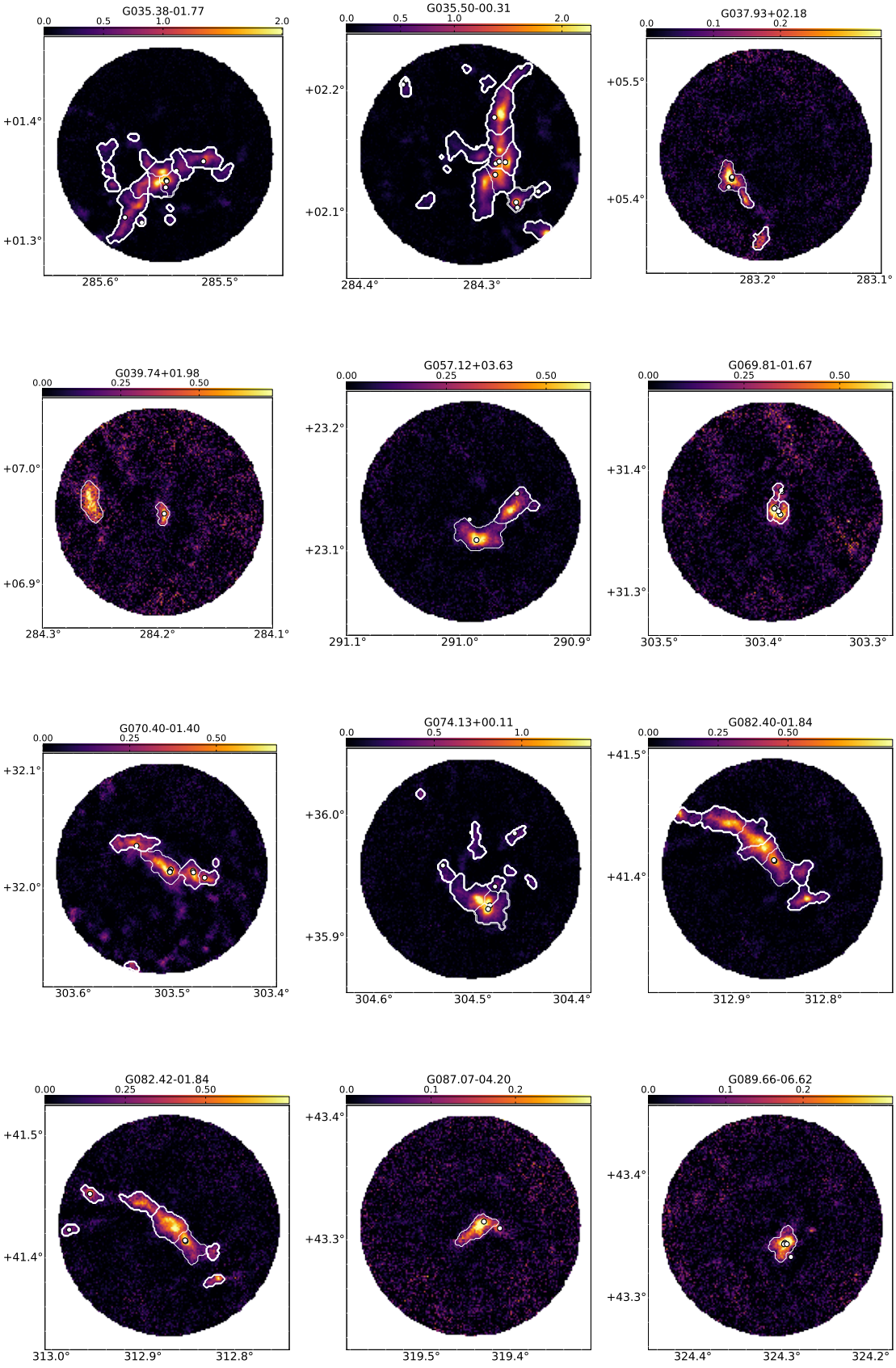
G035.38-01.77
0.0 0.5 1.0 2.0
+01.4°
+01.3°
285.6° 285.5°
G035.50-00.31
0.0 0.5 1.0 2.0
+02.2°
+02.1°
284.4° 284.3°
G037.93+02.18
0.0 0.1 0.2
+05.5°
+05.4°
283.2° 283.1°
G039.74+01.98
0.00 0.25 0.50
+07.0°
+06.9°
284.3° 284.2° 284.1°
G057.12+03.63
0.00 0.25 0.50
+23.2°
+23.1°
291.1° 291.0° 290.9°
G069.81-01.67
0.00 0.25 0.50
+31.4°
+31.3°
303.5° 303.4° 303.3°
G070.40-01.40
0.00 0.25 0.50
+32.1°
+32.0°
303.6° 303.5° 303.4°
G074.13+00.11
0.0 0.5 1.0
+36.0°
+35.9°
304.6° 304.5° 304.4°
G082.40-01.84
0.00 0.25 0.50
+41.5°
+41.4°
312.9° 312.8°
G082.42-01.84
0.00 0.25 0.50
+41.5°
+41.4°
313.0° 312.9° 312.8°
G087.07-04.20
0.0 0.1 0.2
+43.4°
+43.3°
319.5° 319.4°
G089.66-06.62
0.0 0.1 0.2
+43.4°
+43.3°
324.4° 324.3° 324.2°

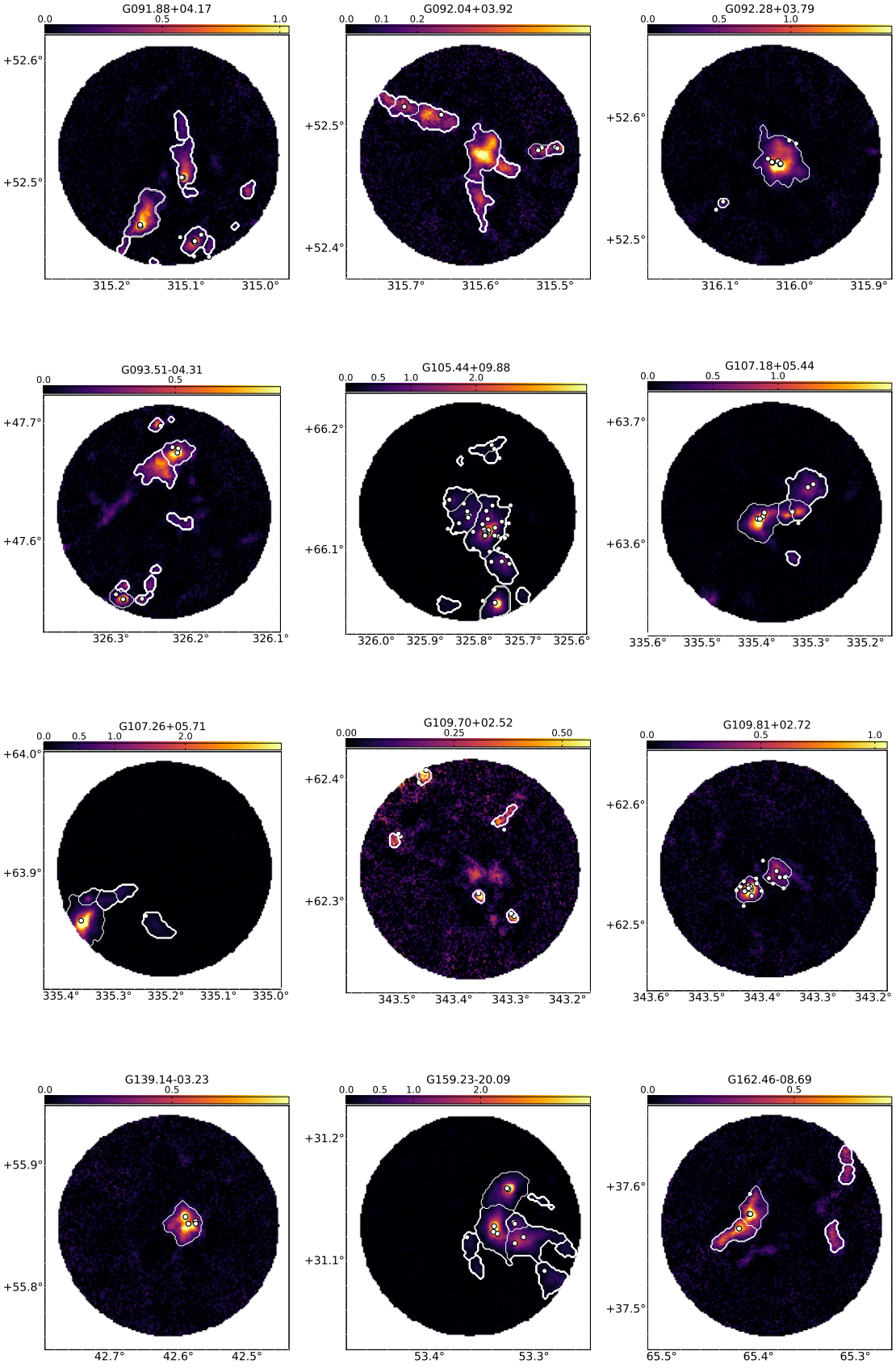
G091.88+04.17
0.0 0.5 1.0
+52.6°
+52.5°
315.2° 315.1° 315.0°
G092.04+03.92
0.0 0.1 0.2
+52.5°
+52.4°
315.7° 315.6° 315.5°
G092.28+03.79
0.0 0.5 1.0
+52.6°
+52.5°
316.1° 316.0° 315.9°
G093.51-04.31
0.0 0.5
+47.7°
+47.6°
326.3° 326.2° 326.1°
G105.44+09.88
0.0 0.5 1.0 2.0
+66.2°
+66.1°
326.0° 325.9° 325.8° 325.7° 325.6°
G107.18+05.44
0.0 0.5 1.0
+63.7°
+63.6°
335.6° 335.5° 335.4° 335.3° 335.2°
G107.26+05.71
0.0 0.5 1.0 2.0
+64.0°
+63.9°
335.4° 335.3° 335.2° 335.1° 335.0°
G109.70+02.52
0.00 0.25 0.50
+62.4°
+62.3°
343.5° 343.4° 343.3° 343.2°
G109.81+02.72
0.0 0.5 1.0
+62.6°
+62.5°
343.6° 343.5° 343.4° 343.3° 343.2°
G139.14-03.23
0.0 0.5
+55.9°
+55.8°
42.7° 42.6° 42.5°
G159.23-20.09
0.0 0.5 1.0 2.0
+31.2°
+31.1°
53.4° 53.3°
G162.46-08.69
0.0 0.5
+37.6°
+37.5°
65.5° 65.4° 65.3°

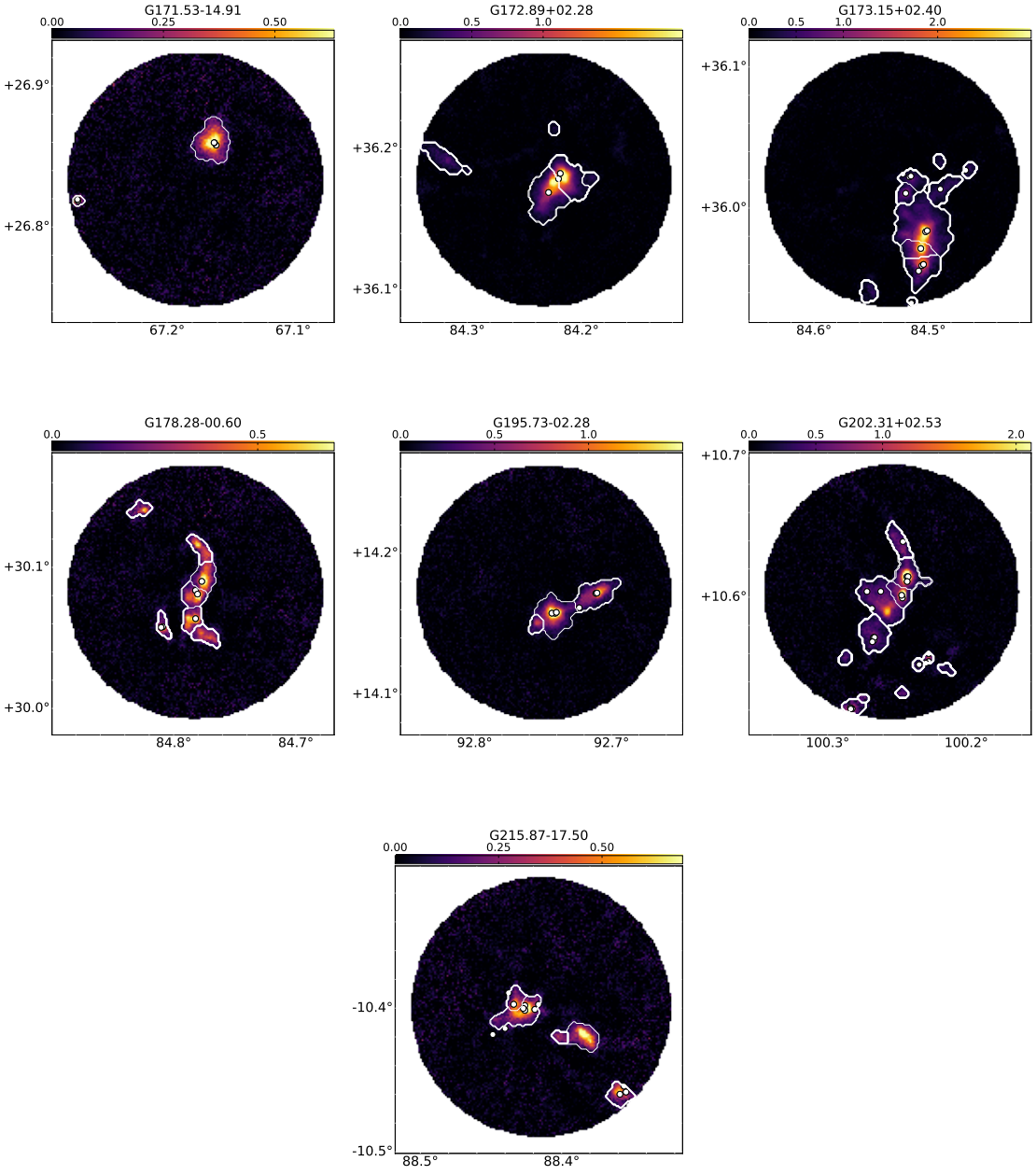
G171.53-14.91
0.00
0.25
0.50
+26.9°
+26.8°
67.2°
67.1°
G172.89+02.28
0.0
0.5
1.0
+36.2°
+36.1°
84.3°
84.2°
G173.15+02.40
0.0
0.5
1.0
2.0
+36.1°
+36.0°
84.6°
84.5°
G178.28-00.60
0.0
0.5
+30.1°
+30.0°
84.8°
84.7°
G195.73-02.28
0.0
0.5
1.0
+14.2°
+14.1°
92.8°
92.7°
G202.31+02.53
0.0
0.5
1.0
2.0
+10.7°
+10.6°
100.3°
100.2°
G215.87-17.50
0.00
0.25
0.50
-10.4°
-10.5°
88.5°
88.4°

C.4 Plots of CO line spectra

Spectra of ^{12}CO and ^{13}CO J=1-0 transitions over the entire field are plotted here for fields G105.44+09.88, G159.23-20.09, and G202.31+02.53 used in the Bayesian distance estimates.

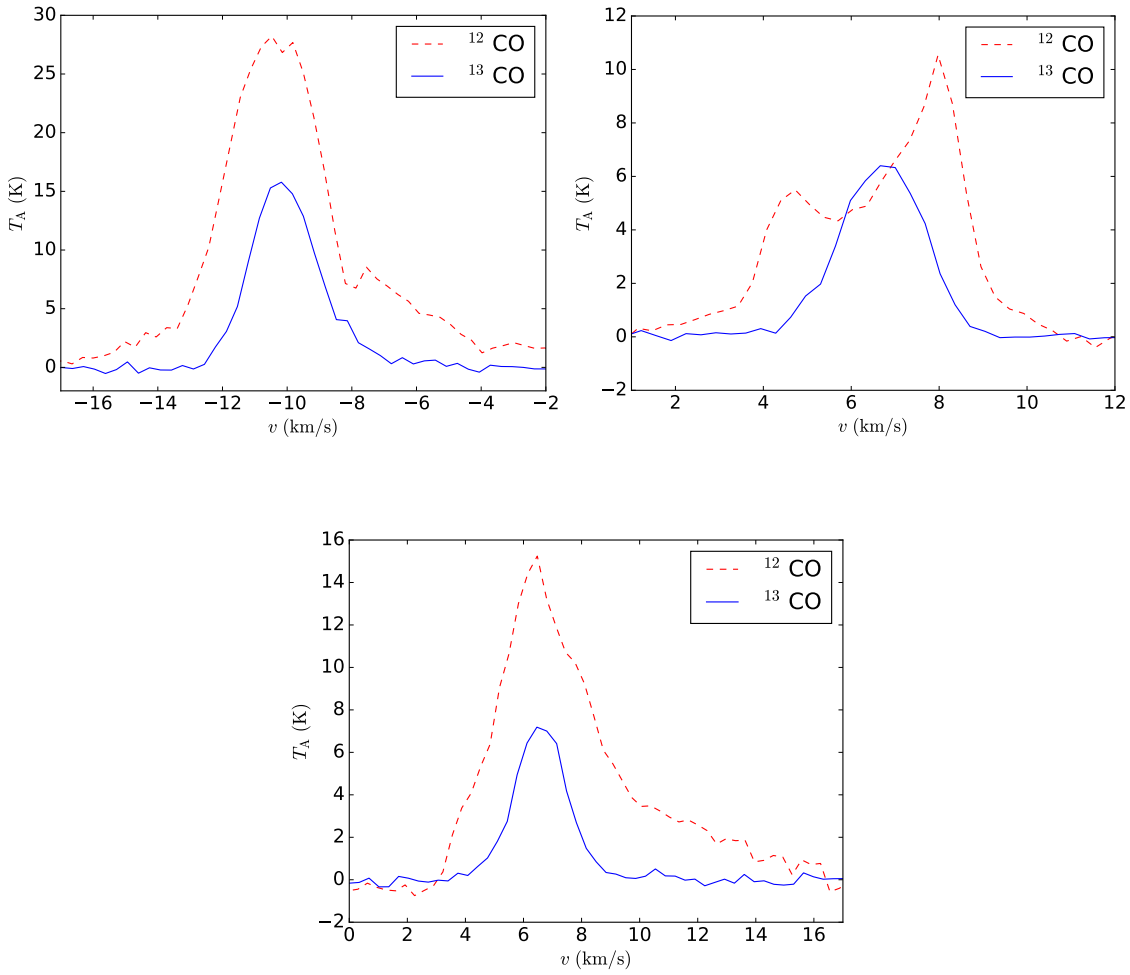

Figure C.1: ^{12}CO (*red dashes*) and ^{13}CO (*blue solid line*) spectra plotted for field G105.44+09.88 (*top left*), field G159.23-20.09 (*top right*) and G202.31+02.53 (*bottom*).

Individual clumps

^{13}CO spectra with a fitted Gaussian is plotted for clumps in the three fields which overlapped with the CO data.

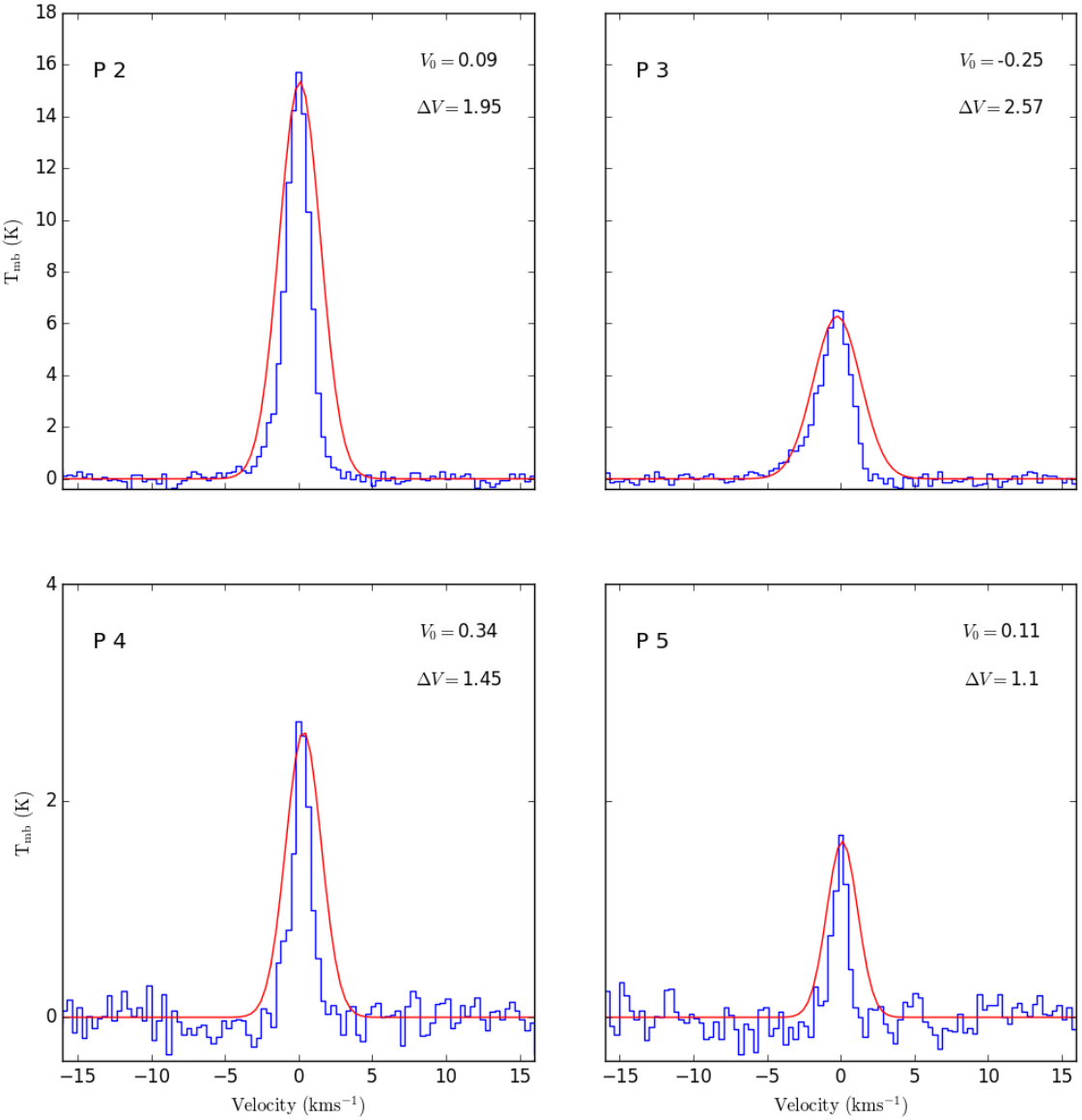

Figure C.2: ^{13}CO spectra for clumps 2, 3, 4, & 5 of field G105.

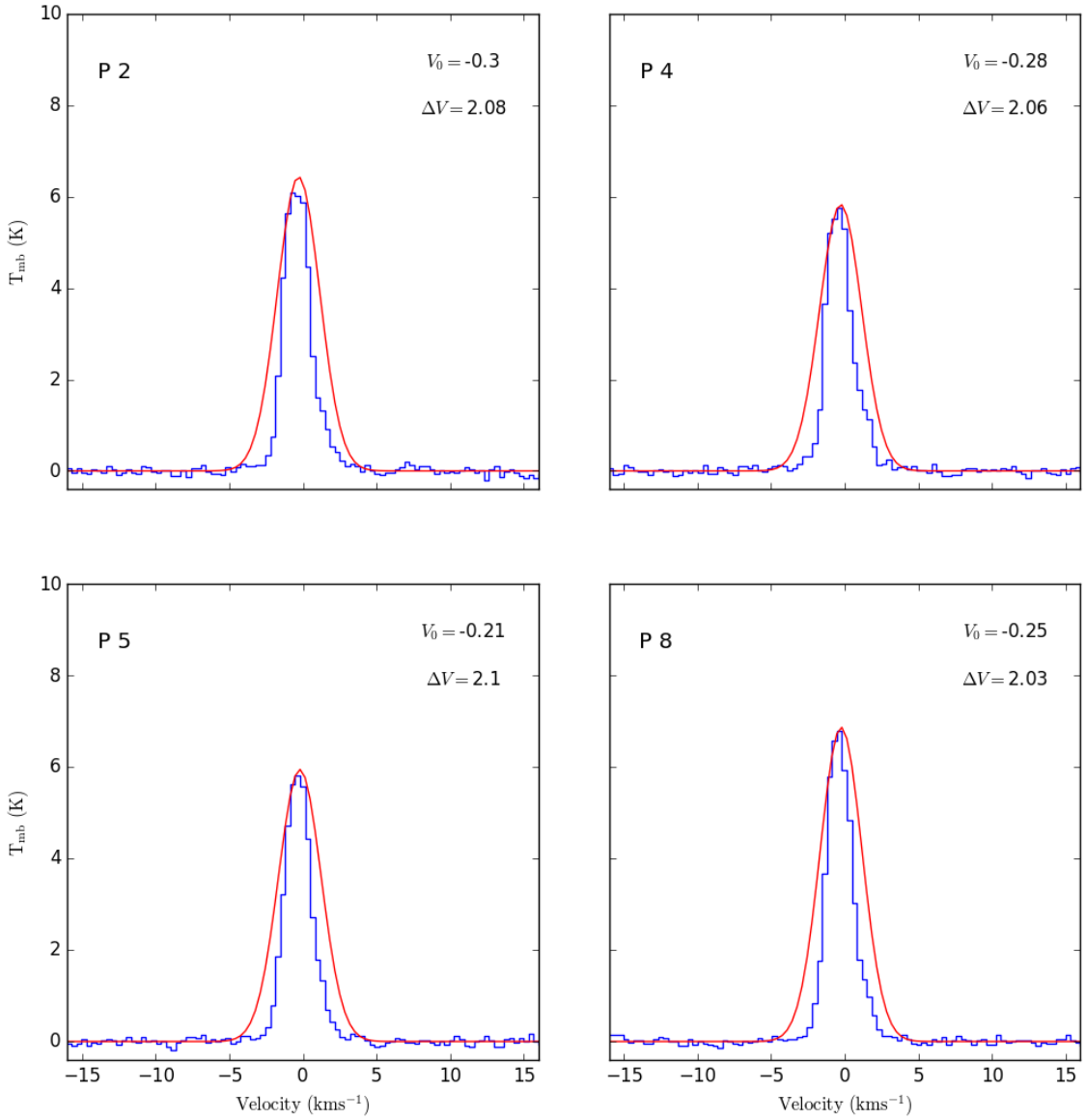

Figure C.3: ^{13}CO spectra for clumps 2, 4, 5, & 8 of field G159.

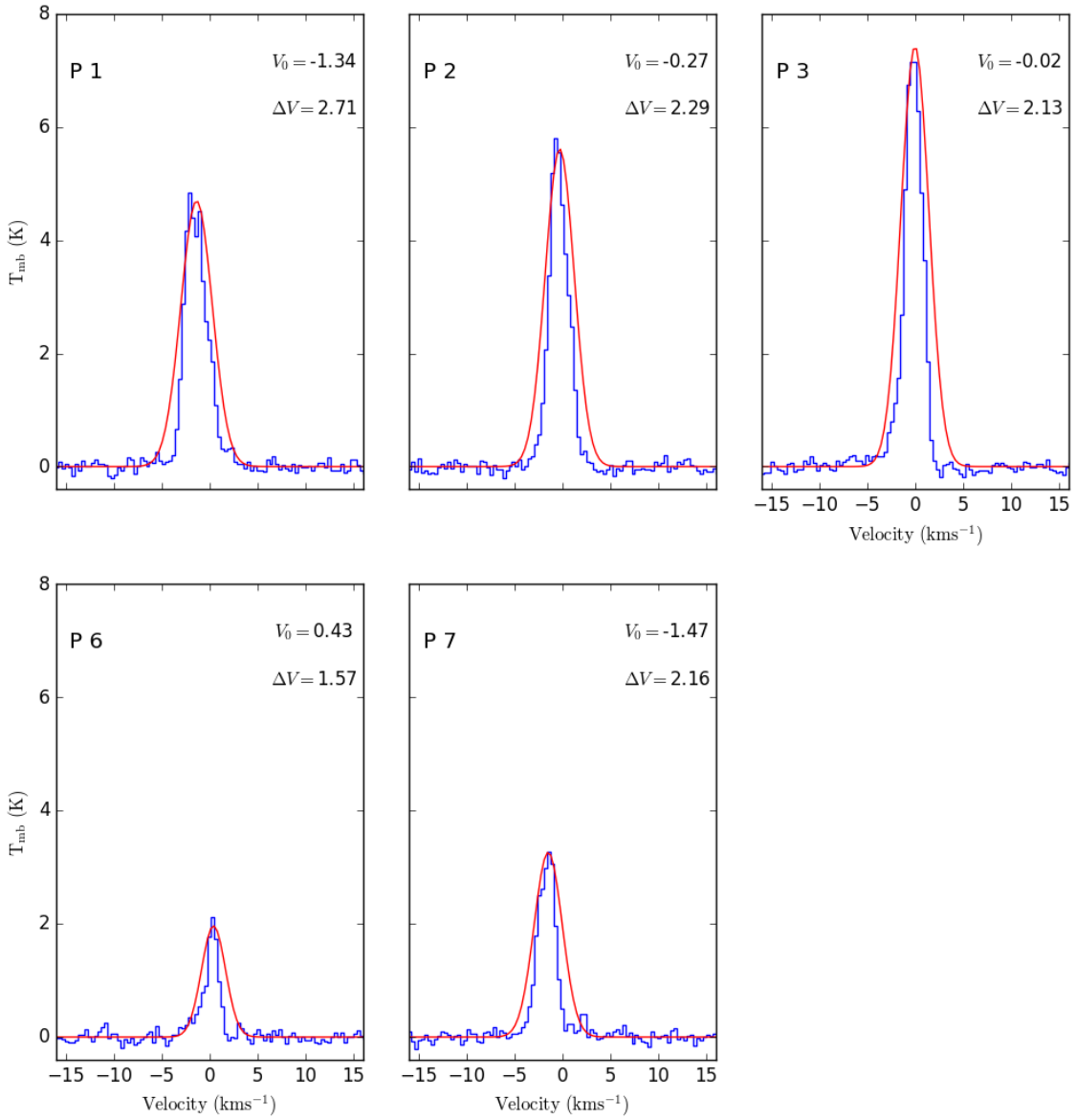

Figure C.4: ^{13}CO spectra for clumps 1-3, 6 & 7 of field G202.

D. Codes and Scripts - ISM analysis

D.1 Map convolution

One version of this code has been provided here, but separate ones were written for all wavelength combinations. Sigmas used for other wavelength combinations are shown in Table B.10.

```
#-----------------------------------------------------------------------
# Convolving Herschel SPIRE 250 um images to the resolution of 500 um images
#-----------------------------------------------------------------------
import numpy as np
from astropy.io import fits
import montage_wrapper as montage
import math
import os
from astropy.utils.data import get_pkg_data_filename
from astropy.convolution import Gaussian2DKernel
from astropy.convolution import convolve
from astropy.convolution import Gaussian1DKernel
#-----------------------------------------
# Calculate sigma
#-----------------------------------------
def sigma(img,band):
    sigma500 = 35.4                 # FWHM of the beam to be convolved to
    if band == 250:
        sigmaU = 17.9
    elif band == 350:
        sigmaU = 24.2
    minus = sigma500**2 - sigmaU**2
```

```
    sq = math.sqrt(minus)
    CDELT1_deg = img.header['CDELT1'] # Read CDELT1 from header
    CDELT1 = abs(CDELT1_deg*3600.0)
    new_FWHM = sq / CDELT1
    sigma = new_FWHM/(math.sqrt(CDELT1*8*math.log(2)))
    return sigma
#-----------------------------------------
# Code for 250 um data
#-----------------------------------------
def band_250():
    for filename in os.listdir(dir250):
        if filename.endswith('.fits'):
            # Get data
            inputFile = path_250+str(filename)
            current = get_pkg_data_filename(inputFile)
            img_250 = fits.open(current)[0]
            img = img_250.data
            sKernel250 = sigma(img_250,250)
            # Create kernel and convolve
            kernel = Gaussian2DKernel(sKernel250)
            conv = convolve(img,kernel)
            # Write convolved map to new FITS file
```

D.2 Map reprojection

```
#-----------------------------------------------------------------------
# Reprojects 160 um files to resolution of 500 um
#-----------------------------------------------------------------------
import montage_wrapper as montage
from astropy.io import fits
import numpy as np
import os
# matchFile = name of file which contains matches in different wavelengths
#--------------------
# Get 500 um headers
#--------------------
for filename in os.listdir(dir500):
    montage.mGetHdr(path_in+filename.fits,path_out+header_name.txt)
#-------------
# Reimage
```

```
#-------------
with open(matchFile) as matches:
    next(matches)
    for line in matches:
        # spire = header file's name
        # pacs = input file's name
        # outPut = name of reprojected file
        # exact_size = True sets the size of the output data array exactly
        #     the same as spire's data array.
        montage.reproject(pacs,outPut,header=spire,exact_size=True)
```

D.3 Derivation of ISM properties

This script was provided by Dr. Juvela. The SPIRE 500, 350, and 250 μm combination is used as an example.

```
#-----------------------------------------------------------------------
# Code to calculate column density and optical thickness, 250, 350, 500 um
#-----------------------------------------------------------------------
#-----------------------------------------
#        Functions
#-----------------------------------------
def MBB_fit_LSQ_mp(UM, S, dS=None, fixed_T=None, fixed_beta=None, filters=None,
    cc_routine=None,Tmin=6.9, Tmax=33.0, beta_min=0.59, beta_max=3.9,T_bins=171,
    beta_bins=171, ncpus=2, spline_smooth=1.0e-6, TCK=[]):
    """
    Wrapper for MBB_fit_chi2 to run the fit with multiprocessing.
    Uses the standard routine MBB_fit_chi2 and MBB_fit_LSQ
    """
    FIXED_BETA_ARRAY = False
    if (fixed_beta!=None):
        if (not(isscalar(fixed_beta))):
            FIXED_BETA_ARRAY = True  # beta fixed but using an array in fixed_beta

    # print '--- MBB_fit_chi2_parallel_2 ---'
    shape      = S[0].shape
    nfreq      = len(S)                 # number of frequencies
    npix       = len(ravel(S[0]))       # pixels in each vector/map
    n          = int(npix/ncpus)        # pixels per job
    if (n==0):                          # less pixels than workers
        return MBB_fit_LSQ(UM, S, dS, fixed_T, fixed_beta, filters, cc_routine,
                           Tmin, Tmax, beta_min, beta_max, T_bins, beta_bins,
```

```
                        spline_smooth=spline_smooth, TCK=TCK)
# set up jobs
manager = multiprocessing.Manager()
II      = multiprocessing.Array('f', npix)
TT      = multiprocessing.Array('f', npix)
BB      = multiprocessing.Array('f', npix)
PROC = []
print('MULTIPROCESSING WITH NCPUS %d' % ncpus)
for i in range(ncpus):
    a, b = i*n, (i+1)*n+1
    if (i==(ncpus-1)): b = npix
    SS, dSS  = [], []
    for iw in range(nfreq):
        SS.append( ravel(S[iw])[a:b].copy() )
    if (dS==None):
        dSS = None
    else:
        for iw in range(nfreq):
            dSS.append( ravel(dS[iw])[a:b].copy() )
    if (FIXED_BETA_ARRAY):
        FIXED_BETA = fixed_beta[a:b].copy()
        p =  multiprocessing.Process(target = MBB_fit_LSQ,
                    args   = (UM, SS, dSS, fixed_T, FIXED_BETA, filters, cc_routine,
                    Tmin, Tmax, beta_min, beta_max,
                    T_bins, beta_bins,
                    II, TT, BB, a,
                    TCK, spline_smooth))
    else:
        p =  multiprocessing.Process(target = MBB_fit_LSQ,
                    args   = (UM, SS, dSS, fixed_T, fixed_beta, filters, cc_routine,
                    Tmin, Tmax, beta_min, beta_max,
                    T_bins, beta_bins,
                    II, TT, BB, a,
                    TCK, spline_smooth))

    PROC.append(p)
    print('.... start %d ... %d-%d = %d pixels' % (i, a, b, b-a), SS[0].shape)
    p.start()

# gather results
# print 'gather'
```

```
    # T, B = zeros(npix, float32), zeros(npix, float32)
    for i in range(ncpus):
        PROC[i].join()
        print('gather ', i)

    II = asarray(II, float32)
    TT = asarray(TT, float32)
    BB = asarray(BB, float32)
    II.shape = shape
    TT.shape = shape
    BB.shape = shape
    return II, TT, BB


def PlanckFunction(freq, T):
    """
    Return value of the Planck function.
    Input parameters frequency (freq, [Hz]) and temperature (T, [K]).
    Returns the intensity in cgs units ([erg/s/cm2/sr/Hz]).
    """
    return (2.0*PLANCK*(freq/C_LIGHT)**2.0*freq) / (exp(H_K*freq/T)-1.0)


def MBB_function(f, T, B):
    # Modified Blackbody function
    return  PlanckFunction(f, T)/PlanckFunction(um2f(200.0), T)  * (f/um2f(200.0))**B

def um2f(um):
    """
    Convert wavelength [um] to frequency [Hz]
    """
    return C_LIGHT/(um*1.0e-4)

#-----------------------------------------------
# Main code
#-----------------------------------------------

# SPIRE matches are read into lists
for i in range(0,len(list_350)):
    H_250 = # SPIRE 250 um file
    H_350 = # SPIRE 350 um file
```

```
H_500 = # SPIRE 500 um file

#Example of calculating temperature and column density maps
UM     =  asarray([250.0, 350.0, 500.0], float32)   #asarray makes list into array

#250
F1 = pyfits.open(path_250_in+H_250)
#350
F2 = pyfits.open(path_350_in+H_350)
#500
F3 = pyfits.open(path_500_in+H_500)

m  = nonzero((F1[0].data!=0.0)&(isfinite(F1[0].data))&
             (F2[0].data!=0.0)&(isfinite(F2[0].data))&
             (F3[0].data!=0.0)&(isfinite(F3[0].data)))
S  = []
S.append(F1[0].data[m])
S.append(F2[0].data[m])
S.append(F3[0].data[m])
dS = []
dS.append(0.07*F1[0].data[m])
dS.append(0.07*F2[0].data[m])
dS.append(0.07*F3[0].data[m])

BETA       =  1.8   # using a fixed dust opacity spectral index
ncpus      =  4     # number of cores to use in the computation
filterList = ['filter_PSW.txt','filter_PMW.txt','filter_PLW.txt']
I200, T, B =  MBB_fit_LSQ_mp(UM, S, dS=dS, fixed_T=None, fixed_beta=BETA,
         filters=filterList, cc_routine=None,Tmin=6.9, Tmax=33.0, beta_min=0.59,
         beta_max=3.9,T_bins=171, beta_bins=171, ncpus=2, spline_smooth=1.0e-6, TCK=[])

# Convert fitted intensity map from 200um to 250um (unit probably MJy/st ==
# defined by input files).
I250       =  I200 * MBB_function(um2f(250.0), T, B) / MBB_function(um2f(200.0), T, B)

# Save fit results to FITS files.
F              =  pyfits.open(path_250_in+H_250)

F[0].data[:,:] =  0.0
F[0].data[m]   =  I250
F.writeto(outPath+name+'_test_I250.fits', clobber=True)
```

```
F[0].data[m]    =  T
F.writeto(outPath+name+'_test_T.fits', clobber=True)
F[0].data[m]    =  B
F.writeto(outPath+name+'_test_BETA.fits', clobber=True)

# Calculate optical depth at 250um
tau250  = I250*intensity_conversion('MJy/sr', 'cgs') / PlanckFunction(um2f(250.0), T)

# Calculate column density as N(H2)
NH2_TO_M  = 2.8*1.008*AMU                    # total gas mass per H2 molecule
kappa250 = 0.1*(um2f(250.0)/1000.0e9)**2.0  # Beckwith at al. kappa / total mass
NH2       = tau250/kappa250 / NH2_TO_M

F[0].data[m] =  tau250
F.writeto(outPath+name+'_test_tau.fits', clobber=True)

F[0].data[m] =  NH2
F.writeto(outPath+name+'_test_NH2.fits', clobber=True)
```

E. Codes and Scripts- clumps

E.1 FellWalker and EXTRACTCLUMPS

```
#-----------------------------------------------------------------
# Perform FellWalker on the 850 um files
# Convert the results into .fits files
#-----------------------------------------------------------------
# Each instance of os.system() makes a new shell
# Starlink- commands must be run in each excecution
#-----------------------------------------------------------------
import os
from astropy.io import fits
import numpy as np
import aplpy
import sys
sys.path.append('/home/emma/star-2017A/lib/')#libkpg_adam.so.0.0.0')
os.environ['PATH'] += os.path.pathsep + '/home/emma/star-2017A/lib/'
os.environ['PATH'] += os.pathsep + '/home/emma/star-2017A/lib/'
#-------------
# Functions
#-------------
def pixel_to_wcs(filename):
    if filename != 'NA':
        fig = aplpy.FITSFigure(filename)
        fData = fits.open(filename)[0].data
        S = fData.reshape(fData.shape[1],fData.shape[2])
        I,J = np.indices(S.shape)
        ra,dec = fig.pixel2world(J,I)
        fig.close()
        return ra,dec
def getRMS(field):
```

```
    # read RMS from file
    return rms
#-------------
# Init
#-------------
cmd1 = "export STARLINK_DIR=/home/emma/star-2017A;"
cmd2 = "source $STARLINK_DIR/etc/profile;"
convert = '/home/emma/star-2017A/bin/convert/convert.sh'
cupid = '/home/emma/star-2017A/bin/cupid/cupid.sh'
fits2ndf = '/home/emma/star-2017A/bin/convert/fits2ndf'
ndf2fits = '/home/emma/star-2017A/bin/convert/fits2ndf'
cmd3 = convert
cmd4 = cupid
init = cmd1+cmd2+cmd3+';'+cmd4+';'
#-----------------------------------------------------
# Convert each FITS SCUBA-2 file to .sdf
#-----------------------------------------------------
for filename in os.listdir(in_850):
    if filename.endswith('.fits'):
        os.system(cmd1+cmd2+'convert'+';'
            +fits2ndf+' '+name_in+' '+name_out)
#-----------------------------------------------------
# Get FellWalker arguments
#-----------------------------------------------------
# Get RMS
with open('centers_scuba.txt') as c:
    next(c)
    for line in c:
        # read ra and dec of center of each SCUBA-2 field
        # read rms of each SCUBA-2 field
        rms_small = getRMS(p[0])
        rms = str((float(rms_small))*2.0)
#-----------------
# Do FellWalker
#-----------------
        clumps_out = outName(name)
        name_in = in_850+name
        name_out = out_850+clumps_out
        cat = out_850+name.strip('.sdf')+'_cat'
        command = init+findclumps+' '+name_in+' outcat= '+cat+' out='+name_out+
            ' method=FellWalker'+' RMS='+rms+' deconv=True config=^config_file_original.txt'
```

```
        os.system(command)
#-------------------------------
# sdf2fits
#-------------------------------
# Convert resultant .sdf files to FITS
for filename in os.listdir(in_850):
    if filename.endswith('.sdf'):
        os.system(cmd1+cmd2+'convert'+';'
            +ndf2fits+' '+name_in+' '+name_out)
#-------------------------------
# Extractclumps
#-------------------------------
for filename in os.listdir(mask_in):
    if filename.endswith('.sdf'):
        dataIN = input data, .sdf
        maskIN = mask data, .sdf
        fileOUT = output file
        cat = cat filename
        command = init+extractclumps+' '+maskIN+' '
            +dataIN+' '+fileOUT+' outcat='+cat
                +' deconv=true shape=ellipse'
        os.system(command)
```

E.2 Association of clumps with YSOs

```
#-------------------------------------------------------------
# Fix FITS file by removing its third dimension
# Function provided by Dr. Juvela
#-------------------------------------------------------------
def FixFits(F):
    for tag in [ 'CRPIX3', 'CRVAL3', 'CTYPE3', 'CDELT3', 'CUNIT3', 'LBOUND3',
                 'PC03_01','PC03_02','PC03_03', 'PC01_03', 'PC02_03', 'CD3_3' ]:
        try:
            F[0].header.remove(tag)
        except:
            pass
    if (len(F[0].data.shape)==3): # one dimension still in the data array
        F[0].data.shape = (F[0].data.shape[1], F[0].data.shape[2])
    F[0].data = np.asarray(F[0].data, dtype='float32')
    F.verify('fix')
    return F
```

```
#-------------------------------------------------------------
# Find YSOs that are associated with each clump
#-------------------------------------------------------------
import os
from astropy.io import fits
import aplpy
from functions import distance_on_sphere_deg
import numpy as np
from FixFits import FixFits
#-------------------------
# Code
#-------------------------
for filename in os.listdir(clumps_in):
    if filename.endswith('.fits'):
        doc = open('file corresponding to field','w')

        f = fits.open(clumps_in+filename)
        sc = FixFits(f)
        fData = sc[0].data
        #-------------------------------------
        # open Marton I/II catalog
        # Same was performed for all other catalogs
        #-------------------------------------
        try:
            vizI = open(vizierIFile,'r')
            next(vizI)
            for line in vizI:
                if len(line.strip()) == 0:
                    continue
                v = line.split()
                n,ra0,dec0 = v[2],float(v[3]),float(v[4])
                fig = aplpy.FITSFigure(sc)
                # Function that calculates whether there is a clump within
                # a few pixels of this area
                # r = 0.005 deg
                I,J = np.indices(fData.shape)
                RA,D = fig.pixel2world(J,I)
                dist = distance_on_sphere_deg(ra0,dec0,RA,D)
                m = np.nonzero((dist<0.005)&(np.isfinite(fData)))
                if fData[m].shape == (0,):
                    e = 'nan'
```

```
            else:
                a = np.mean(fData[m])
                e = round(a,0)
            #-------------------------
            # Round a to nearest whole number:
            # Any stars that fall onto
            # two clumps will be assigned to
            # the clump they share the most area with.
            #-------------------------
            fig.close()
    except:
        print 'Marton I/II: No file exists'
```

E.3 CO lines

The code was provided by Mika Saajasto.

```
import aplpy as apl
import numpy as np
import matplotlib.pyplot as plot
from astropy.io import fits
from math import log, exp
from scipy.optimize import fmin


#-------------------------------------------------------------
# Functions
#-------------------------------------------------------------
def GetPixelCoord(fname,xworld,yworld):
    '''
    For a given set, float or array, of world coordinates, in degrees
    return the physical coordinates of image fname
    '''
    fig = apl.FITSFigure(fname, dimensions=[0,1], slices=[0,0]) # For G105
  # fig = apl.FITSFigure(fname)#, dimensions=[2,3], slices=[0,0])
    if isinstance(xworld,(list,np.ndarray)):
        x_pix = np.zeros(len(xworld))
        y_pix = np.zeros(len(yworld))
        for i in range(len(xworld)):
            x_pix[i], y_pix[i] = fig.world2pixel(xworld[i],yworld[i])
    else:
        x_pix, y_pix = fig.world2pixel(xworld,yworld)
    fig.close()
```

```
    return x_pix, y_pix


def GetWorldCoord(fname,xpix,ypix):
    '''
    For a given set, float or array, of pixel coordinates,
    return the world coordinates of image fnam in degrees
    '''
    fig = apl.FITSFigure(fname, dimensions=[0,1], slices=[0])
    if isinstance(xpix,(list,np.ndarray)):
        x_world = np.zeros(len(xpix))
        y_world = np.zeros(len(ypix))
        for i in range(len(xpix)):
            x_world[i], y_world[i] = fig.pixel2world(xpix[i],ypix[i])
    else:
        x_world, y_world = fig.pixel2world(xpix,ypix)
    fig.close()
    return x_world, y_world



def chi2_gaussian_fit(P, X, Y, dY=None, P1=None, M=None):
    """
    Return Chi2 error for fitting a gaussian(s) to data.
    Usage:
        chi2 = chi2_gaussian_fit(p, X, Y, dY)
    Input:
        P     = parameters [ centre position, peak value, fwhm ]
                in case of multiple gaussians, a longer vector with
                such three elements for each component
        X, Y  = vectors of independent and dependent variable
        dY    = optionally, error estimates of dependent variable,
                can be None or a vector of same length with X and Y
        P1    = optional, original parameters (needed if M!=None)
        M     = mask with values > 1 for fitted parameters and
                0 for fixed parameters
    """
    YP = 0.0*Y
    if (M!=None):
        PP = np.asarray(P1.copy(), np.float64)          # some remain at original values
        PP[np.nonzero(M>0)] = P     # these are fitted parameters
    else:
```

```
        PP = P                  # all parameters free
    for i in range(len(PP)/3): # loop over gaussian components
        x0, y0, fwhm  = PP[(3*i):(3*i+3)]
        if (fwhm == 0):
            K = 0.0
        else:
            K             = 4.0*log(2.0)/(fwhm**2.0)
        for j in range(len(X)):
            YP[j]    += y0*exp(-K*(X[j]-x0)**2.0)
    if (dY==None):
        return sum((Y-YP)**2.0)
    else:
        return sum(((Y-YP)/dY)**2.0)

def fit_gaussian(X, Y, P=None, dY=None, M=None):
    """
    Fits a gaussian or several gaussians to data (X,Y).
    Usage:
        p    =  fit_gaussian(X, Y, dY=None, P=None)
    Input:
        X, Y =  vectors of independent and dependent variable
        P    =  initial values, [ centre position, peak value, fwhm ]
                in case of several gaussians, vector containing a multiple of such 3 elements
                or 2d array with several rows
                if None, routine tries to guess initial values for fitting
                a single gaussian
        dY   =  optional error estimates of dependent variable,
                None or vector with length equal to X and Y
        M    =  optional, an array of similar size to P, with zero for fixed
                parameters and positive values for fitted parameters
    Returns:
        P    =  [ centre, peak, FWHM ]
                in case of several gaussians, a 2d array of such arrays
    """
    dims = None
    if (P==None):
        # start by filling in guesses of initial values
        X0 = X[np.argmax(Y)]
        p0 = np.asarray([ np.dot(X,Y)/sum(Y), max(Y), sum( (Y*(X-X0)**2.0) ) / sum(Y) ]
                        , np.float32)
    else:
```

```
        dims = np.asarray(P).shape
        p0   = np.ravel(np.asarray(P))
    if (M!=None):
        m  = np.nonzero(np.ravel(np.asarray(M))>0)      # free parameters
        p1 = p0[m]                                      # fitted parameters
        M  = np.ravel(np.asarray(M))
    else:
        p1 = p0.copy()
    res  = fmin(chi2_gaussian_fit, p1, args=(X, Y, dY, np.asarray(p0), M), disp=False)
    if (M!=None):
        p2 = p0
        p2[np.nonzero(np.ravel(np.asarray(M))>0)] = np.asarray(res, np.float32)
    else:
        p2 = res
    if (dims):
        p2.shape = dims
        if (M!=None):
            M.shape = dims
    return p2


def FitGaussian(a,b,c,x):
    '''
    Defines a gaussian function
    Input:  a = height of the peak
            b = center of the peak
            c = width of the gaussian
            x = running x-axis value
    Output: gaus = the values of the gaussian as a function of x
    '''
    gaus = np.zeros(len(x))
    for i in range(len(x)):
        temp = ((x[i]-b)**2.0) / (2.0 * c**2.0)
        gaus[i] = a*exp(-temp)
    return gaus

#-------------------------------------------------------------
# Functions
#-------------------------------------------------------------

coords = np.loadtxt('new_KVN_coords.list',unpack=True, usecols=(-2,-1))
```

```
hdu = fits.open(C13+'SC19_13CO21.fits')
dat = hdu[0].data

nax1 = hdu[0].header['naxis1']
nax2 = hdu[0].header['naxis2']
nax3 = hdu[0].header['naxis3']

quess_f,quess_b, quess_v = 3.0, 1.5, -2.0
quess = [quess_v, quess_b, quess_f]
vel = np.linspace(-20.1199,20.0619,nax3)

fit_velocity = np.zeros(len(coords[0]))
fit_peak_bright = np.zeros(len(coords[0]))
fit_fwhm = np.zeros(len(coords[0]))

spectra = []
gaussian = []
s = [-2,-1,0,1,2]

for i in range(len(coords[0])):          # len(coords[0]) = number of clumps (= 10 for G105)
    temp2 = []

    # GetPixelCoord(filename, RA, DEC) of i:th clump
    xx, yy = GetPixelCoord(C13+'SC19_13CO21.fits', coords[0][i], coords[1][i])
    for j in range(nax3):        # For each velocity (for each frame of the data cube)
        temp1 = []
        for a in range(len(s)): # len(s) = 5, dat.shape = (1, 125, 48, 48)
            for b in range(len(s)):      # For a and b in range 0,4

                temp1.append(dat[0,j,xx+s[a],yy+s[b]])
                # nax3 = 125, but nax1 and nax2 = 48
        temp2.append(np.nanmean(temp1))
    spectra.append(temp2[::-1]) #13CO
    spec = np.asarray(spectra[i])
    fit_velocity[i], fit_peak_bright[i], fit_fwhm[i] = fit_gaussian(vel,spec, P=quess)
    gaussian.append(FitGaussian(fit_peak_bright[i],fit_velocity[i],
                    np.sqrt(fit_fwhm[i]),vel))
```

References

1 D. Ward-Thompson and A. P. Whitworth, *An Introduction to Star Formation*. Cambridge University Press, 2011.

2 T. Liu, K.-T. Kim, M. Juvela, and et al., "The TOP-SCOPE survey of Planck Galactic Cold Clumps: Survey overview and results of an exemplar source, PGCC G26.53+0.17," *The Astrophysical J. Supplement S.*, vol. 243, February 2018.

3 S. S. R. Offner, P. C. Clark, P. Hennebelle, and et al., "The origin and universality of the stellar initial mass function," in *Protostars and Planets VI* (H. Beuther, R. S. Klessen, C. P. Dullemond, and T. Henning, eds.), Tucson, AZ, USA: University of Arizona Press, 2014.

4 B. Draine, *Physics of the interstellar and intergalactic medium*. Princeton University Press, 2011.

5 R. B. Larson, "The physics of star formation," *Rept.Prog.Phys*, vol. 66, 2003.

6 K. A. Marsh, J. M. Kirk, P. André, and et al., "A census of dense cores in the Taurus L1495 cloud from the Herschel Gould Belt Survey," *Monthly Notices of the Royal Astronomical Society*, vol. 459, no. 1, pp. 342–356, 2016.

7 V. Könyves, P. André, A. Men'shchikov, and et al., "A census of dense cores in the Aquila cloud complex: SPIRE/PACS observations from the Herschel Gould Belt Survey," *A& A*, vol. 584, December 2015.

8 D. Polychroni, E. Schisano, D. Elia, and et al., "Two mass distributions

in the L 1641 molecular clouds: The Herschel connection of dense cores and filaments in Orion A," *ApJ Letters*, vol. 777, October 2013.

9 C. McKee and E. Ostriker, "Theory of star formation," *Annual Review of Astronomy and Astrophysics*, vol. 45, 2007.

10 S. I. Sadavoy, J. di Francesco, P. André, and et al., "Herschel observations of a potential core-forming clump: Perseus B1-E," *A& A*, vol. 540, p. A10, Apr. 2012.

11 R. C. Bohlin, B. D. Savage, and J. F. Drake, "A survey of interstellar HI from L-alpha absorption measurements. II," *ApJ*, vol. 224, pp. 132–142, 8 1978.

12 H.-B. Li, K. H. Yuen, F. Otto, P. K. Leung, T. K. Sridharan, Q. Zhang, H. Liu, Y.-W. Tang, and K. Qiu, "Self-similar fragmentation regulated by magnetic fields in a region forming massive stars," *Nature*, vol. 520, pp. 518–521, Apr. 2015.

13 E. A. Bergin and M. Tafalla, "Cold dark clouds: The initial conditions for star formation," *Annual Review of Astronomy & Astrophysics*, vol. 45, pp. 339–396, 09 2007.

14 K. Pattle, D. Ward-Thompson, J. M. Kirk, and et al., "The JCMT Gould Belt Survey: first results from the SCUBA-2 observations of the Ophiuchus molecular cloud and a virial analysis of its prestellar core population," *Monthly Notices of the Royal Astronomical Society*, vol. 450, pp. 1094–1122, June 2015.

15 M. Benedettini, S. Pezzuto, E. Schisano, and et al., "A catalogue of dense cores and young stellar objects in the Lupus complex based on Herschel Gould Belt Survey observations," *published on ArXiv*, 09 2018.

16 T. Giannini, D. Elia, D. Lorenzetti, and et al., "The Herschel view of the on-going star formation in the Vela-C molecular cloud," *A& A*, vol. 539, march 2012.

17 S. I. Sadavoi, J. Di Francesco, D. Johnstone, and et al., "The Herschel and JCMT Gould Belt Surveys: Constraining dust properties in the Perseus B1 clump with PACS, SPIRE, and SCUBA-2," *ApJ*, March 2013.

18 S. V. W. Beckwith, A. I. Sargent, R. S. Chini, and R. Guesten, "A survey for circumstellar disks around young stellar objects," *ApJ*, vol. 99, pp. 924–945, march 1990.

19 M. Juvela, K. Demyk, Y. Doi, and et al., "Galactic Cold Cores VI. dust opacity spectral index," *A& A*, december 2015.

20 D. Bresnahan, D. Ward-Thompson, J. M. Kirk, and et al., "The dense cores and filamentary structure of the molecular cloud in Corona Australis: Herschel SPIRE and PACS observations from the Herschel Gould Belt Survey," *A& A*, vol. 615, July 2018.

21 N. Schneider, F. Motte, S. Bontemps, and et al., "The Herschel view of star formation in the Rosette molecular cloud under the influence of NGC 2244," *Astronomy & Astrophysics*, vol. 518, may 2010.

22 J. Ostriker, "The equilibrium of polytropic and isothermal cylinders," *ApJ*, vol. 140, p. 1056, 10 1964.

23 I. MacLaren, K. M. Richardson, and A. W. Wolfendale, "Corrections to virial estimates of molecular cloud masses," *ApJ*, vol. 333, p. 821, October 1988.

24 A. Parikka, M. Juvela, V.-M. Pelkonen, J. Malinen, and J. Harju, "The physical state of selected cold clumps," *Astronomy & Astrophysics*, vol. 577, 5 2015.

25 P. F. Goldsmith, "Molecular Depletion and Thermal Balance in Dark Cloud Cores," *ApJ*, vol. 557, pp. 736–746, Aug. 2001.

26 W. Bonnor, "Boyle's law and gravitational instability," *MNRAS*, vol. 116, pp. 351–359, June 1956.

27 R. Ebert, "Über die Verdichtung von H I-Gebieten. Mit 5 Textabbildungen," *Zeitschrift für Astrophysik*, vol. 37, p. 217, 1955.

28 K. Pattle, D. Ward-Thompson, J. M. Kirk, and et al., "The JCMT Gould Belt Survey: first results from SCUBA-2 observations of the Cepheus Flare region," *MNRAS*, vol. 464, pp. 4255–4281, Feb. 2017.

29 C. J. Lada, *Star formation - From OB associations to protostars*. D. Reidel Publishing Co, 1987. Accessed through ArXiv.

30 P. Andre, D. Ward-Thompson, and M. Barsony, "Submillimeter continuum observations of Rho Ophiuchi A - the candidate protostar VLA 1623 and prestellar clumps," *ApJ*, vol. 406, March 1993.

31 T. P. Greene, B. A. Wilking, P. Andre, E. T. Young, and C. J. Lada, "Further mid-infrared study of the Rho Ophiuchi cloud young stellar population: Luminosities and masses of pre-main-sequence stars," *ApJ*, vol. 434, pp. 614–626, October 1994.

32 G. H. Herbig, "The spectra of Be- and Ae-typ e stars associated with nebulosity," *ApJS*, vol. 4, p. 337, 03 1960.

33 T. P. Robitaille and B. A. Whitney, "The present-day star formation rate of the Milky-Way determined from Spitzer detected young stellar objects," *ApJ Letters*, vol. 710, January 2010.

34 M. Schmidt, "The rate of star formation," *ApJ*, vol. 129, p. 243, 03 1959.

35 R. C. J. Kennicutt, "The global Schmidt law in star-forming galaxies," *ApJ*, vol. 498, pp. 541–552, 05 1998.

36 R. C. J. Kennicutt and N. J. I. Evans, "Star formation in the Milky Way and nearby galaxies," *Annual Review of Astronomy and Astrophysics*, vol. 50, pp. 531–608, 09 2012.

37 S. Longmore, J. Bally, L. Testi, and et al., "Variations in the Galactic star formation rate and density thresholds for star formation," *Monthly notices of the Royal Astronomical Society*, vol. 429, no. 2, pp. 987–1000, 2013. accessed thru `http://citeseerx.ist.psu.edu/viewdoc/download?doi=10.1.1.881.6661&rep=rep1&type=pdf`.

38 E. E. Salpeter, "The luminosity function and stellar evolution," *ApJ*, vol. 121, pp. 161–167, 1 1955.

39 P. Kroupa, "The Initial Mass Function of Stars: Evidence for Uniformity in Variable Systems," *Science*, vol. 295, pp. 82–91, Jan. 2002.

40 G. Chabrier, "Galactic Stellar and Substellar Initial Mass Function," *The Publications of the Astronomical Society of the Pacific*, vol. 115, pp. 763–795, July 2003.

41 Planck Collaboration, P. A. R. Ade, N. Aghanim, M. Arnaud, M. Ashdown, J. Aumont, C. Baccigalupi, A. J. Banday, R. B. Barreiro, N. Bar-

tolo, and et al., "Planck 2015 results. XXVIII. The Planck Catalogue of Galactic Cold Clumps," *Astronomy & Astrophysics*, vol. 594, sep 2016.

42 P. collaboration, "Planck 2015 results. I. overview of products and scientific results," *Astronomy & Astrophysics*, February 2015. Accessed through Arxiv.

43 M. Tang, T. Liu, S.-L. Qin, and et al., "The properties of Planck Galactic Cold Clumps in the L1495 dark cloud," *ApJ*, vol. 856, April 2018.

44 K. Tatematsu, "The onset of star formation in widely different environments." unpublished. Observation time proposal for Nobeyama telescope, given by Adjunct Prof. Mika Juvela.

45 J. Montillaud, M. Juvela, A. Rivera-Ingraham, and et al., "Galactic cold cores IV. Cold submillimetre sources: catalogue and statistical analysis," *Astronomy & Astrophysics*, vol. 584, Dec. 2015.

46 "SCUBA-2." `http://www.eaobservatory.org/jcmt/instrumentation/continuum/scuba-2/`. Accessed: 27.4.2018.

47 E. L. Chapin, D. S. Berry, A. G. Gibb, and et al., "SCUBA-2: iterative map-making with the sub-millimetre user reduction facility," *Monthly Notices of the Royal Astronomical Society*, vol. 430, p. 2545–2573, apr 2013.

48 "Herschel." `http://sci.esa.int/herschel/`. Accessed: 27.4.2018.

49 "SPIRE in depth." `http://herschel.cf.ac.uk/mission/spire`.

50 *PACS photometer scientific capabilities*, ch. 3.

51 "Herschel science archive." http://archives.esac.esa.int/hsa/whsa/.

52 S. I. Sadavoy, J. Di Francesco, D. Johnstone, et al., t. JCMT, and H. G. B. S. Teams, "The Herschel and JCMT Gould Belt Surveys: Constraining dust properties in the Perseus B1 clump with PACS, SPIRE, and SCUBA-2," *ApJ*, vol. 767, 4 2013.

53 M. Juvela, J. He, K. Pattle, and et al., "Herschel and SCUBA-2 observations of dust emission in a sample of Planck Cold Clumps," *A& A*, vol. 612, p. A71, apr 2018.

54 M. J. Reid, T. M. Dame, K. M. Kenten, and A. Brunthaler, "A parallax-based distance estimator for spiral arm sources," *ApJ*, vol. 823, June 2016. Accessed through ArXiv.

55 K. Wang, S. Zahorecz, M. R. Cunningham, et al., and S. Collaboration, "First data release of the ESO-ARO public survey sampling -SMT "all-sky" mapping of Planck interstellar nebulae in the Galaxy," *RNAAS*, january 2018. Accessed through ArXiv.

56 D. Berry, "Fellwalker—a clump identification algorithm," *Astronomy and Computing*, vol. 10, April 2015.

57 D. Berry, "CUPID – A 3D clump identification and analysis package version 2.2 users' manual." `http://starlink.eao.hawaii.edu/devdocs/sun255.pdf`, April 2016.

58 G. Marton, L. Tóth, R. Paladini, and et al., "An all-sky support vector machine selection of WISE YSO candidates," *Monthly Notices of the Royal Astronomical Society*, vol. 458, pp. 3479–3488, june 2016.

59 M. Wenger, F. Ochsenbein, D. Egret, and et al., "The SIMBAD astronomical database," *Astronomy and Astrophysics Supplement*, vol. 143, pp. 9–22, April 2000. Accessed through ArXiv.

60 I. Yamamura, S. Makiuti, N. Ikeda, and et al., "AKARI/FIS all-sky survey Bright Source Catalogue version 1.0." http://www.ir.isas.jaxa.jp/AKARI/Archive/Catalogues/PSC/RN/AKARI-FIS_BSC_V1_RN.pdf, March 2010.

61 H. Kataza, C. Alfageme, A. Cassatella, and et al., "AKARI/IRC all-sky survey Point Source Catalogue version 1.0." http://www.ir.isas.jaxa.jp/AKARI/Archive/Catalogues/PSC/RN/AKARI-IRC_PSC_V1_RN.pdf, March 2010.

62 G. Marton, L. Calzoletti, A. M. Perez Garcia, et al., and the Herschel Point Source Catalogue Working Group, "The Herschel/PACS Point Source Catalogue explanatory supplement," May 2017.

63 *The Spectral and Photometric Imaging REceiver (SPIRE) handbook*. Herschel Space Observatory, 3.1 ed., february 2017.

64 R. Cutri, M. Skrutskie, S. Van Dyk, and et al., "Explanatory supplement to the 2MASS All Sky data release and extended mission products," nov 2006. https://old.ipac.caltech.edu/2mass/releases/allsky/doc/explsup.html.

65 R. M. Cutri, E. L. Wright, T. Conrow, and et al., "Explanatory supplement to the AllWISE data release products," jan 2014. http://wise2.ipac.caltech.edu/docs/release/allwise/expsup/.

66 H. Beuther, J. Tackenberg, H. Linz, and et al., "Galactic Structure Based on the ATLASGAL 870 μm Survey," *ApJ*, vol. 747, p. 43, Mar. 2012.

67 D. Elia, S. Molinari, Y. Fukui, and et al., "The first Hi-GAL observations of the outer Galaxy: A look at star formation in the third Galactic

quadrant in the longitude range 216.°5 <∼ l <∼ 225.°5," *ApJ*, vol. 772, July 2013.